UNIVERSITÀ DI SIENA 1240

Dipartimento di Scienze fisiche, della Terra e dell'ambiente

Dottorato in Scienze e tecnologie ambientali, geologiche e polari

33° Ciclo

Coordinatore: Prof. Simone Bastianoni

Geochemical characterization of dust from the Talos Dome ice core

Settore scientifico disciplinare: GEO04

Candidata

Elena Di Stefano
Università degli studi di Siena

Tutore

Valter Maggi
Università degli studi di Milano-Bicocca

Co-tutori

Barbara Delmonte
Università degli studi di Milano-Bicocca

Paolo Gabrielli
Byrd Polar and Climate Research Center,
Ohio State University

Anno accademico di conseguimento del titolo di Dottore di ricerca
2019/2020

Università degli Studi di Siena
Dottorato in Scienze e tecnologie ambientali, geologiche e polari
33° Ciclo

Data dell'esame finale
27 Aprile 2021

Commissione giudicatrice
Massimo Frezzotti, Università degli studi Roma Tre
Giancarlo Della Ventura, Università degli studi Roma Tre
Sarah Aarons, University of California, San Diego (USA)

Esperti
Andrea Spolaor, Università Ca' Foscari Venezia
Sarah Aarons, University of California, San Diego (USA)

Supplente
Barbara Stenni, Università Ca' Foscari Venezia

Abstract

Polar ice cores contain many proxies, of which mineral dust is a key one in understanding past climate variability. In fact, dust and climate have a strong influence on each other. Dust has both direct and indirect effects on climate by interacting with solar radiation and influencing cloud formation processes, while climate itself can strongly affect production, transport and deposition of dust. For example, it is well known that dust fluxes respond to the transition from glacial to interglacial regimes. Deposition of dust on the Antarctic continent is controlled by a number of climatic and environmental factors, and a reliable reconstruction of the dust record is essential to understand how these factors have changed in the past. But evidence has shown that, at certain depths in the ice, the dust record may be subjected to some degree of alteration.

This work was conceived with the main objective of enhancing our comprehension of deep ice processes through the use of an array of different techniques applied to the Talos Dome ice core. In particular, we aim at studying the chemical and physical anomalies present in the deeper part of the dust record and confirm the existence of post-depositional processes which may alter the climatic signal embedded in deep ice. Moreover, we wish to observe how different elements partition between soluble and insoluble phase, at different depths of the ice core and link the geochemical patterns of the considered elements to the main climatic oscillations covered in the Talos Dome ice core.

The Talos Dome ice core, drilled from a peripheral dome in Eastern Antarctica, is 1620 m long and covers more than 250k years of climate history. We prepared samples from the entire length of the ice core, with a focus on depths lower than 1450 m, which have not yet been dated. In this work, the published dust record has been integrated in its deepest part, by analyzing 125 samples through Coulter Counter. The dust concentration in the Talos Dome ice core exhibits the well known correlation with the oxygen isotopic ratio; levels are low during interglacials and rise during the last glacial stage. South America, and Patagonia in particular, has been recognized as the major dust supplier for Eastern Antarctica during glacial stages, while during interglacials other sources become more relevant. When the hemispheric dust influx from remote sources is dampened, local sources become more important to the total dust budget at Talos Dome.

We calculated two indexes, Fine Particle Percentage (FPP) and Coarse Local Particle Percentage (CLPP), to assess the relative contribution of fine and coarse particles to the total dust record. The deeper section of the ice core displayed some anomalies: FPP drops to very low values, while CLPP shows a significant increase. Moreover, we found that modal values for the volume size distribution shift from 2 μm to higher values at deeper depths. We interpret this as a sign of dust aggregation, which was confirmed by our observations at SEM. We found evident weathering features in grains belonging to samples from the deep section. Elemental maps of individual grains show that precipitates present in the deep part are typically composed by Fe, S and K, which is compatible with the chemical formula of jarosite, while the "residual" cores of the grains mostly consist in Si or a mixture of Si and Al. These results are compatible with the acidic weathering of basalt in a closed system. Jarosite is also known to act as a cement during weathering, explaining the difficulty we encountered in breaking the aggregates when we performed tests with an ultrasonic bath.

We further investigated the elemental composition of dust in the Talos Dome ice core with INAA and ICP-SFMS measurements, covering 36 different elements with the former

and 38 with the latter; 22 elements overlapped between the two techniques, allowing comparisons between the two. Our principal aim was to study the fractionation of elements between soluble and insoluble phase and how this may change at different climatic stages. We consider INAA results to reflect the composition of the insoluble fraction of dust, while filtered ICP-SFMS samples should reflect the soluble fraction, and untreated ICP-SFMS samples are considered as a benchmark for the total dissolvable concentration. We also used enrichment factors and correlation matrices to assess the crustal or non crustal origin of the considered elements.

The high correlations and low enrichment factors found among insoluble elements confirm a prevalent crustal source for mineral dust. Other minor contribution to mineral dust can derive from volcanic eruptions and marine emissions, in the form of sea salt sprays and biogenic emissions, as testified by our records of mercury and selenium. The concentration of some elements, namely As, Sr, Ni and Ca, is the probable result of a mixture of different sources, both terrestrial and marine, making the signal harder to read.

Rare Earth elements were measured both with INAA and ICP-SFMS. They present a typical crustal behavior, with crustal-like concentrations and low solubility. No evident differences were observed along the core, confirming that these set of elements is among the most suited to track crustal material, regardless of weathering.

In our solubility study, the majority of elements exhibits a minimum in solubility during the last glacial maximum. This is the result of higher fluxes of mineral dust which were transported to the Antarctic continent from remote sources and is consistent with the crustal origin we documented for the better part of the elements considered. Many elements also showed a maximum in solubility in shallower samples, belonging to the Holocene. Despite this, no clear trends connected to depth were found, except for iron. The decrease of iron's solubility with depth further supports the chemical weathering of the deeper sections of the ice core. When comparing INAA and ICP-SFMS data, the soluble fraction typically remains constant while the total and insoluble fraction vary. Concentrations are higher during glacial stages and lower during interglacials, showing a good correlation with total dust content. Deep samples always display an intermediate behavior, which could point to a disturbance in the paleoclimatic signal of this section, leading to a homogenization of the concentration from different climatic periods.

Five elements (Ag, Ni, Ta, Li, Na) were found to be completely soluble throughout the entire ice core, and three more (Rb, Cs, Bi) have shown strong solubility tendencies. We suggest this may be due to a significant bond of these elements with insoluble particles smaller than 0.2 μm, which would not be retained by the filter thus altering our soluble fraction. Because these elements do not display the typical glacial/interglacial pattern of aeolian dust, we can also hypothesize a predominant local origin for these elements, and in particular the result of aeolian remobilization of local volcanic material.

Contents

Chapter 1

Introduction

Glaciers and ice sheets are a key point in understanding the changes that the climate is undergoing, as they have a major influence on the hydrological cycle and on the net surface energy budget. They also provide highly resolved records of climate signals, atmospheric parameters and forcing factors. In this chapter we will briefly discuss the current state of the cryosphere in the light of climate change, and we will see how the climate of the past can be reconstructed through the use of natural archives. We will then focus on the Antarctic ice sheet, from its birth to present day state. This will serve as a general introduction to the core of this thesis, which aim is to expand the general knowledge of the elemental composition of mineral dust in Antarctic ice cores and to investigate the presence and the influence of post-depositional effects on the climatic record of deeper ice core sections.

1.1 Climate change

Anthropogenic climate change is today an undeniable reality. A warming of the climate system has been observed since the 1950s, and many of the observed changes are unprecedented over the last decades to millenia (IPCC, 2013b). Both the atmosphere and the ocean have experienced a progressive warming, ice sheets and glaciers worldwide have been continuously losing mass over the last few decades, and the rate of sea level rise since the industrial revolution has been larger than the mean rate during the previous two millennia (IPCC, 2013b).

1.1.1 The Cryosphere in a Changing Climate

The cryosphere and climate change are deeply interconnected, such that the Intergovernamental Panel on Climate Change (IPCC) issued in 2019 a special report focusing on the links between climate change, the oceans and the cryosphere (IPCC, 2019a). Global snow and ice cover directly affect the heating and cooling of the planet by modifying the surface albedo. This plays a role in determining how much energy is absorbed or reflected, influencing Earth's energy balance. Changes in snow and ice cover also affect air temperatures, sea levels and ocean currents all over the world. Vice versa, climate change strongly affects the various components of the cryosphere, although this may happen with different timescales. This is already very evident if we look at mountain regions, where changes in glacier area, length and mass show a global negative trend (Zemp et al., 2015; Medwedeff and Roe, 2017). The IPCC Special Report on the Ocean and Cryosphere in a Changing Climate considers *very likely* that atmospheric warming is the primary driver for global glacier recession and it has been estimated that the anthropogenic fraction of mass loss of all mountain glaciers has increased from 25 ± 35 % during the period 1851–2010 to 69 ± 24 % during the period 1991–2010 (Marzeion et al., 2014).

Polar regions, and especially Antarctica, may be slower in their response to climatic variations, due to the volume of ice involved and to nonlinear responses which involve thresholds. Nonetheless, not only glaciers, but also ice sheets are expected to experience irreversible mass losses on time scales relevant to human societies (IPCC, 2019b). There is *high confidence* that both polar oceans have continued to warm in recent years, with the Southern Ocean being disproportionately and increasingly important in global ocean heat increase (IPCC, 2019b). It is also *extremely likely* that the rapid ice loss from the Greenland and Antarctic ice sheets (Slater et al., 2021) during the early 21st century has increased into the near present day, adding to the ice sheet contribution to global sea level rise (IPCC, 2019b).

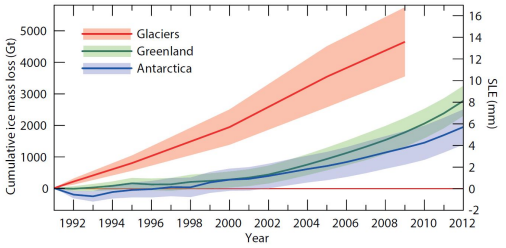

Figure 1.1: Contribution of Glaciers and Ice Sheets to Sea Level Change. Cumulative ice mass loss from glacier and ice sheets (in sea level equivalent) is 1 to 1,4 mm/year for 1993-2009 and 1.2 to 2.2 mm/year for 2005-2009. Adapted from IPCC (2013a).

1.1.2 Paleoclimatology

During Earth's geological history, the climate has greatly varied as a complex response to both internal and external forcings, which ultimately alter the global energy budget. For example, it is known that orbital parameters play a key role in driving long term climatic changes, but also that the natural oscillations of greenhouse gasses' concentrations have a deep connection with global temperatures, which in turn are strongly linked with atmospheric circulation patterns.

The study of the past climate variations may help us to better understand present ones and predict future scenarios. As defined by Bradley (2014), Paleoclimatology aims at the study of natural phenomena which are climate-dependent and which incorporate into their structure a measure of this dependency. Such phenomena provide a proxy record of climate that span beyond the period of instrumental measurements. Table 1.1 reports the main natural archives and their characteristics. Chapter 2 will further expand on the use of ice cores as paleoclimatic archives.

Table 1.1: Main natural archives and their characteristics. Adapted from (Bradley, 2014).

Archive	Minimum Sampling Interval	Temporal Range (years)	Potential Information Derived
Tree rings	Season/year	10^4	Temperature; Precipitation or Humidity; Biomass information; Volcanic eruptions; Solar Activity
Lake sediments	Year to 20 years	$10^4 - 10^6$	Temperature; Precipitation or Humidity; Biomass information; Volcanic eruptions; Geomagnetic field variations; Chemical composition of water
Corals	Year	10^4	Temperature; Precipitation or Humidity; Sea level; Chemical composition of water
Ice cores	Season/year	10^6	Temperature; Precipitation or Humidity; Biomass information; Volcanic eruptions; Solar Activity; Geomagnetic field variations; Chemical composition of air
Pollen	20 years	10^6	Temperature; Precipitation or Humidity; Biomass information
Speleothems	Year	$5 * 10^5$	Temperature; Precipitation or Humidity; Biomass information; Volcanic eruptions; Chemical composition of water
Paleosols	100 years	10^6	Temperature; Precipitation or Humidity; Biomass information
Loess	100 years	10^6	Precipitation or Humidity; Biomass information; Geomagnetic field variations
Geomorphic features	100 years	10^6	Temperature; Precipitation or Humidity; Volcanic eruptions; Sea level
Marine sediments	100 years	10^7	Temperature; Precipitation or Humidity; Biomass information ; Sea level; Solar Activity; Geomagnetic field variations; Chemical composition of water

1.2 The Antarctic Ice Sheet (AIS)

The Antarctic continent, situated over the south pole, is almost entirely covered by the Antarctic Ice Sheet.

Ice sheets are large masses of ice which bury the underlying topography and cover an area of more than 50 000 km^2. Unlike glaciers, which only flow in one direction, ice sheets flow from a center point in all outer directions. The center point is generally a Dome, which is also among the preferred sites for deep ice coring, as here the ice flow velocity is minimum, translating in lesser disturbances in the vertical record of the ice.

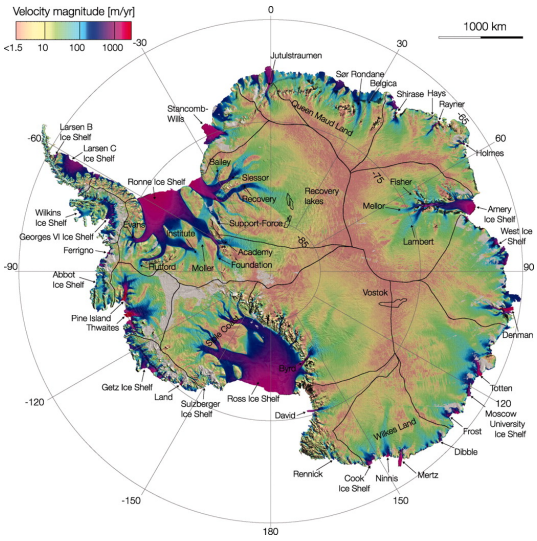

Figure 1.2: Ice flow velocity in Antarctica, from Rignot et al. (2011).

1.2.1 Present day AIS

The Antarctic ice sheet today contains more than half of Earth's freshwater reservoir, which would translate in a sea level rise of 57 m if it were to melt completely (Fretwell et al., 2013). Some studies have estimated that between 1992 and 2017, the Antarctic Ice Sheet has lost mass at an average rate of 66 ± 18 Gt/year, translating to an average 4.6 ± 1.2 mm contribution to global sea level over the same period (Shepherd et al., 2019). Others report total mass losses of 166 ± 18 Gt/year in the period 1999-2009 and 252 ± 26 Gt/year in the period 2009-2017, signaling to a fast acceleration in the last decades (Rignot et al., 2019). Overall, the majority of melt is concentrated where the Circumpolar Deep Water, a warm and salty oceanic current, meets the ice shelves (Rignot et al., 2019).

While it is commonly considered in its entirety, AIS is actually composed of two separated ice sheets: Eastern Antarctic Ice Sheet (EAIS) and Western Antarctic Ice Sheet (WAIS), divided by the Transantarctic Mountains, a 4000 m high mountain range which emerges from the ice sheet. EAIS rests on bedrock which is mainly above sea level, giving good stability to the

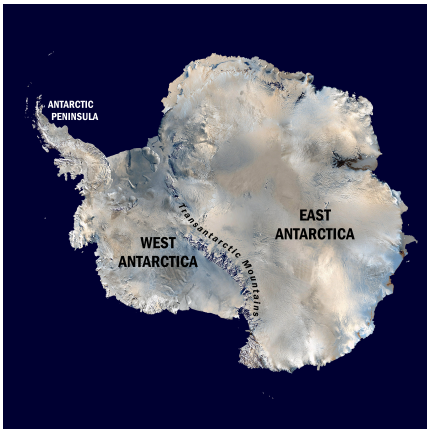

Figure 1.3: Satellite view of Antarctica (from Blue Marble: Next Generation series (Stockli et al., 2005))

ice sheet and thus permitting thicker ice growth, while WAIS seats prevalently over bedrock which is below sea level, making it more unstable. Multiple studies agree on the growing instability of West Antarctica, especially in the area around the Amundsen Sea (Mouginot et al., 2014; Rignot et al., 2014; Jenkins et al., 2018), and predict a significant contribution to sea level rise in decades to come. It has been estimated that West Antarctica experiences a mass loss which is three to four times larger than that from East Antarctica (Rignot et al., 2019). Eastern Antarctica covers a more extensive area than its occidental counterpart (85% of AIS) and shows a complex configuration. Ice flows from the ice divide towards the outer margins, feeding multiple ice streams. Frequently these end in ice shelves, floating glacier ice which has lost contact with the bedrock. EAIS, which was for long thought to have a positive mass balance, has also shown signs of distress: Rignot et al. (2019) concluded in their study that East Antarctica is a major participant in AIS mass loss.

A peculiar feature of the Antarctic continent are the Dry Valleys, in Northern Victoria Land (East Antrarctica). These are considered among the driest places in the world, experiencing an annual maximum precipitation of 50mm weq (Fountain et al., 2010), and are the largest ice-free zone of Antarctica. They are in a precipitation shadow of the Transantarctic Mountains which block the moist air coming from the Ross sea sector, and the surrounding mountains prevent ice flow from the nearby ice sheet into the valleys.

1.2.2 Paleoreconstruction of AIS

Earth underwent a climatic transition from a green-house state to an ice-house state starting from the early-middle Eocene, 50 to 48 Million years ago (Ma), when temperatures began to drop (see Figure 1.4) (Liu et al., 2004). An initial decrease in deep-sea temperatures triggered negative feedback mechanisms which lead to an abrupt cooling at 34 Ma, during the Eocene-Oligocene transition (Zachos et al., 2001), usually referred to as Earlieast Oligocene Glacial Maximum (EOGM) (Zachos et al., 1996). It is around this time that the Antarctic ice sheet was established. EOGM is an excellent example of how a better understanding of past climate

changes can help us forecast the future. In fact, atmospheric CO_2 variation rates during EOGM has been shown to be close to modern day trends (Barrett, 2003), and it has been observed that at the time the partial pressure of atmospheric CO_2 was the primary influence on the overall climate state and variability of AIS volume (Galeotti et al., 2016).

The Antarctic ice sheet has since experienced numerous cycles of advances and retreats as a response to different climatic conditions (Marchant et al., 1993; Miller et al., 2008). During the subsequent 11 million years, temperature decreased progressively and the ice sheet grew in size, as testified by high sedimentation rates along the continental slope of East Antarctica and in deltaic systems on the continental shelf of West Antarctica (Hochmuth et al., 2020). After the Oligocene-Miocene boundary (23 Ma) and up to the mid-Miocene climate transition at 14 Ma, warmer and colder periods followed one another, modifying the ice volume of the ice sheet, which in turn altered the climate system, in a complex feedback system. Ice sheet models have predicted the presence at the time of an Ice Sheet in East Antarctica, which retreated during interglacials, while the West Antarctic Ice Sheet was significantly smaller than today, and it likely collapsed during severely warm interglacials (Gasson et al., 2016).

At 14 Ma, cold climate conditions were established leading ultimately to a new phase of expansion for the AIS and establishing the current conditions of an ice-covered continent. East Antarctica has experienced limited changes since the Mid-Miocene to present time (Marchant et al., 1993; Sugden et al., 2006), while West Antarctica has proven to have a more heterogeneous response to climatic variations (Sugden et al., 2006). A general cooling of Earth's climate continued during the Pliocene (5 to 2.6 Ma) culminating in the beginning of the Quaternary glaciation, which saw the formation of a permanent ice sheet on the North Pole, which survives today in the from of the Greenland Ice Sheet. At this time, the AIS transitioned from a wet-based ice sheet to a cold based one (Levy et al., 2019; Pollard and Deconto, 2020).

Data from the Pleistocene show an extension of the ice on the Antarctic Ice Sheet which in several occasions exceeded present day one; EAIS overrode the Transantarctic Mountains during several episodes of extensive glaciations while WAIS was considerably thicker than at present on several occasions during the Early and Middle Pleistocene (Ingolfsson, 2004, and references therein). Ice from the mid-Pleistocene has survived intact in East Antarctica until today, giving us a detailed record of 8 glacial-interglacial cycles directly from the ice (EPICA Community Members, 2004).

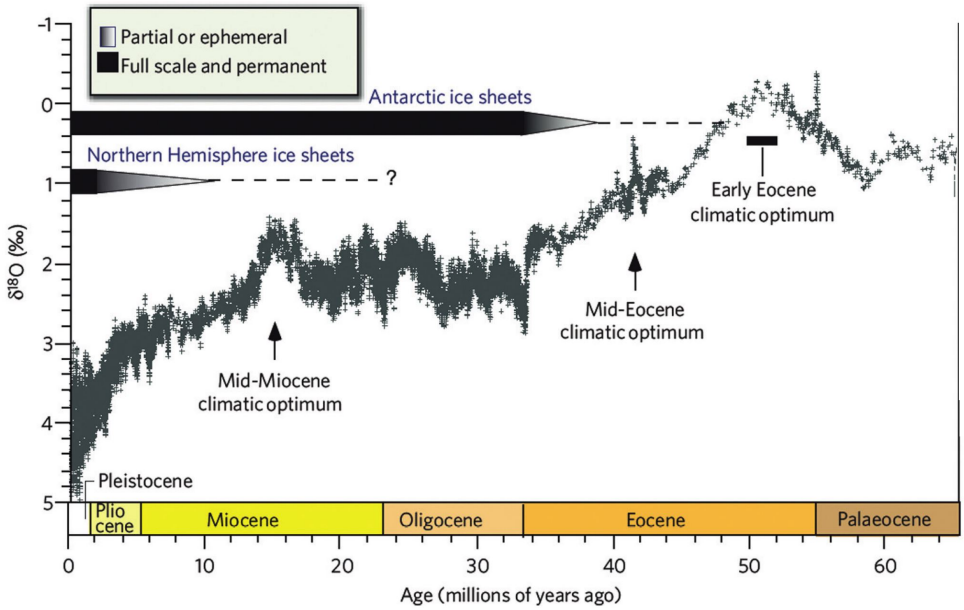

Figure 1.4: Climate from 65 million years ago to present day. The x-axis on the left is a stacked deep-sea benthic foraminiferal oxygen-isotope curve smoothed with a five-point running mean, expressed in parts per thousands (‰). The figure clearly shows the Early Eocene Climatic Optimum and both the Mid-Eocene and Mid-Miocene Climatic Optimums. Adapted from Zachos et al. (2008).

Chapter 2

Ice cores

Ice cores are remarkable archives of past climate and environmental conditions of the Earth, giving us access to information on temperature, greenhouse gases, aerosols, atmospheric circulation patterns, sea-ice extent, volcanic eruptions and solar activity. Furthermore, by synchronization with climatic records from the northern hemisphere, we now have a much better understanding of how climatic changes across the globe are interconnected. In this chapter we will explore how snow transitions to ice and ultimately forms glaciers and ice sheets. We will see how some proxies are interpreted to extract paleoclimatic information, with a special attention on mineral dust. At last, we will retrace the history of deep ice coring in Antarctica and focus on the main features of the Talos Dome drilling site.

2.1 Formation of glacier ice

Snow is a highly porous material made up of single crystals bound in a continuous structure and with a continuously connected pore space. During its transformation, porosity is gradually reduced as grains pack together and recrystallize, and density becomes an exponential function of depth, slowly turning snow to ice. Metamorphism is a complex mechanism, mainly driven by temperature, pressure and time. In dry conditions, when the temperature is always below freezing point, we can hypothesize two ideal situations: 1) the temperature is uniform across the snow pack, or 2) a temperature gradient is present. We must keep in mind that natural conditions will in reality reflect a somehow intermediate condition between the two extremes (Sommerfeld and LaChapelle, 1970). Equi-temperature metamorphism is characterized by a change in structure of the crystal, which is subjected to rounding. This decreases the surface free energy, which is proportional to the ratio between surface area and mass, and is in accordance with the laws of physics: a system will always shift to the lowest possible energy configuration. During an initial phase the snow crystal may break up to form several smaller grains, but in a second phase, to further reduce surface energy, grains grow bigger in size and decrease in number. Temperature-gradient metamorphism leads to the formation of

a particular type of crystals called depth hoar, which consist of large and faceted grains. Because of the temperature gradient, sublimation is favored on the top of the grain whilst deposition is favored on the bottom. This reduces the temperature gradient, which has to be maintained from the outside for the process to continue. In any case, when a threshold of 580-600 kg/m^3 in density is reached (Anderson and Benson, 1963), snow properties change and snow becomes firn. As firn is progressively buried by new snowfalls, pressure becomes the main metamorphic agent. At a density of 800-830 kg/m^3 (Sommerfeld and LaChapelle, 1970) pores close off, losing communication between each other, and the firn by definition becomes ice. Accumulation of ice over the years leads to the formation of a glacier: when the mass of ice reaches a critical thickness, it cannot sustain itself anymore and starts to flow under the action of gravity.

2.2 Ice core proxies

Ice cores are circular sections of ice, extracted vertically from glaciers or ice sheets. They are archives which record climatic information. For example, past atmospheric concentrations can be measured from gas bubbles entrapped in the ice, giving us a direct measure of CO_2 and CH_4 from the past. Other parameters, such as temperature, humidity, volcanic activity, solar activity and sea ice extent, have to be measured indirectly through the use of proxies. Proxies are physical, chemical or biological materials which can be linked to climatic parameters such as temperature and humidity. By understanding and calibrating the relationship between the measurable material and the climatic parameter, we obtain an indirect measure of said parameter. In Fig. 2.1 we present an example of different parameters measured in the EPICA Dome C ice core (Lambert et al., 2008). Eight glacial/interglacial cycles covering the last 800kyrs can be seen in the figure, showing good correlations between proxy measurements for temperature ($\delta^{18}O$) and humidity (δD), gas concentrations (CO_2 and CH_4) and dust records.

Here we will briefly discuss the use of the stable isotopes of water, which are the main proxy for temperature. Section 2.3 will discuss in detail the use of mineral dust as a climatic proxy in antarctic ice cores.

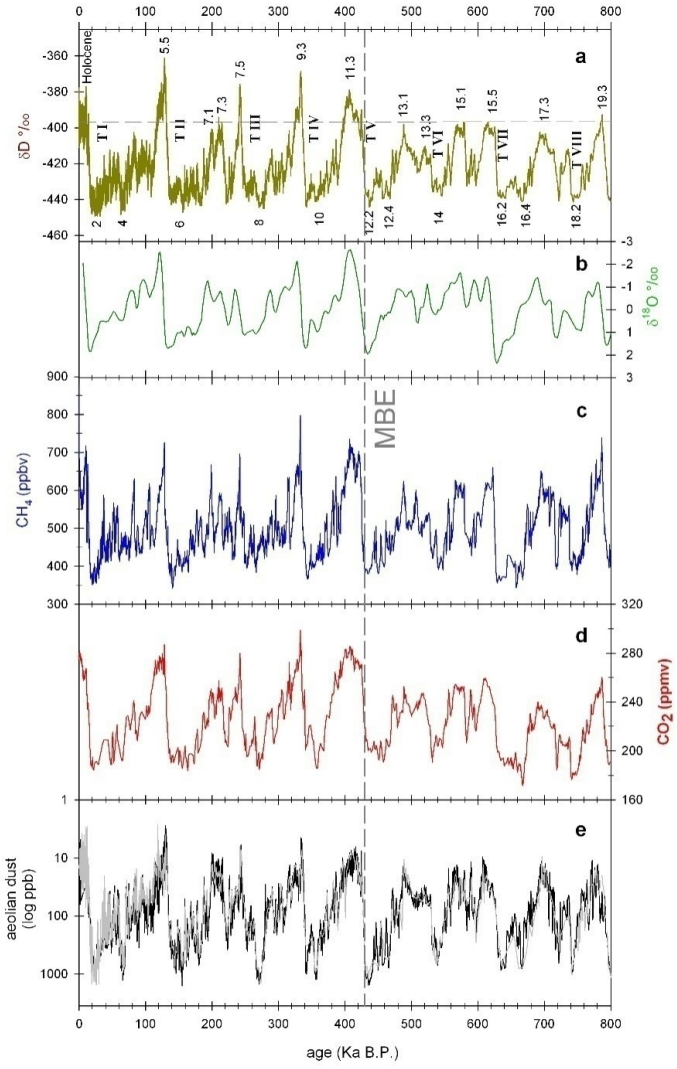

Figure 2.1: Main features from the EPICA Dome C ice core plotted against age (in Ka B.P.). Dotted line indicates the Mid-Brunhes Event, which marks a shift in the amplitude of glacial/interglacial cycles. In particular: a) δD with numbers indicating Marine Istopic Stages (2-18.3) and glacial terminations (TI-TVIII) b) $\delta^{18}O$ c) Methane record (ppbv) d) Carbon dioxide record (ppmv) e) Aeolian dust (log ppb). Redrawn from Lambert et al. (2008).

2.2.1 Stable Isotopes of Water

Among the most used proxies, not only in ice cores but also in a range of other natural archives, we find the study of the stable isotopes of water. These provide information on past temperature and humidity values. Stable isotope profiles can also be used to estimate past changes in accumulation through inversed glaciological dating methods (Parrenin et al., 2001). The relationship between stable isotopes and accumulation also forms the basis for the dating of deep ice cores, through the modeling of accumulation and ice thinning (Masson-Delmotte et al., 2008).

Isotopes are atoms of the same element, which differ by the number of neutrons, and thus in their mass. This does not alter their chemical properties, but modifies their physical behavior. In nature, isotopes exists in fixed relative proportions, but physical processes may modify them locally. Oxygen has three stable isotopes, ^{16}O, ^{17}O, ^{18}O, and Hydrogen has two, ^{1}H and ^{2}H, leading to nine possible isotopic combination for water molecules. Of these, only two are important for paleoclimatic reconstructions: $^{1}H^{2}H^{16}O$ and $^{1}H_{2}^{18}O$, which we will refer to as "heavy" water molecules. The vapor pressure at which a molecule may evaporate or precipitate also depends on the mass of the molecule: a "light" water molecule ($^{1}H_{2}^{16}O$) will evaporate more easily than a heavy one, leading to the formation of vapor which is depleted in heavy isotopes with respect to the original water source. Vice versa, heavy molecules will condensate more easily, leading to precipitations which are initially enriched in heavy isotopes.

Essentially, the ratio of $^{18}O/\ ^{16}O$ and of $^{2}H/\ ^{1}H$ is a function of temperature at the time of condensation (Johnsen et al., 1972). This ratio is measured in the sample and compared with a water standard in order to calculate two parameters: $\delta^{18}O$ and δD. The spatial variations of these two parameters are strongly related to the spatial variation of temperature, which in turn is strongly related to the distance from the open ocean, latitude, elevation, and atmospheric circulation (Masson-Delmotte et al., 2008). For an accurate interpretation of the climatic signal it is necessary to correctly consider all of these factors.

Moreover, $\delta^{18}O$ and δD are linked by a strong relationship which was empirically derived and can be expressed as Equation 2.1 (Craig, 1961).

$$\delta D = 8\delta^{18}O + 10 \tag{2.1}$$

This relationship is valid globally under equilibrium conditions. The offset value (d) can be derived from Equation 2.1:

$$d = \delta D - 8\delta^{18}O \tag{2.2}$$

d is referred to as the deuterium excess and varies under non equilibrium conditions, giving us further information on humidity, wind speed and sea surface temperatures (Jouzel et al., 1982; Petit et al., 1991).

2.3 Mineral Dust in Antarctica

Dust and climate share a strong but complex relationship with each other. On one hand, dust has direct effects on climate (Maher et al., 2010) as it interacts with solar radiation influencing the Earth's radiative budget (Tegen, 2003), and indirect effects linked to its role in the formation of clouds and to its influence in atmospheric chemistry. To date, the net contribution of aerosols to climate forcing is still prone to high uncertainties (Huang et al., 2013). On the other hand, climate itself can strongly affect production, transport and deposition of dust (Mahowald et al., 2006). It is well known that dust fluxes respond to the transition from glacial to interglacial regimes (Petit et al., 1999; EPICA Community Members, 2004; Jouzel et al., 2007; Lambert et al., 2008).

Deposition of dust on the Antarctic continent is controlled by a number of factors, such as the primary supply of dust particles from the continents (Petit et al., 1999), the long range transport, the hydrological cycle and the snow accumulation rate (Lambert et al., 2008; Wegner et al., 2015). Different aspects provide different kinds of information: total dust deposition is a proxy of climate conditions at the dust source (Fischer et al., 2007), particle size distribution reflects transport efficiency (Wegner et al., 2015) and chemical composition provides information on the geographical provenance (Delmonte et al., 2010a). Thus, it can be used to reconstruct past patterns and intensities of atmospheric circulation at hemispherical scale (Delmonte et al., 2002; Gabrielli et al., 2005a; Vallelonga et al., 2010; Gabrielli et al., 2010; Gili et al., 2017).

2.3.1 Dust Flux and Particle Size Distribution

As mentioned before, a strong correlation between dust fluxes and temperatures exists during glacial periods. During these periods, dust fluxes have shown to be 25 times stronger than in interglacials (Petit et al., 1999; Lambert et al., 2008). The cause of this lies in a strengthening in the deflation of dust from source areas, linked to vegetation patterns and soil humidity (Rothlisberger et al., 2003), and in a more efficient transport to deposition sites in Antarctica (Petit et al., 1999; Vallelonga and Svensson, 2014; Delmonte et al., 2017). This strong correlation with temperature implies that the intensity of dust flux can be used as an indicator of Southern Ocean climatic variability at millennial scale, at higher resolutions than the δD in deeper parts of ice cores (Lambert et al., 2012). It has also been observed that during transitions from glacial to interglacial periods, dust levels usually drop 4000 years before temperature and CO_2, suggesting changes in wind circulation patterns and in the hydrological cycle at the dust source (Lambert et al., 2012).

The mass-size distribution of dust particles in East Antarctica is usually well sorted around a mean mass diameter of 2 µm and rarely exceeds 5 µm (Delmonte et al., 2004). This is compatible with prolonged transport in the atmosphere, indicating remote sources as the major dust input to inner Antarctica. At peripheral sites, such as Taylor Dome, Talos Dome and at the WAIS divide ice core site, dust records with higher contributions of coarser particles has been identified (Aarons et al., 2016; Albani et al., 2012; Koffman et al., 2014b). This points to the presence of local dust sources which become detectable especially during interglacial periods

when the atmospheric circulation is dampened. This is also confirmed by dust provenance studies (see 2.3.2).

2.3.2 Dust Composition

Geochemical analysis of dust in ice cores can be used to trace dust provenance using various parameters. The use of enrichment factors is a simple and intuitive way to determine the crustal provenance of dust particles, as was done for the first time in Antarctic ice cores by Petit et al. (1981). A geographical estimation of dust sources is possible through the study of the isotopic signature ($^{87}Sr/^{86}Sr$ vs $^{143}Nd/^{143}Nd$) of dust inside the ice and in Potential Source Areas (PSA) (Grousset et al., 1992; Basile et al., 1997). Similarly, lead isotopes have also been used as dust provenance tracers (Vallelonga et al., 2002). Patterns of rare earth elements concentrations, which are widely used geochemical tracers due to their low environmental mobility, have also been applied to paleoclimatic reconstruction on ice core records (Gabrielli et al., 2010).

South America has been broadly recognized as the main source area for glacial dust across Eastern Antarctica (Basile et al., 1997; Delmonte et al., 2008, 2010a; Gili et al., 2017), both during glacial and interglacial periods (Paleari et al., 2019), although for these latter a more complicate pattern emerges. Actually, for the Holocene and the earlier interglacial, geochemical fingerprints do not allow excluding Australia as a potential contributor to dust input (De Deckker et al., 2010; Revel-rolland et al., 2006; Delmonte et al., 2008; De Deckker, 2020). At peripheral sites, like Talos Dome, located close to high elevation ice-free areas, local sources also become relevant, especially during warm periods when the remote dust flux is at minimum (Delmonte et al., 2010b; Bory et al., 2010; Aarons et al., 2016).

2.4 Antarctic ice cores

2.4.1 History of Antarctic Ice Cores

The first complete ice core, which reached bedrock, was drilled at Camp Century, Greenland, from 1960 to 1966. The site was chosen due to its easy accessibility as part of a "city under the ice" experiment during the cold war (Jouzel, 2013). Shortly after, in 1968, the first deep drilling was completed in Antarctica, at Byrd Station. Deep drillings went on in both ice sheets. The major differences between ice cores from Greenland and Antarctica are the ice flow velocity and the mean snow precipitation. In Greenland, ice flows quite fast and accumulations rates are relatively high if compared to Antarctica. This translates to a higher resolution record but also a challenge in finding undisturbed records. In Antarctica, accumulation is lower and ice flow is slower, allowing to retrieve older and deeper records, especially in EAIS where accumulation rates are very low and the ice thickness is maximum. The ice core drilled at Vostok, East Antarctica, in 1999 is the deepest to date reaching 3623 m of depth. This was dated at 420 000 years B.P., corresponding to a depth of 3310 m. (Petit et al., 1999). The EPICA-Dome C (EDC) ice core, also drilled in East Antarctica, reached bedrock at 3260 m of

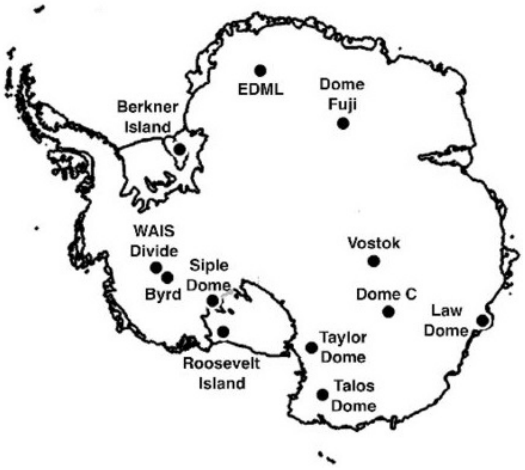

Figure 2.2: Location of main deep ice core drillings in Antarctica. Adapted from Neff (2014).

depth in 2005 and provided the oldest ice record covering 800 000 years of climate history (EPICA Community member 2004, jouzel 2007a). Table 2.1 and Figure 2.2 show the principal deep drillings in Antarctica.

Table 2.1: Main deep ice cores drilled in Antarctica.

Site	Last year of drilling	Bottom depth (m)	Reconstructed age (years B.P.)	References
Byrd	1968	2164	50 000	(Hammer et al., 1994)
Law Dome	1993	1196	2000	(Morgan et al., 1997; MacFarling Meure et al., 2006)
Taylor Dome	1994	554	230 000	(Steig et al., 1998; Grootes et al., 2001)
Vostok	1996	3623	420 000	(Petit et al., 1999)
Dome Fuji	1996	2503	330 000	(ice core research group, 1998; Watanabe et al., 2003)
Siple Dome	1999	1004	98 000	(Nereson et al., 1996; Taylor et al., 2004; Brook et al., 2005)
Dome C	2005	3260	800 000	(EPICA Community Members, 2004)
Berkner Island	2005	948	120 000	(Mulvaney et al., 2007)
Dronning Maud Land	2006	2760	150 000	(EPICA Community Members, 2006)
Dome Fuji	2006	3035	720 000	(Motoyama, 2007; Kawamura et al., 2017)
Talos Dome	2007	1620	150 000	(Stenni et al., 2011)
WAIS divide	2011	3405	62 000	(Fudge et al., 2013)
Roosevelt Island	2012	763	83 000	(Lee et al., 2020)

2.4.2 Talos Dome

Talos Dome is an ice dome situated in peripheral East Antarctica (159°04′21″ E, 72°47′1″ S; 2315 m asl) (Frezzotti et al., 2004). Due to its vicinity to the Southern Ocean and the Ross Sea, it experiences relatively high accumulation rates (87 ± 8 mm/year we) (Scarchilli et al., 2011). This permitted the reconstruction at relatively high resolution of the last climatic cycle, reaching the penultimate interglacial (MIS5) (Veres et al., 2013). TALDICE is synchronized to the AICC2012 chronology, which in turn is tied to the Greenland chronology, permitting a global scale reconstruction of climatic processes (Bazin et al., 2013; Veres et al., 2013).

During glacial periods, Talos Dome exhibits similar dust isotopic fingerprints, and comparable dust flux and grain distribution, to those of inner sites, such as Vostok and Dome C. This points to a common and remote source for East Antarctica, which has mainly been identified

Figure 2.3: Mesa Range, Northern Victoria Land, East Antarctica. Adapted from Damaske et al. (2014).

in the Patagonia region (Delmonte et al., 2010a,b, 2013). During interglacials major isotopic differences between Talos Dome and central Antarctica point to a shift in the dominant dust sources. The presence of a relevant fraction of coarser particles, having diameter larger than 5 µm, which are not present in dust records from inner sites of Antarctica, suggest that at Talos Dome local sources are important, particularly during Holocene, and can be used as proxy for local atmospheric circulation changes. The site is in fact located near high altitude, ice-free sites in Northern Victoria Land, such as the Mesa Range for example, located about 150 km away in an E–SE direction. Under such conditions, strong atmospheric dust uplift is not necessary for mineral aerosol transport to the site, while only wind direction is important (Delmonte et al., 2010b).

2.4.3 Future and challenges of deep ice core drillings

In the last decade international efforts have focused on the search for an appropriate site for a new deep ice core drilling. The objective is to expand the ice core climatic record from the current 800 kyr to 1.5 million. This would cover the mid-Pleistocene transition, a climatic event which is currently poorly understood. Approximately 0.9-1.2 Ma Earth's climate experienced a change of pace in the glacial/interglacial cycles, which went from a 41 kyr cycle to the current 100 kyr. This has been documented by records of benthic foraminifera (Lisiecki and Raymo, 2005), but the hope is that the higher resolution generally provided by ice core will shed light on what forced this transition.

East Antarctica, where the *current* oldest ice was drilled, has always been considered the best candidate for a new drilling site for obvious reasons. But the dynamic nature of ice sheets

and the influence of geothermal heat make it difficult for such old ice to survive, despite the fact that the East Antarctic ice sheet has existed continuously for much longer than 1.5 million years (Fischer et al., 2013). Ice thickness, which according to models must be over 2000 m, is not the only parameter to consider, and may be in fact counterproductive in some cases as too large ice thickness may lead to excessive bottom melting (Fischer et al., 2013; Liefferinge and Pattyn, 2013). Rough bedrock topographies and surface velocities above 2 m/yr must also be avoided (Fischer et al., 2013; Liefferinge and Pattyn, 2013). Sites in the vicinity of Dome Fuji and Dome C were identified as the most suitable for Oldest ice drilling (Van Liefferinge et al., 2018), and finally the European Project for Ice Coring in Antarctica (EPICA) selected Little Dome C as the best site and was set to start drilling during 2020/2021 season.

Selection of the most appropriate site is not the only challenge concerning the quest for Oldest ice. Spectral analysis from the EPICA Dome C core have revealed enhanced isotopic diffusion, high values of ice grain size and strongly smoothed records of soluble ions occurring in the deepest ice (Durand et al., 2009; Pol et al., 2010). Evidence of clear anomalies (Tison et al., 2015; Faria et al., 2010) and possible in situ processes have been documented in deep ice samples (De Angelis et al., 2013; Baccolo et al., 2018a, 2021) possibly modifying both physical and chemical features. It is clear that these processes have to be fully understood in order to correctly interpret the climatic signal from a new deep ice core.

Chapter 3

Material and Methods

3.1 Objectives of this work

This work was conceived with the main objective of enhancing our comprehension of deep ice processes through the use of an array of different techniques applied to the Talos Dome ice core. In particular, our aims were:

- To study chemical and physical anomalies present in the deeper part of the dust record
- To confirm the existence of post-depositional processes which may alter the climatic signal embedded in deep ice
- To observe how different elements partition between soluble and insoluble phase, at different depths of the ice core
- To link the geochemical patterns of the considered elements to the main climatic oscillations covered by TALDICE

The Talos Dome ice core was drilled between 2005 and 2007 from a peripheral dome in Eastern Antarctica, in the framework of the European project "TALDICE" . The ice core is 1620 m long and covers more than 250k years of climate history (Stenni et al., 2011; Bazin et al., 2013; Veres et al., 2013). We prepared samples from the entire length of the ice core, with a focus on depths lower than 1450 m, which hereafter we will refer to as the deep section of the core. This section has not yet been dated due to anomalies in the $\delta^{18}O$ record (Bazin et al., 2013) and to the presence of anomalously large ice crystals (Montagnat et al., 2012), which questioned the integrity of the stratigraphy.
During this work, the published dust record (Delmonte et al., 2010b; Albani et al., 2012) has been integrated in its deepest part. A geochemical investigation was carried out using ICP-SFMS and INAA techniques, mainly to study the fractionation of elements between soluble and insoluble phase and how this may change at different climatic stages. Samples were also prepared for single particle analysis with EDS-SEM to investigate the presence of aggregates

in the deep part and study their elemental composition.

3.2 Coulter Counter

Coulter Counter measures the volume and size of solid particles inside the sample, and thus permits an estimate of the equivalent spherical volume of the particle. The sample is placed in contact with a capillar tube with a small aperture through which the sample passes while an electric potential difference is applied. As dust particles pass through the opening, the change in electrical conductivity of the circuit is measured. The intensity of the potential variations is proportional to the volume of the particle.
Two Beckman Multisizers (4 and 4e), present at University of Milano-Bicocca, were used, equipped with a capillar tube with a 30 µm aperture, which allows the detection of particles between 0.6 and 18 µm.

3.2.1 Sample preparation

We analyzed 125 samples belonging to the deep part of the ice core. Each sample was decontaminated using three subsequent baths of ultrapure water, following the procedure described in Delmonte et al. (2002). All ultrapure water used in this work is produced through a Millipore Milli-Q Reference system and has a resistivity of 18.2 MΩ at 25 °C. Samples were melted at room temperature in polypropylene centrifuge tubes, precleaned using ultrapure water. For analysis, samples were then transferred in precleaned polystyrene accuvettes, where an electrolyte solution (NaCl, 20%) was added until a concentration of about 1-2% was reached. Each sample was measured twice, so that the final data is represented by the mean value of the two measurements. Blanks were measured daily together with the samples.

3.2.2 Sonication

After Coulter Counter analysis, several samples were placed in an ultrasonic bath in order to study the presence of aggregates. Here samples are exposed to high frequency sound waves (ultrasounds) which are diffused through water, and had previously shown the ability to break aggregates in ice core samples (De Angelis et al., 2013). Various tests were made to assess the validity of the technique, by changing: the type of container, the positioning of the sample inside the ultrasonic bath, the time passed before changing the water and the sonication time. After sonication, samples were immediately measured again with the Coulter Counter.

3.3 SEM-EDS

We prepared ten samples for analysis with a Scanning Electron Microscope (SEM) coupled with energy-dispersive X-ray spectroscopy (EDS). The latter relies on the interaction of the sample with an X-ray beam, which produces an emission spectrum. The instrument measures X-rays generated by excited electrons returning to their ground state, which are characteristic

of the atomic structure and thus permit to know the elemental composition of the sample.
Samples were decontaminated and melted following the same procedure used for Coulter Counter measurements. An aliquot was used for Coulter Counter measurements, while the remaining one was filtered using a Millipore vacuum-driven filtration system. Dust was collected using polycarbonate filters (0.4 μm cutoff) which were then mounted on specimen stubs for SEM measurement. Before analysis, samples need to be coated with an ultra thin layer of electrical conducting material. This is done to avoid the sample becoming electrically charged, which would ultimately degrade the resolving power and analytical capabilities of the system (Goldstein et al., 1992). We used grafite for samples that required EDS, since carbon is transparent to the electron beam but still conductive. Some samples were coated with gold to have a better imaging resolution.
The University of Milano-Bicocca is equipped with a Zeiss Gemini 500 SEMs coupled with a QUANTAX EDS 4000 microanalysis system. For the gold coating, a Sputter Coater S150B was used.
The prepared samples were all from the deep section of the ice core, ranging from 1504 m of depth to 1610 m, except for two Holocene samples, which were used for comparison. Due to the low concentration of dust in the Holocene samples, these were prepared merging several adjacent samples.

3.4 INAA

Neutron activation is a nuclear technique used in elemental analysis, which exploits the ability of atomic nuclei to capture neutrons when exposed to a neutron flux. When the product of this nuclear reaction is an unstable nuclide, its radioactive decay will emit gamma rays and particles which can be detected, allowing the quantification of the original element concentration in the sample. After irradiation the sample can either be chemically treated to separate the various elements (Radiochemical Neutron Activation Analysis - RNAA) or kept intact and analyzed through high-energy resolution equipment (Instrumental Neutron Activation Analysis - INAA). We will deal with the latter. This technique was used early on in the analysis of ice core impurities (Rauter and Stauffer, 1977; Petit et al., 1981; Angelis et al., 1987; Legrand and Delmas, 1988; Koyama and Fujii, 1988) but was outcompeted by other elemental analysis techniques such as ICP-SFMS, CFA, PIXE and XRF. It was only recently that neutron activation was applied again to polar ice cores (Baccolo et al., 2015, 2016a). Its main advantages are the fact that it does not require destruction of the sample and that it poses a low risk of contamination as the sample treatment is quite simple. Following Greenberg et al. (2011), we can divide INAA into three steps:

1. Activation of the samples via irradiation using a neutron flux.
2. Measurement of the subsequent gamma radiation using germanium detectors.
3. Identification of radionuclides and associated elements by analyzing the resulting gamma spectra.

Each atomic nucleus, when exposed to a neutron flux, has a certain probability of capturing a neutron, expressed by its neutron cross section (σ). When this happens, the nucleus will change its atomic mass and may undergo different reactions, the most common of which is the immediate emission of a gamma prompt radiation. An alternative is the emission of a proton. These reactions are commonly indicated with (n,γ) and (n,p). All reactions considered in this work are reported in Table 3.1.

If the newly formed nuclide is unstable, it will undergo radioactive decay by emitting ionizing radiation in order to return to its less energetic, more stable, asset. Ionizing radiation can take different forms, but here we will only consider γ-radiation which due to its nature provides a straightforward identification of the radionuclide via its emitted energy. Each radioactive decay is characterized by a half-life ($t_{1/2}$), which gives us the statistical probability that a certain nucleus will decay in a certain time interval. This will influence the interval of time needed between sample irradiation and sample measurement in order to detect the different radionuclides of interest. To cover the largest number of elements, we decided to measure the samples in three different time intervals: immediately after irradiation for short lived radionuclides ($<$ 3 h), after one week for medium lived radionuclides and after one month for long lived radionuclides. Gamma spectra are analyzed by fitting each energy peak with a gaussian function and subtracting its background using the most appropriate polynomial function.

3.4.1 Apparatus

The Laboratory for Applied Nuclear energy (LENA) at University of Pavia is equipped with a 250 kW Triga Mark II reactor, available for irradiations. For short irradiations ($<$15 min) we used the "Rabbit" channel which has a neutron flux of $7.40 \pm 0.95 \times 10^{12}$ s^{-1} cm^{-2}, while for long irradiations (60 h) we used the "Lazy Susan" channel, which has a neutron flux of $2.40 \pm 0.24 \times 10^{12}$ s^{-1} cm^{-2} (Borio di Tigliole et al., 2014). Samples were later analyzed with p-type high purity germanium detectors specifically designed for low background measurements (Salvini et al., 2006). A coaxial germanium detector was used at LENA for samples coming out of the "Rabbit" channel; its relative efficiency is 30% and its energy resolution at the 1.332 MeV is 1.8 keV FWHM. A well-type germanium detector installed at the Radioactivity Laboratory of the University of Milano-Bicocca was used after the "Lazy Susan" irradiations; it has a very high efficiency with a total active volume of 350 cm^3 and its energy resolution at the 1.332 MeV is 2.2 keV FWHM.

Table 3.1: Nuclear reactions used for the determination of elements, with associated main γ energies used during the analysis of the spectra, reported half time, and used channel. Data from Chu et al. (1999)

Element	Reaction	Energy (keV)	Half Time	Channel
Al	^{27}Al (n,γ) ^{28}Al	1779	2.3 min	Rabbit
As	^{75}As (n,γ) ^{76}As	559.1	1 d	Lazy Susan
Ba	^{130}Ba (n,γ) ^{131}Ba	216.1 - 373.2	11.5 d	Lazy Susan
Ca	^{46}Ca (n,γ) ^{47}Ca $\xrightarrow{\beta^-}$ ^{47}Sc	159.4	3.3 d	Lazy Susan
Ce	^{140}Ce (n,γ) ^{141}Ce	145.4	32.5 d	Lazy Susan
Co	^{59}Co (n,γ) ^{60}Co	1173.2 - 1332.5	5.3 y	Lazy Susan
Cr	^{50}Cr (n,γ) ^{51}Cr	320.1	27.7 d	Lazy Susan
Cs	^{133}Cs (n,γ) ^{134}Cs	604.7 - 795.9	2.1 y	Lazy Susan
Eu	^{151}Eu (n,γ) ^{152}Eu	344.3 - 1408	13.5 y	Lazy Susan
Fe	^{58}Fe (n,γ) ^{59}Fe	1099.3 - 1291.6	44.5 d	Lazy Susan
Hf	^{180}Hf (n,γ) ^{181}Hf	345.9 - 482.2	42.4 d	Lazy Susan
Hg	^{202}Hg (n,γ) ^{203}Hg	279.2	46.6 d	Lazy Susan
Ho	^{165}Ho (n,γ) ^{166}Ho	80.6	26.8 h	Lazy Susan
K	^{41}K (n,γ) ^{42}K	1524.7	12.4 h	Lazy Susan
La	^{139}La (n,γ) ^{140}La	815.8 - 1596.2	1.7 d	Lazy Susan
Lu	^{176}Lu (n,γ) ^{177}Lu	208.4	6.7 d	Lazy Susan
Mg	^{26}Mg (n,γ) ^{27}Mg	843.7	9.5 min	Rabbit
Mn	^{55}Mn (n,γ) ^{56}Mn	846.8 - 1810.7	2.6 h	Rabbit
Na	^{23}Na (n,γ) ^{24}Na	1368.6 - 2754	15 h	Lazy Susan
Nd	^{146}Nd (n,γ) ^{147}Nd	91.1 - 531	11 d	Lazy Susan
Ni	^{58}Ni (n,p) ^{58}Co	810.8	70.9 d	Lazy Susan
Rb	^{85}Rb (n,γ) ^{86}Rb	1076.7	18.6 d	Lazy Susan
Sb	^{121}Sb (n,γ) ^{122}Sb	564.1	2.7 d	Lazy Susan
Sc	^{45}Sc (n,γ) ^{46}Sc	889.3 - 1120.6	83.8 d	Lazy Susan
Se	^{74}Se (n,γ) ^{75}Se	400.7	119.8 d	Lazy Susan
Si	^{29}Si (n,γ) ^{29}Al	1273.4	6.6 min	Rabbit
Sm	^{152}Sm (n,γ) ^{153}Sm	103.2	46.3 h	Lazy Susan
Sr	^{84}Sr (n,γ) ^{85}Sr	514	64.8 d	Lazy Susan
Ta	^{181}Ta (n,γ) ^{182}Ta	1189.1	114.4 d	Lazy Susan
Tb	^{159}Tb (n,γ) ^{160}Tb	879.4 - 1178	72.3 d	Lazy Susan
Th	^{232}Th (n,γ) ^{233}Th $\xrightarrow{\beta^-}$ 233Pa	300.3 - 312.2	27 d	Lazy Susan
Ti	^{50}Ti (n,γ) ^{51}Ti	320.1	5.8 min	Rabbit
Tm	^{169}Tm (n,γ) ^{170}Tm	84.3	128.6 d	Lazy Susan
U	^{238}U(n,γ) ^{239}U $\xrightarrow{\beta^-}$ 239Np	106.1 - 277.6	2.4 d	Lazy Susan
V	^{51}V (n,γ) ^{52}V	1434.1	3.7 min	Rabbit
W	^{186}W (n,γ) ^{187}W	618.4 - 695.8	23.7 h	Lazy Susan
Yb	^{174}Yb (n,γ) ^{175}Yb	282.5 - 396.3	4.2 d	Lazy Susan
Zn	^{64}Zr (n,γ) ^{65}Zr	1115.5	244.3 d	Lazy Susan
Zr	^{96}Zr (n,γ) ^{97}Zr	743.4	16.9 h	Lazy Susan

3.4.2 Reference Materials and INAA Calculations

In order to calculate the final element concentration we used a relative method. This implies the use of certified reference materials (RM) and allows to neglect a series of parameters such as isotopic abundances, branching ratios, neutron capture cross sections, neutron flux and detector efficiencies. Reference materials have a known composition, and are prepared and analyzed using the same methodology as the samples. Nine RMs were used for this work, as reported in detail in Table 3.2.

Table 3.2: Reference Material

Name	Type	Elements
STD-Al	Pure Al	Al
STD-Si	Pure Si	Si
STD1	Liquid multielemental	Mg, Ti
STD2	Liquid multielemental	Al, Mn, V
STD3	Soil	Ag, Al, As, Au, B, Ba, Ca, Cd, Ce, Co, Cr, Cs, Cu, Dy, Eu, Fe, Gd, Hf, Hg, In, K, La, Lu, Mg, Mn, Na, Nd, Ni, P, Pb, Rb, Sb, Sc, Se, Si, Sm, Sr, Ta, Tb, Th, Ti, Tl, U, V, W, Yb, Zn, Zr
STD4	Andesite	Al, Ba, Be, Ca, Ce, Co, Cr, Cu, Dy, Fe, Gd, K, La, Mg, Mn, Na, Nb, Nd, Ni, P, Pb, Pr, Rb, Sc, Si, Sr, Th, Ti, U, V, Y, Yb, Zn, Zr
STD5	Soil	Al, As, B, Ba, Ca, Cd, Ce, Co, Cr, Cs, Cu, Dy, Eu, Fe, Gd, Hf, Hg, K, La, Lu, Mg, Mn, Na, Nd, Ni, P, Pb, Rb, Sb, Sc, Se, Si, Sm, Sr, Ta, Tb, Th, Ti, Tl, U, V, Yb, Zn, Zr
STD6	Basalt	Al, Ba, Ca, Ce, Co, Cr, Eu, Fe, Ga, Gd, K, La, Mg, Mn, Mo, Na, Nd, P, Rb, Sc, Si, Sr, Th, Ti, U, V, Y, Yb, Zn, Zr
STD7	Soil	Al, As, Au, B, Ba, Be, Bi, Br, Ca, Cd, Ce, Cl, Co, Cr, Cs, Cu, Dy, Er, Eu, Fe, Ga, Gd, Ge, Hf, Hg, Ho, I, In, K, La, Li, Lu, Mg, Mn, Mo, Na, Nb, Nd, Ni, P, Pb, Pr, Rb, S, Sb, Sc, Se, Si, Sm, Sn, Sr, Ta, Tb, Th, Ti, Tl, Tm, U, V, W, Y, Yb, Zn, Zr

STD1 and STD2 were prepared by using adsorbent paper to which the liquid RM was added; these were irradiated in the "Rabbit" channel. For short lived radionuclides it was also necessary to prepare a pure Al and a pure Si reference to correct some interferences. ^{28}Al can be in fact produced by two reactions: ^{27}Al (n,γ) ^{28}Al and ^{28}Si (n,p) ^{28}Al; similarly ^{27}Mg can be produce by the reaction ^{26}Mg (n,γ) ^{27}Mg or by ^{27}Al (n,p) ^{27}Mg. The irradiation of pure Al and Si permits the quantification of the contribution of the additional reaction to the final budget of the element. STD3 was prepared using a certified soil and was used both for short and long lived radionuclides. The remaining RMs, prepared from certified soils and powdered rocks, were used for long lived radionuclides.

Because several certified elements overlap between the chosen reference materials, we were able to evaluate the accuracy of the measurement. After calculating the Specific Activity for each element in each reference material, the mean and its standard deviation were calculated. When the uncertainty was higher than 20%, the measurement was not considered reliable and the element was discarded. This was the case for Mg, W and Zr, which were not considered in the final results.

Before we introduce the equations used in INAA calculations, it is necessary to explain the concept of dead time during the acquisition of a spectrum. Dead time is an interval, usually a small fraction of a second, in which the detector is busy acquiring the pulse it has just received and is therefore not acquiring. This leads to the definition of a real time (t_r), which is the time that has actually passed between the start and the end of the acquisition, and a live time (t_l), which is the real time minus the dead time. Both of these will be used in the following calculations.

The specific activity of the RM [counts $\cdot s^{-1} \cdot g^{-1}$] is calculated following Eq. 3.1,

$$A_{spec}(RM) = \frac{A/t_l * e^{\lambda * t_d} * K_a}{m} \tag{3.1}$$

where:

A = integral of the considered photopeak
t_l = live time
λ = decay constant for the considered radionuclide
t_d = time passed between irradiation of the sample and acquisition of the spectrum
m = mass of the considered element present in the RM
K_a = correction factor

K_a only becomes relevant when the real time and the half life are comparable, as it accounts for the radioactive decay which occurs during the acquisition of the spectrum and is calculated following Equation 3.2.

$$K_a = \frac{\lambda * t_r}{1 - e^{-\lambda * t_r}} \tag{3.2}$$

where:

t_r = real time

The specific activity of the sample [counts $\cdot s^{-1} \cdot g^{-1}$] is calculated following Eq. 3.3, similarly to the RM.

$$A_{spec}(sample) = A/t_l * e^{\lambda * t_d} * K_a * K_i \tag{3.3}$$

K_i is another correction factor which accounts for the different irradiation time of sample and RM, and is calculated following Equation 3.4.

$$K_i = \frac{1 - e^{-\lambda * t_i(sample)}}{1 - e^{-\lambda * t_i(RM)}} \tag{3.4}$$

where:

$t_i(sample)$ = irradiation time of sample
$t_i(RM)$ = irradiation time of RM

Finally, the concentration [pg/ml] of the considered element in the sample is calculated following Equation 3.5.

$$C_{sample} = \frac{A_{spec}(sample)}{A_{spec}(RM)} * \frac{1}{V(sample)} \tag{3.5}$$

where:

$V(sample)$ = filtered volume of sample

We refer to Greenberg et al. (2011) and Baccolo et al. (2016a) for a more extensive description of the procedure.

3.4.3 Sample preparation

Four samples from the deep part of the ice core were prepared during the course of this project; these were considered together with twelve other samples from the same ice core previously analyzed by our research group, obtaining a final set of sixteen samples which span the entire length of the ice core. Table 3.3 reports details for all the samples and Fig. 3.1 reports a flow scheme depicting sample preparation.

The preparation procedure was the same for all the samples. To avoid any contamination samples were prepared in a class 1000 clean room. 81 initial samples, each 25 cm long and spanning from 1490 to 1590 m of depth, were selected. Samples were decontaminated and melted following the same procedure used for Coulter Counter analysis. An aliquot of the sample was used to determine the mass dust of the sample through Coulter Counter analysis. The remaining aliquot of each sample was filtered using a vacuum driven Millipore filtration system, merging several adjacent samples together in order to obtain ad adequate amount of dust on each filter. Approximately 20 samples covering the depth range indicated in Table 3.3 were merged together for each INAA sample. Dust was collected on PTFE filters (13mm diameter, 0.4 µm cutoff) and stored in polyethylene vials. Both the filters and the vials underwent several weeks of an acid bath prepared with hyper pure HNO_3 at 5%.

Table 3.3: INAA Samples

Sample	Depth (m)	Age (ky B.P.)	Dust mass (μg)	Filtered Volume (ml)
T1	439-529	6.3-8.3	29 $\pm$ 2	580
T2	531-649	8.3-11.1	32 $\pm$ 2	1048
T3	669-798	11.6-16.3	29 $\pm$ 2	676
T4	802-813	16.5-17.1	32 $\pm$ 2	187
T5	816-903	17.3-25	34 $\pm$ 2	145
T6	906-931	25.4-28.1	37 $\pm$ 2	120
T7	939-957	28.9-30.6	36 $\pm$ 2	151
T8	1067-1199	39.6-51.4	42 $\pm$ 3	542
T9	1210-1255	52.8-59.3	17 $\pm$ 1	198
T10	1259-1298	59.8-70.1	28 $\pm$ 3	199
T11	1423-1441	136.5- unknown	30 $\pm$ 2	204
T12	1445-1477	unknown	31 $\pm$ 3	280
T13	1489-1512	unknown	59 $\pm$ 12	378
T14	1513-1530	unknown	34 $\pm$ 10	238
T15	1535-1552	unknown	32 $\pm$ 8	239
T16	1560-1590	unknown	32 $\pm$ 6	308

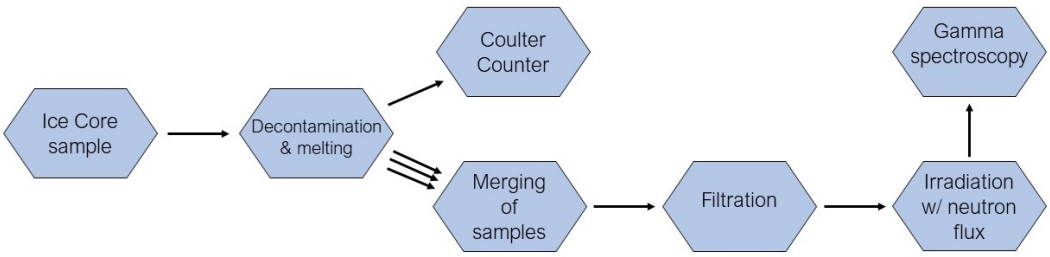

Figure 3.1: Flow scheme of sample preparation for INAA. Ice core samples were decontaminated and melted inside a clean room, and divided into two aliquots. The first aliquot was used for Coulter Counter analysis. The second aliquot was prepared for INAA. At this point several samples were merged together and filtered using a vacuum driven Millipore filtration system. The employed PTFE filters were then stored in precleaned polyethylene vials and brought to the nuclear reactor for irradiation with a neutron flux. Finally, the filters were analyzed through gamma spectroscopy.

3.4.4 Blanks and Detection Limits

Seven blanks were prepared, in order to cover all the preparations made for the RM and the samples. Three blanks (B1, B2 and B3) were prepared using the same filtration methodology as the one used for the samples, but filtering ultrapure water. Additionally, three more blanks (BA1, BA2 and BA3) were specifically prepared for Rabbit irradiations, two being for the liquid reference material and one for the pure Al and Si reference. Finally, two blanks (B6 and B7) where prepared for the multielemental RMs, and were constituted of an empty clean vial. During INAA calculations, both RM and samples were corrected for the corresponding blank.

Detection Limits were calculated using Equation 3.6, following Currie (1968). 3.3 and 3.5 were then applied in order to have the Detection Limit expressed as concentration values.

$$DL = 2.71 + 4.65\sqrt{A_b} \tag{3.6}$$

where:

A_b = integral area of blank sample at the considered gamma energy

Table 3.4 and Figure 3.2 present Detection limits, minimum and median values, all in µg, for the considered elements. A range is presented for detection limits as they were calculated separately for each different batch of irradiation. Differences can be ascribed to longer or shorter periods of time passed between irradiation and measurement of the blank. For each batch of irradiation, sample values were evaluated with respect to the corresponding Detection Limit. Ba, Hg, Ho, Se, Tm and Zn were not considered for the last batch of irradiation, which corresponds to the 4 deeper samples.

Table 3.4: Statistics for Detection Limits and Samples for the Talos Dome ice core in neutron activation analysis. All values reported are in μg.

Element	Detection Limit (μg)	Sample Minimum (μg)	Sample Median (μg)
Al	0.004 - 0.008	1.353	2.551
As	0.000008 - 0.0002	0.0002	0.0004
Ba	0.009 - 0.3	0.01	0.02
Ca	0.04 - 0.5	0.4	0.7
Ce	0.0001 - 0.0002	0.001	0.003
Co	0.000005 - 0.0005	0.0003	0.0006
Cr	0.0002 - 0.0004	0.0007	0.002
Cs	0.000005 - 0.00009	0.0001	0.0002
Eu	0.000004 - 0.00004	0.00003	0.00006
Fe	0.006 - 0.02	1.172	2.185
Hf	0.00001 - 0.0001	0.0002	0.0003
Hg	0.00001 - 0.0001	0.00006	0.0001
Ho	0.0000005 - 0.00001	0.00002	0.00004
K	0.002 - 0.3	0.3	0.7
La	0.00003 - 0.0002	0.0006	0.001
Lu	0.000001 - 0.00001	0.000007	0.00001
Mn	0.0002 - 0.02	0.01	0.02
Na	0.0002 - 0.008	0.2	0.5
Nd	0.0001 - 0.001	0.0004	0.001
Ni	0.0006 - 0.005	0.0006	0.001
Rb	0.0004 - 0.001	0.002	0.003
Sb	0.00001 - 0.00003	0.00002	0.00003
Sc	0.000001 - 0.000006	0.0003	0.0006
Se	0.00001 - 0.00003	0.00003	0.0001
Si	3 - 10	5	10
Sm	0.000001 - 0.000007	0.00007	0.0002
Sr	0.002 - 0.02	0.01	0.02
Ta	0.000002 - 0.00002	0.00008	0.0001
Tb	0.000003 - 0.00003	0.00001	0.00003
Th	0.00002 - 0.0001	0.0002	0.0005
Ti	0.02 - 0.04	0.2	0.3
Tm	0.000001 - 0.000007	0.000004	0.00002
U	0.00003 - 0.0001	0.00006	0.00009
V	0.0001 - 0.0004	0.003	0.004
Yb	0.00001 - 0.0002	0.00008	0.0001
Zn	0.0001 - 0.001	0.002	0.008

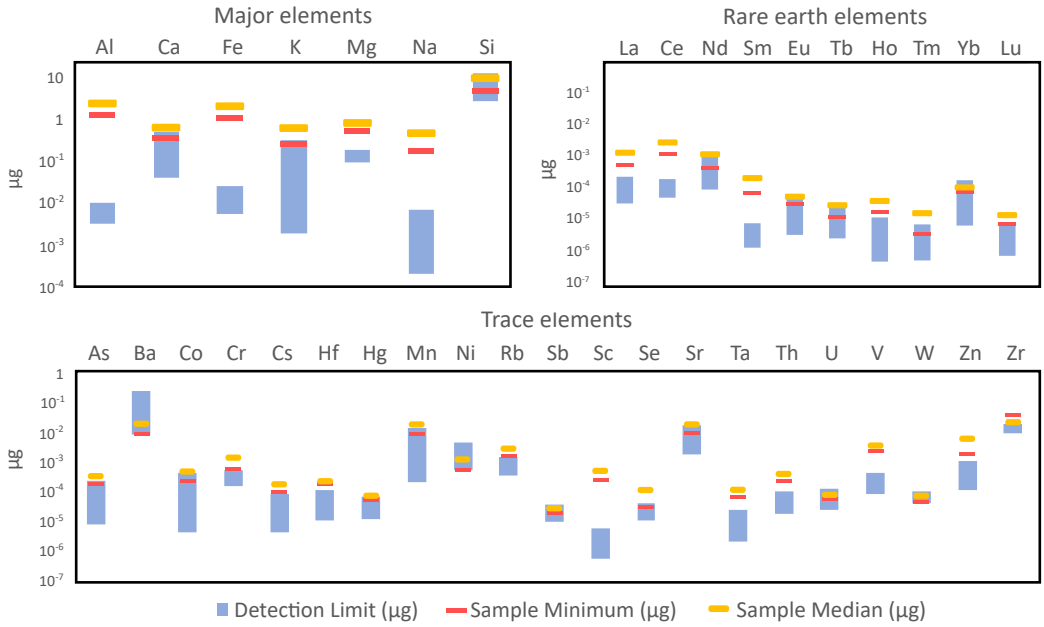

Figure 3.2: Statistical features of INAA measurements: detection limits (blue), minimum (red) and median (yellow) concentrations for all considered elements. y-axis presents µg values on logarithmic scale.

3.5 ICP-SFMS

Inductively Coupled Plasma Sector Field Mass Spectrometry (ICP-SFMS) is an established tool for elemental analysis. Since its first invention in the '80s, it has constantly evolved becoming at present highly automated and easy to operate. This, together with its low detection limits, its applicability to a wide range of different fields of study and the ability to measure the majority of the elements in the periodic table, makes it the forefront of elemental analysis. Since it works with liquid samples, we chose to employ it with INAA, which instead works on solid matrices.

ICP-SFMS employs electronic lenses and a magnetic sector field, which separates ions based on their mass-to-charge ratio, combined with a plasma torch where the sample is atomized. Plasma is generated through the use of argon: high frequency oscillating magnetic and electrical fields are applied at the top of the torch, so that when argon is lit by a spark, electrons can be stripped from argon atoms. This eventually creates a chain reaction which will go on as long as the electrical and magnetic fields are maintained and the gas is supplied. The high temperature of the plasma (6000 - 10000 K) induces the ionizations of atoms which pass through it. The ions are then accelerated and channeled through an interface into the instrument, which is vacuum sealed, where oscillating electrical and magnetic fields are applied: here each ion will have its distinct trajectory and can be recognized and counted by a detector that is installed at the end of this path.

3.5.1 Apparatus

The Byrd Polar Climate and Research Center at Ohio University is equipped with a Thermo Element 2 Inductively Coupled Plasma Sector Field Mass Spectrometer coupled with a microflow nebulizer and a desolvation system (ApexQ, ESI). This setup enhances sensitivity and reduces the interferences due to the formation of oxides by removing water vapor from the sample (Gabrielli et al., 2006).
The stability of the instrument was checked by measuring a solution containing 1 ppb of indium every six samples and variations were never above 15% during daily analysis.
Samples were analyzed in all three available resolution modes (low, medium, high), as reported in Table 3.5.

Table 3.5: Resolution Modes for each analyzed isotope

Resolution Mode	Isotope
Low	^{109}Ag, ^{137}Ba, ^{138}Ba, ^{209}Bi, ^{111}Cd, ^{140}Ce,^{133}Cs, ^{163}Dy, ^{164}Dy, ^{166}Er, ^{167}Er, ^{151}Eu, ^{158}Gd, ^{160}Gd, ^{165}Ho, ^{139}La, ^{7}Li, ^{175}Lu, ^{95}Mo, ^{23}Na, ^{93}Nb, ^{143}Nd, ^{144}Nd, ^{208}Pb , ^{141}Pr,^{85}Rb, ^{121}Sb, ^{147}Sm, ^{152}Sm, ^{120}Sn, ^{86}Sr, ^{181}Ta, ^{159}Tb, ^{205}Tl, ^{169}Tm, ^{238}U, ^{172}Yb, ^{174}Yb
Medium	^{27}Al, ^{59}Co, ^{52}Cr, ^{63}Cu, ^{56}Fe, ^{69}Ga, ^{24}Mg, ^{55}Mn, ^{60}Ni, ^{48}Ti, ^{51}V, ^{64}Zn
High	^{75}As, ^{72}Ge

The choice of the resolution mode for a selected element depends on the potential spectral interferences which may arise. These depend on the presence of atomic or molecular ions with the same mass-to-charge ratio than the element of interest. Elements which lack relevant spectral interferences can therefore be analyzed with low resolution, in order to maximize transmission, while elements which may potentially present interferences have to be determined at higher resolution, reducing the sensitivity and increasing the detection limits.

3.5.2 Calibration solutions

External calibration for each analyzed element was carried out using multielemental standards. All calibration solutions were prepared in a clean room at Byrd Polar Climate and Research Center. For trace analysis, we prepared a set of five calibration solutions of growing concentration, each containing all the trace elements of interest. Trace elements inside each multielemental standard are divided into 4 different groups with different concentrations, based on the potential concentration which can be found in the samples. For rare earth elements (REE) analysis, we prepared two sets. The first one consists of seven solutions of growing concentration, each containing all the REE. The second one consists of four solutions of growing concentration of barium. This was necessary as barium had previously shown potential relevant interferences with REE spectra owing to the formation of barium oxides (Gabrielli et al., 2006). Therefore, calibration curves were checked to see if any corre-

lation between Ba and mass ranges charactered by REE was found in the calibration solution, pointing to the presence of interferences. None were found. Table 3.6 reports details on the elemental concentrations used in the calibration solutions for this study. All calibration curves used for sample analysis had $R^2 > 0.99$.

Table 3.6: Concentration of elements used for each calibration solution in this study

Set of Calibration solutions for REE							
Elements	Concentration values [ppt]						
La, Ce, Pr, Nd, Sm, Eu, Gd, Tb, Dy, Ho, Er, Tm, Yb, Lu	0.0004	0.02	0.1	1.2	5.6	22.5	113.5

Set of Calibration solutions for Ba			
Elements	Concentration values [ppt]		
Ba	3.3	37.7	193	1205

Set of Multielemental Calibration solutions					
Elements	Concentration values [ppt]				
Al, Fe, Mg, Na, Ti	11.1	136	698	1415	2804
Ba, Co, Cr, Cu, Ga, Li, Mn, Nb, Ni, Pb, Rb, Sr, V, Zn	1.11	13.6	69.8	141.5	280.4
As, Cs, Ge, Mo, Sn, Ta, U	0.11	1.36	6.98	14.15	28.04
Ag, Bi, Cd, In, Sb, Tl	0.01	0.14	0.70	1.42	2.80

3.5.3 Sample preparation and leaching procedure

Twenty-three samples spanning the entire ice core were selected for ICP-SFMS analysis, as reported in Table 3.7.

Preparation of the samples was carried out in a class 1000 clean room at University of Milano-Bicocca. All the containers used to store, even temporarily, the samples had been subjected to two weeks acid bath (HNO_3 5%) prior to use. Samples were decontaminated and melted following the same procedure as the INAA samples. Samples were then divided into tree aliquots. The first one was used for Coulter Counters analysis. The second aliquot was filtered using a Nalgene filtration system (0.2 µm cut off). This filtration system gives the possibility to change the holder and the receiver for each sample, thus diminishing the possibility for cross-contamination between the samples. This was not the case for the Millipore filtration system that was used for the preparation of the INAA samples. The filtrate was transferred to polypropylene (PP) centrifuge tubes. The third aliquot was transferred in the PP centrifuge tubes without further treatment. Figure 3.3 reports a flow scheme for ICP-SFMS sample preparation.

Table 3.7: Samples prepared for ICP-SFMS analysis

Sample	Depth (m)	Age (kyr B.P.)	Dust Concentration (ng/g)
TD-0209	209	2.3	31 ± 6
TD-0262	262	3.1	32 ± 1
TD-0383	383	5.2	48 ± 3
TD-0398	398	5.6	21 ± 1
TD-0438	438	6.3	40 ± 3
TD-0849	849	19.5	480 ± 32
TD-0893 *	893	23.9	156 ± 5
TD-0950	949	29.8	232 ± 52
TD-1030	1030	37.1	240 ± 5
TD-1186	1186	49.8	160 ± 3
TD-1249	1249	58.4	95 ± 5
TD-1269	1269	61.6	255 ± 7
TD-1303	1303	72.2	80 ± 6
TD-1313	1312	76	106 ± 9
TD-1391	1390	118.9	34 ± 3
TD-1397	1396	122.5	45 ± 10
TD-1492	1492	unknown	142 ± 22
TD-1496 *	1496	unknown	86 ± 8
TD-1524 *	1524	unknown	83 ± 4
TD-1544	1544	unknown	94 ± 6
TD-1558	1558	unknown	204 ± 62
TD-1571	1571	unknown	112 ± 21
TD-1616	1616	unknown	64 ± 3

* not filtered due to small volume

All samples (untreated and filtered) were acidified with ultrapure HNO_3 at 1% v/v for the leaching procedure. The effectiveness of leaching is highly dependent on leaching time, on the element and on the mineral in which the element is enclosed (Koffman et al., 2014a; Rhodes et al., 2011; Uglietti et al., 2014). It is also difficult to quantify how much of the inconsistencies are actually due to incomplete leaching and how much to partial atomization of the single mineral particle in the plasma. Thus, all results obtained with this procedure have to be considered approximated to a certain degree.

Nonetheless, leaching remains the best choice for ICP-SFMS analysis of Antarctic ice samples since the alternate procedure, full digestion, has a much higher contamination risk. Moreover, the majority of aeolian dust in Antarctic samples is composed of very small particles (modal value for Talos Dome is around 2 µm), which typically suffer less from leaching and atomization problems. To reach allowable recovery rates, samples have to be leached for at least one month (Koffman et al., 2014a; Uglietti et al., 2014). Our samples were allowed to leach for six weeks before analysis. Al and Fe has been shown to be among the most difficult elements to leach (Grotti et al., 2011). In our case, during analysis, we noticed very high standard deviations during the acquisition of the aluminum spectrum. We therefore chose to not consider Al measurements for our study.

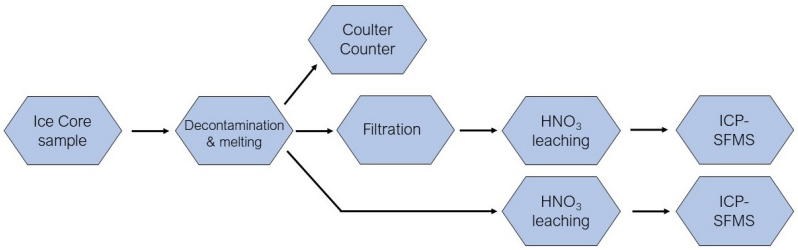

Figure 3.3: Flow scheme of sample preparation for ICP-SFMS. Ice core samples were decontaminated and melted inside a clean room, and divided into three aliquots. The first aliquot was used for Coulter Counter analysis. The second aliquot was filtered using a Nalgene filtration system. The filtrate and the third aliquot were subsequently treated with HNO_3 and allowed to leach for 6 weeks before ICP-SFMS analysis.

3.5.4 Blanks and Detection Limits

We prepared two instrumental blanks (B1 and B2) and four procedural blanks, all with ultrapure water. The instrumental blanks simply consist of ultrapure water with 1% v/v HNO_3. Of the procedural blanks, two were frozen blanks (B3 and B4) which were melted and decontaminated following the same procedure as the samples, and two were filtered blanks (BF1 and BF2) which were subjected to the same filtration procedure as the samples.

Detection Limits were calculated by measuring ten times an instrumental blank, and then considering 3 times the standard deviation of this measurement. For some elements, namely U, Cu, Pr, Er, Ho, Dy, one of the ten measurements had to be discarded due to anomalously high values. Table 3.8 lists detection limits and measured blanks for all the elements considered in

this work.

Table 3.8: Detection limits and measured blanks. For each type of blank, the mean and standard deviation are reported.

			Untreated sample			Filtered sample		
Isotope	LOD	Instrumental blank	Procedural blank	Min.	Median	Procedural blank	Min.	Median
	(pg/g)	$\mu \pm \sigma$ (pg/g)	$\mu \pm \sigma$ (pg/g)	(pg/g)	(pg/g)	$\mu \pm \sigma$ (pg/g)	(pg/g)	(pg/g)
Ag	0.08	0.94 ± 0.02	1.1 ± 0.1	0.44	0.54	0.97 ± 0.02	0.45	0.55
As	0.42	0.6 ± 0.1	3 ± 2	1.22	2.94	0.58 ± 0.03	0.55	1.08
Ba	29.04	149 ± 127	45 ± 21	33.54	85.63	105 ± 68	30.02	29.04
Bi	0.01	0.07 ± 0.01	0.06 ± 0.01	0.08	0.22	0.20 ± 0.04	0.06	0.17
Cd	0.058	0.8 ± 0.7	3.6 ± 0.5	5.34	20.20	3 ± 1	0.36	1.99
Ce	0.153	0.17 ± 0.01	0.27 ± 0.03	1.44	23.17	1.1 ± 0.8	0.30	0.89
Co	0.2	1.37 ± 0.06	1.39 ± 0.02	0.91	3.12	1.6 ± 0.2	0.55	1.05
Cr	15	35 ± 11	35 ± 5	22.44	36.79	78 ± 49	31.33	62.87
Cs	0.77	1.9 ± 0.3	2.3 ± 0.2	1.17	1.88	2.0 ± 0.4	0.79	1.24
Cu	0.79	6 ± 1	6.65 ± 0.45	8.36	22.29	12 ± 2	7.35	21.81
Dy	0.020	0.04 ± 0.01	0.024 ± 0.002	0.11	1.22	0.08 ± 0.05	0.02	0.06
Er	0.012	0.015 ± 0.002	0.019 ± 0.006	0.07	0.64	0.05 ± 0.02	0.02	0.04
Eu	0.050	0.112 ± 0.000	0.104 ± 0.007	0.12	0.64	0.11 ± 0.01	0.08	0.10
Fe	1036	1575 ± 435	1717 ± 96	1056.13	6315.16	1596 ± 238	1445.74	1036.00
Ga	0.67	5 ± 1	4.41 ± 0.19	2.11	4.81	7 ± 1	1.08	2.20
Gd	0.026	0.095 ± 0.007	0.110 ± 0.005	0.13	1.77	0.13 ± 0.04	0.06	0.11
Ge	2.88	4 ± 1	3.35 ± 0	3.01	2.88	3.6 ± 0.2	3.01	2.88
Ho	0.002	0.003 ± 0.001	0.003 ± 0.001	0.02	0.24	0.022 ± 0.001	0.003	0.01
La	0.066	0.2 ± 0.1	0.4 ± 0.1	0.97	12.18	0.8 ± 0.5	0.17	0.51
Li	30	263 ± 13	268 ± 5	144.98	187.29	265 ± 12	143.51	172.60
Lu	0.005	0.006 ± 0.001	0.005 ± 0.001	0.01	0.08	0.009 ± 0.004	0.01	0.01
Mg	233.90	676 ± 1	731 ± 125	2340.37	6362.23	1322 ± 91	1253.94	1870.79
Mn	13.33	21 ± 8	19 ± 1	18.86	160.89	19 ± 4	14.93	22.64
Mo	0.21	0.6 ± 0.2	0.50 ± 0.03	0.58	1.34	2 ± 1	1.07	2.34
Na	777	3215 ± 452	2953 ± 171	17848.10	40992.28	17597 ± 12962	16449.87	44723.47
Nb	0.48	0.9 ± 0.3	0.55 ± 0.04	0.50	2.18	2 ± 1	0.56	0.48
Nd	0.056	0.073 ± 0.02	0.12 ± 0.02	0.65	10.23	0.3 ± 0.2	0.10	0.33
Ni	28	359 ± 23	342 ± 3	156.47	201.36	348 ± 15	154.36	191.81
Pb	0.14	0.7 ± 0.1	2 ± 1	1.95	7.45	2 ± 1	0.95	1.82
Pr	0.015	0.031 ± 0.006	0.029 ± 0.001	0.17	2.93	0.09 ± 0.06	0.03	0.09
Rb	5	24.1 ± 0.4	29 ± 6	22.92	38.92	23.85 ± 0.01	15.82	24.08
Sb	0.37	0.24 ± 0.05	0.17 ± 0.03	0.39	0.37	0.9 ± 0.6	0.39	0.65
Sm	0.065	0.214 ± 0.001	0.27 ± 0.01	0.30	2.44	0.29 ± 0.06	0.19	0.28
Sn	0.20	3.15 ± 0.06	3.1 ± 0.1	2.09	2.99	4.5 ± 0.3	2.58	3.53
Sr	5.59	85.7 ± 0.3	91 ± 2	70.14	145.72	126 ± 36	38.53	61.38
Ta	0.201	0.27 ± 0.06	0.18 ± 0.01	0.21	0.22	0.27 ± 0.01	0.20	0.21
Tb	0.006	0.0119 ± 0.0001	0.012 ± 0.000	0.02	0.25	0.02 ± 0.01	0.01	0.02
Ti	97	152 ± 36	97 ± 25	109.29	502.17	141 ± 37	99.76	126.92
Tl	0.072	0.08 ± 0.02	0.05 ± 0.02	0.10	0.24	0.07 ± 0.02	0.08	0.07
Tm	0.004	0.008 ± 0.001	0.008 ± 0.001	0.01	0.09	0.012 ± 0.004	0.01	0.01
U	0.16	0.06 ± 0.02	0.10 ± 0.06	0.10	0.16	0.14 ± 0.04	0.04	0.36
V	3.95	9 ± 1	6 ± 1	5.58	14.01	6 ± 2	4.08	3.95
Yb	0.027	0.037 ± 0.003	0.044 ± 0.001	0.06	0.60	0.06 ± 0.02	0.03	0.04
Zn	3	990 ± 900	709 ± 50	164.40	837.91	1487 ± 925	408.05	997.68

Elements with blank values too much high with respect to the minimum and median values of the sample data set were discarded; namely Ba, Cr, Ge, Sb, U, Zn. Similarly we discarded Nb, Nd and Mo values for the filtered samples.

Chapter 4

Results and Discussion

4.1 Talos Dome dust record

Here we expand the published dust profile (Delmonte et al., 2010b; Albani et al., 2012) for the Talos Dome ice core in the deep section. We analyzed 125 samples from 1450 m to the bottom, integrating the profile which in this section previously counted only 80 samples. The dust record for the deep part can be seen in Figure 4.1, while the complete dust record is shown in Figure 4.2 together with the $\delta^{18}O$ record (from Stenni et al. (2011) and two dust size indexes (FPP and CLPP) which will be discussed later. The $\delta^{18}O$ record stops before 1500 m, since beneath this depth dating is still uncertain as the isotopic signal may be disturbed.

The dust concentration in the Talos Dome ice core exhibits the well known correlation with the oxygen isotopic ratio, and thus temperature (Lambert et al., 2008; Delmonte et al., 2010b). Levels drop during the Holocene and the earlier interglacial (MIS5) and rise during the last glacial stage (MIS2). South America, and Patagonia in particular, has been recognized as the major dust supplier for Eastern Antarctica during glacial stages (Grousset et al., 1992; Basile et al., 1997; Lambert et al., 2008; Delmonte et al., 2008; Vallelonga et al., 2010; Delmonte et al., 2017). It seems that during interglacials other sources become more relevant. When the hemispheric dust influx from remote sources is dampened, local sources become more important to the total dust budget at Talos Dome. This is highlighted by higher concentrations of larger particles (Albani et al., 2012; Aarons et al., 2016) and by geochemical evidences (Baccolo et al., 2018b).

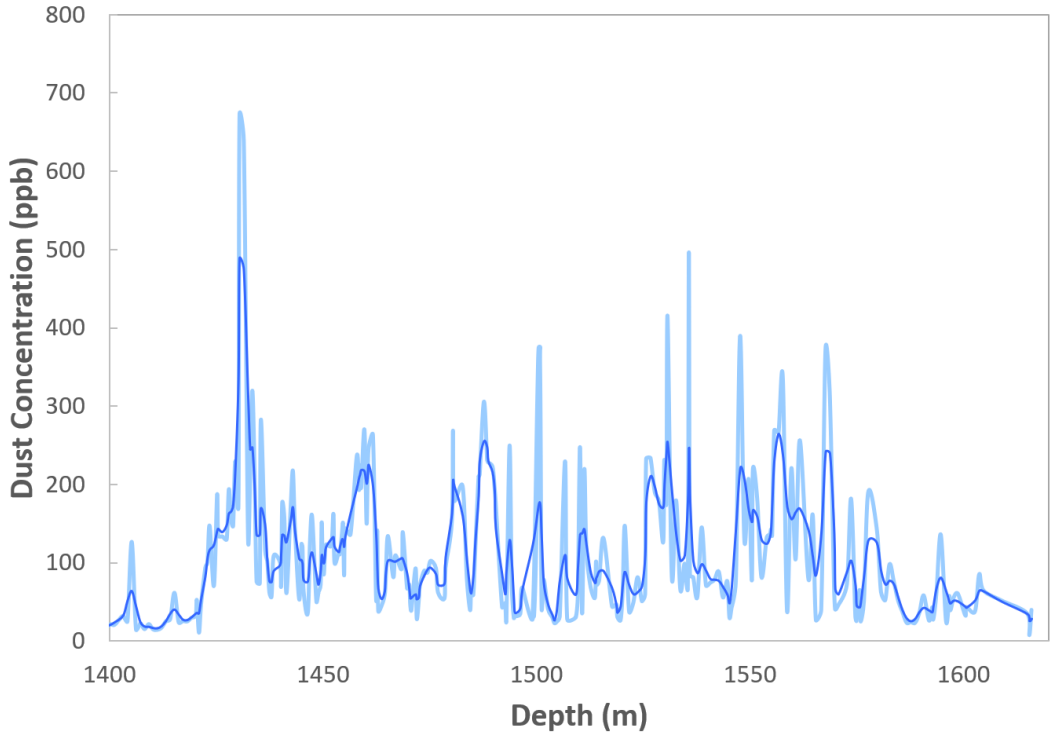

Figure 4.1: Dust profile for the deep part of the Talos Dome ice core, from 1400 m of depth to the bottom. In light blue the raw dust concentration in ppb, in dark blue the same data smoothed using a gaussian filter with a window size of 5.

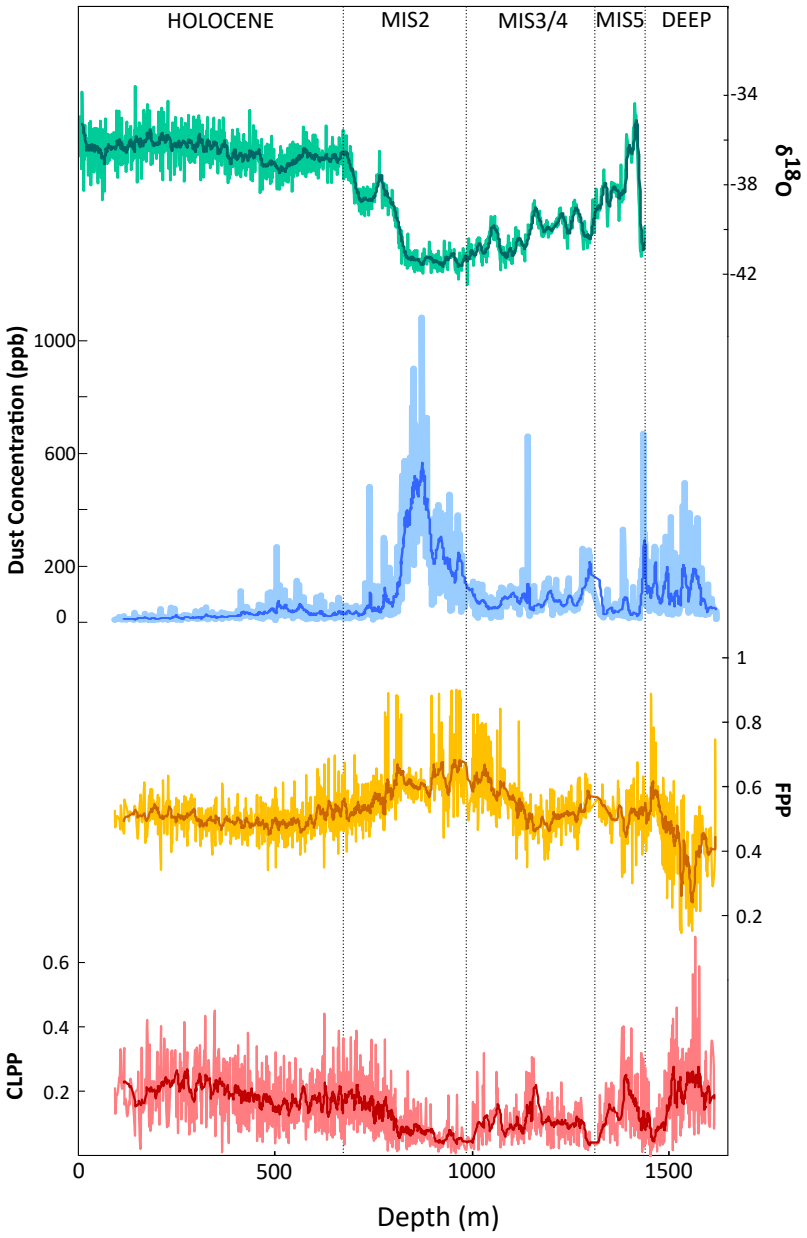

Figure 4.2: Features of the Talos Dome ice core. Four records are presented, each one with a lighter color indicating data points and a darker color showing the 10-point moving average, which highlights significative patterns. All data are plotted with respect to sample depth, expressed in meters, on the x-axis. Dotted vertical lines underline different climatic periods, using the Marine Isotope Stage (MIS) timescale (Railsback et al., 2015). At the top, in green, we present the $\delta^{18}O$ record (from Stenni et al. (2011)). Underneath, in blue, we show the total dust concentration, expressed in parts per billion (ppb). The last two records show the fine particle percentage (FPP) in yellow and the coarse local particle percentage (CLPP) in red (Delmonte et al., 2004; Baccolo et al., 2018b). FPP is defined as the ratio between fine particles (0.6-2 µm) and 0.6-5 µm ones, while CLPP represents the ratio between coarse particles (5-10 µm) and the total dust (0.6-10 µm).

Two indexes were calculated to assess the relative contribution of fine and coarse particles respectively: FPP (Fine Particle Percentage) and CLPP (Coarse Local Particle Percentage) (Delmonte et al., 2004; Baccolo et al., 2018b), as seen in Figure 4.2. These are calculated following Equations 4.1.

$$FPP = \frac{0.6 - 2}{0.6 - 5} \qquad CLPP = \frac{5 - 10}{0.6 - 10} \tag{4.1}$$

where:

$0.6 - 2$ = dust concentration between 0.6 and 2 µm
$0.6 - 5$ = dust concentration between 0.6 and 5 µm
$0.6 - 10$ = dust concentration between 0.6 and 10 µm
$5 - 10$ = dust concentration between 5 and 10 µm

Both indexes display a correlation with climatic stages. FPP is higher during the last glacial stage, in accordance with the remote source of dust transported to Antarctica during this period. In fact the longer the atmospheric transport, the smaller the diameter of dust particles, since the coarse ones are progressively removed due to gravitational settling. Thus, the coarser fraction is less represented with respect to the total dust flux during the last glacial stage, translating in a lower CLPP. As Talos Dome is located near ice-free zones, the site receives a constant dust flux from local sources (Baccolo et al., 2018b). This is characterized by coarser particles with respect to distant sources, as the transport is much more limited. This is evident if we compare the Talos Dome dust record with inner sites, such as Vostok or Dome C (Delmonte et al., 2004, 2010b).

4.1.1 Granulometric anomalies

Figure 4.2 highlights some anomalies in the deeper part of the Talos Dome dust record; in particular the FPP drops to very low values, while CLPP shows a significant increase. We interpret this as a sign of dust aggregation, as was previously observed in the EPICA Dome C ice core (De Angelis et al., 2013). Dust particles originally present in the ice, as a result of the high pressure that characterizes deep ice and of ice metamorphism, are pushed towards crystal boundaries and bound together. This mechanism leads to a post-depositional artefact consisting in an increase of coarser grain size in the dust record which is uncorrelated to dust sources and transport. This post-depositional effect can be observed exclusively from the analysis of dust grain size spectra, while it cannot be appreciated from the concentration data only.

In the TALDICE core, 98% of samples from surface to 1450 m depth show modal values around 2 µm for the volume size distribution. For comparison, samples from the deep section, show in 25% of cases a mode between 2 and 4 µm. Examples are shown in Figure 4.3.

Various sonication tests were made to break the aggregates into its original constituents, but the methodology overall was not successful. In total 79 samples were sonicated, with varying

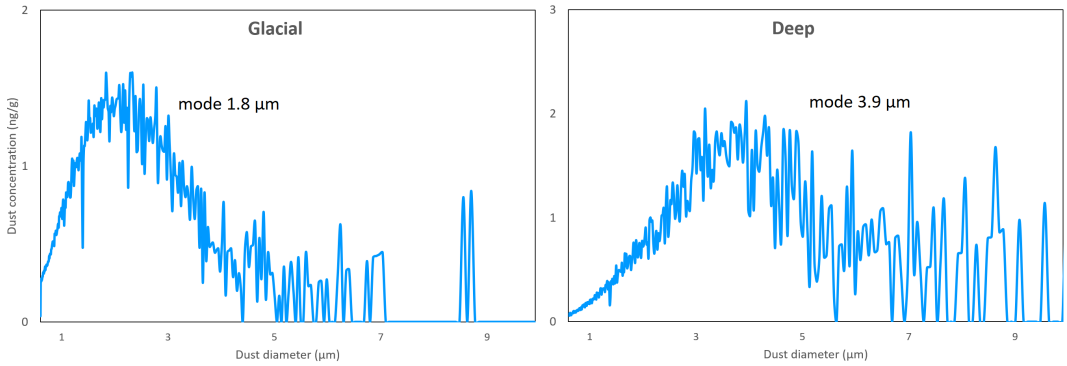

Figure 4.3: Example of grain size distribution in a glacial (left) and deep (right) sample. We show diameter values between 0.6 and 10 µm plotted against dust concentration (ng/g). The mode for both samples has been calculated: 1.8 µm for the glacial sample and 3.9 µm for the deep sample, showing a net increase in the latter distribution.

time intervals between 3 and 15 minutes. 47% of the sonicated samples displayed an increase of the total volume of particles, pointing to possible contamination, while 32% showed a decrease and only 21% showed no variation. No correlation with sonication time was found. Looking at grain size distribution, if sonication was successful, we would expect to find an increase in fine particles and a decrease in coarse particles. Considering the 0.6 - 10 µm range, 28% of samples showed an increase across all grain size categories, and 10% showed a decrease in all categories. Only 22% of total samples showed the expected decrease of coarse dust aggregates and an increase of particles below 5 µm. These numbers clearly demonstrate that sonication is not a reliable method of study for deep ice particle aggregates.

We interpret these results in the following way:

- Microparticle increase in all grain size channels reflect a possible contamination of the samples during the sonication procedure, possibly related to the containers used, including their lids. Lids and caps typically release much more particles during sonication than the container itself. This means that the sample has either to be maintained in an upward position inside the sonicator, or the container has to be changed. Further study is needed in this respect, as even blank samples with the same sonication parameters (type of container, position of container, time of sonication and period since water inside the sonic bath was changed) sometimes displayed contamination and sometimes did not. In any case, we conclude that an increase in dust concentration spread throughout all the dust spectrum is related to contamination.

- Change in the size spectra towards smaller particles after sonication may actually reflect the presence of uncemented aggregates, as those found in the EPICA Dome C ice core below 2800 m depth.

- No change in the dust grain size spectra and persistence of large dust particles reflects the presence of cemented aggregates formed into the ice and difficult or impossible to break. This is further sustained by our observations at SEM (see Section 4.2) where we found

evidence for a newly-formed mineral into the deep ice, deriving from chemical alteration of dust grains, and acting as a cementing agent for the residual partly-weathered or unweathered particles.

4.2 Jarosite formation

During our observations at SEM, we analyzed single dust particles deposited on a polycarbonate filter. On these samples we also performed EDS to assess the composition of the particles. While the upper part of the core typically displays micrometric particles and volcanic glasses, the deeper part showed grains characterized by evident weathering features (Figure 4.4).

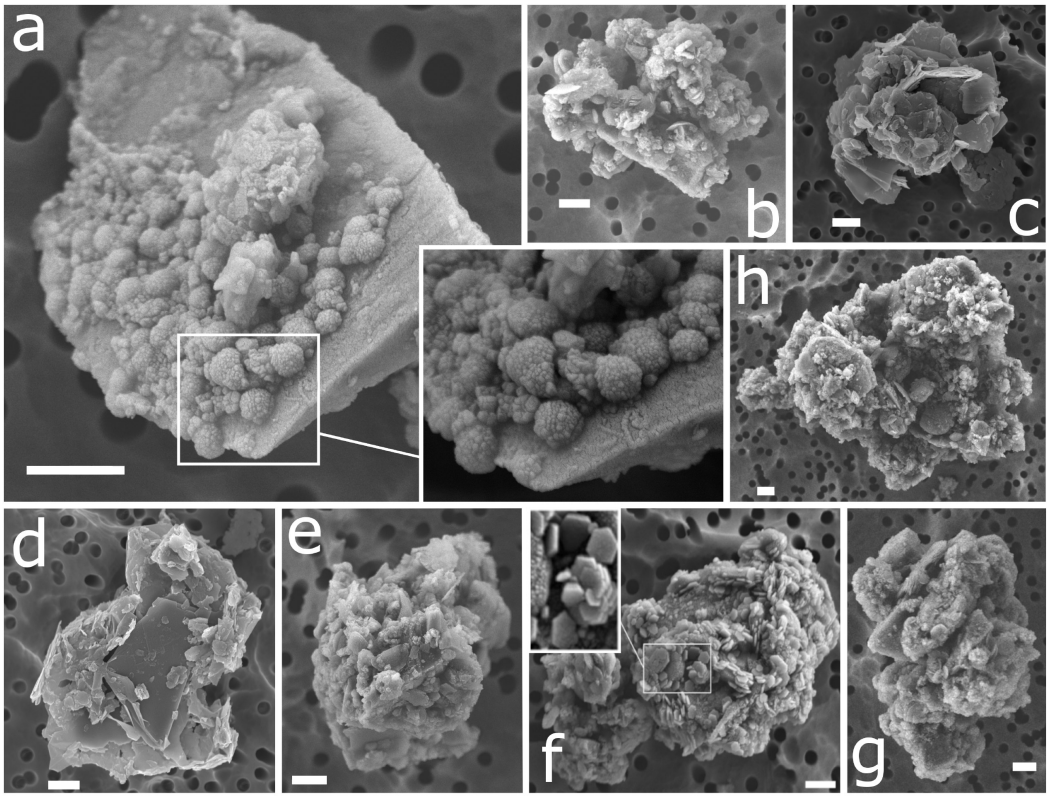

Figure 4.4: SEM images of dust grains from deep samples (>1450 m) of the Talos Dome ice core. The scale bar is 1 µm.

We found precipitates ranging from globular shapes (Figure 4.4a) to layered plates (Figure 4.4b) and hexagonal crystals (Figure 4.4f). A few volcanic glasses, covered by precipitates (Figure 4.4a) or aggregated together (Figure 4.4c,d) are recognized. Poorly ordered aggregates of relatively big dimensions were also spotted (Figure 4.4e,g,h). Elemental maps of individual grains show the different composition between particles from the deep part and other sections of the ice core. Typically, precipitates that are present in the deep part are composed by Fe, S and K, which is compatible with the chemical formula of jarosite [$KFe_3(SO_4)_2(OH)_6$], while the "residual" cores of the grains mostly consist in Si or a mixture of Si and Al (see Figure 4.5).

Jarosite is a ferric-potassium hydroxide sulphate mineral which typically forms as a result of chemical weathering in environments which are acidic, rich in iron and with limited presence of liquid water (Papike et al., 2006). Moreover, it is known that the acidic weathering of basalt

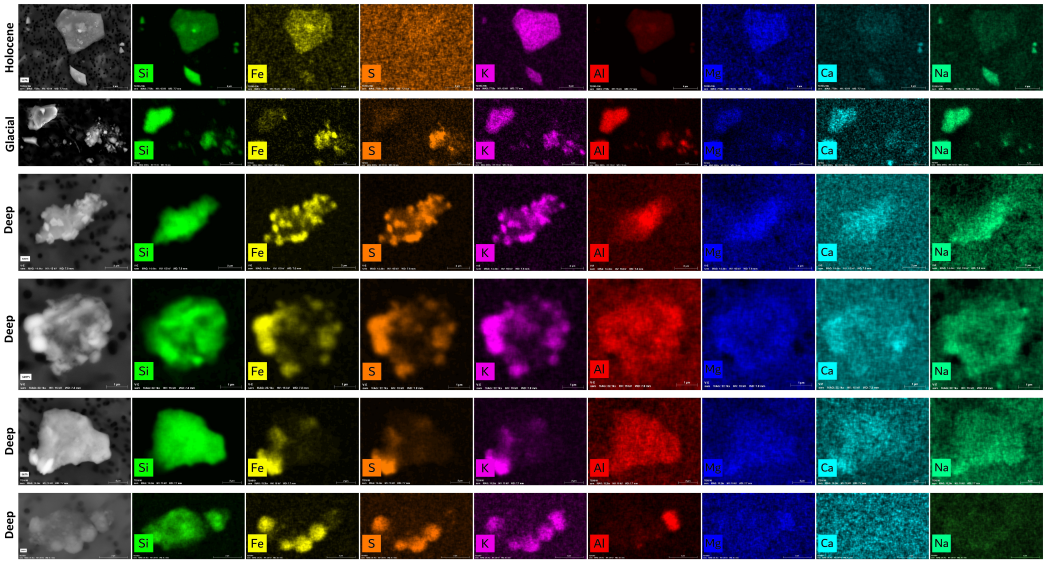

Figure 4.5: Elemental maps of individual grains obtained with SEM-EDS analysis. Starting from the top row, we show: a Holocene sample, a glacial sample and four deep samples. For each sample, from left to right, the SEM image and the elemental concentrations of Si, Fe, S, K, Al, Mg, Ca and Na are presented.

in a closed system produces jarosite and amorphous silica (Madden et al., 2004; Zolotov and Mironenko, 2007). This matches the observed composition of the grains observed in our deep samples. Since its discovery on Mars soil by the Opportunity Rover, jarosite has been a mineral of great interest because of its connection to water-related weathering on Mars. Jarosite is also known to act as a cement during weathering (Long et al., 1992): this would explain the difficulty in breaking the aggregates experienced with the ultrasonic bath.

The distribution of other elements further supports chemical weathering in the deep section of the ice core: Mg, Ca and Na are almost absent from jarosite precipitates and scarce within Si-rich grains. This confirms what had already been observed in a previous elemental characterization of TALDICE mineral dust (Baccolo et al., 2018a). It is possible that the acidic environment of deep ice favors chemical reaction of these elements which lead to the formation of soluble compounds. These findings led to the publication of Baccolo et al. (2021).

4.3 Elemental composition

We further investigated the elemental composition of dust in the Talos Dome ice core with INAA and ICP-SFMS measurements. Raw concentration values are reported in Appendix A. We consider INAA results to reflect the composition of the insoluble fraction of dust,

while filtered ICP-SFMS samples should reflect the soluble fraction, and untreated ICP-SFMS samples are considered as a benchmark for the total dissolvable concentration. We note that the total dissolvable concentration actually represents the fraction which can both be dissolved in acid and atomized in plasma. We will consider separately the data from the three different methodologies by looking at correlation matrices and enrichment factors (EFs) for each dataset.

The correlation matrices were calculated by using the Pearson correlation coefficient (r), which is expressed by dividing the covariance of the considered variables by the product of their standard deviations. This coefficient varies between -1 and +1, where -1 represents a perfect negative correlation; 0 represents no correlation at all; +1 represents a perfect positive correlation.

The enrichment factor was calculated with respect to the average concentration of the upper continental crust, following Equation 4.2 and using Wedepohl (1995) for elemental crustal values.

$$EF = \frac{Element_{ice}/Ce_{ice}}{Element_{crust}/Ce_{crust}} \tag{4.2}$$

The reference element is chosen as to be an element with low geochemical reactivity and mobility; in this way an EF close to 1 tells us that the considered element in our sample is prevalently of crustal origin, while higher numbers testify to an enrichment of the element. We chose cerium as the reference element, since it was measured both with INAA and ICP-SFMS. This will allow us to compare EFs calculated for the same element measured with the two different techniques.

As indicated in literature (Gabrielli et al., 2005a), we chose a threshold of 10 to discriminate between enriched and non enriched elements and in the figures we divided samples in three different color-coded categories:

- Interglacial samples, with Holocene samples indicated in red shading and MIS5 samples in yellow;
- Glacial samples, which cover MIS2 to MIS4, in blue shading;
- Deep samples,from 1450 m of depth to the bottom of the ice core, in green shading.

4.3.1 Insoluble fraction

Below we show a graphical representation of the correlation matrix of INAA data for major and trace elements (Figure 4.6), and for rare-earth elements (Figure 4.7).

Al, As, Ba, Co, Cs, Fe, K, Mn, Na, Sc, Si, Sr, Ti, V all show a high degree of correlation between each other, with values always above 0.7 (two exceptions are Ba-Si and V-Si, both with r = 0.67). Among these, Al, Fe, Ti, Mn, Co and V show very high correlation with r values always above 0.85. Rb and Zn also display a good correlation with this group of elements. This indicates a common source for these elements, which we expect to be mainly of crustal origin. On the other hand, Cr is the element that shows the least amount of correlation with

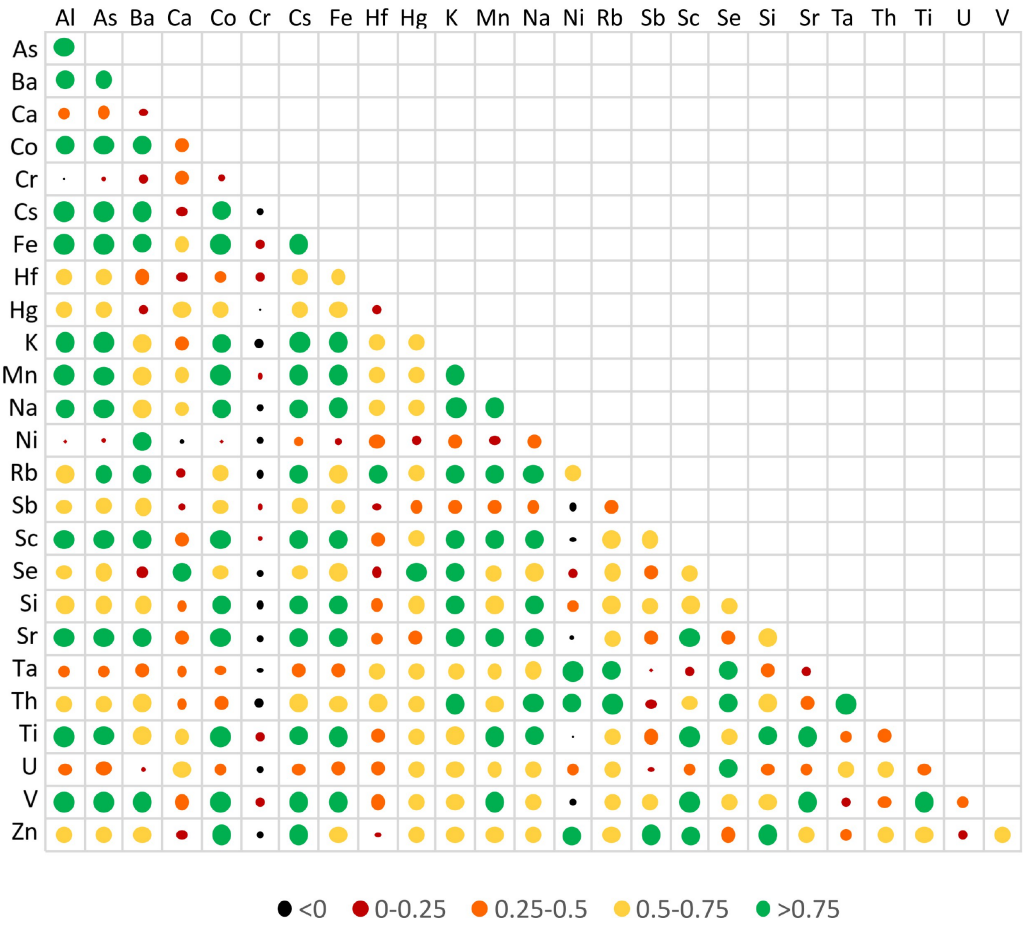

Figure 4.6: Graphical representation of the correlation matrix for INAA data for major and trace elements. Both color (see legend) and dimension of the dots represent the degree of correlation. The bigger the dot, the closer the number is to 1.

other elements. Ca, Se and Hg appear to be correlated to one another, pointing to a probable common source, as will be explained while discussing EFs.

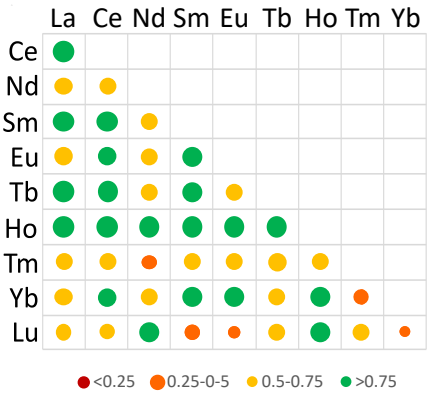

Figure 4.7: Graphical representation of the correlation matrix for INAA data for Rare Earth Elements. Both color (see legend) and dimension of the dots represent the degree of correlation. The bigger the dot, the closer the number is to 1.

Looking at REEs, correlation is very high ($r > 0.9$) only for Ce, Ho, La, Sm and Tb. An anomaly is represented by Lu, Nd, Tm and in minor part Yb, which do not show a good correlation with other REEs. This could be due to analytical problems as these elements had detection limits similar to the minimum concentrations found in the samples.
No element showed any correlation with depth.

Figure 4.8 shows the enrichment factors calculated for INAA measurements. Most of the elements show values close to 1, which confirm the prevalent crustal origin of the mineral dust. This is not unexpected since INAA focused on the insoluble fraction of the impurities present in the Talos Dome ice core which mostly consist in mineral particles. Hg and Se are the elements in the insoluble fraction with the highest EFs throughout the entire length of the ice core, with values always above 10. Both these elements are volatile species which are typically oxidized and partitioned to the particulate phase before being deposited (Mosher and Duce, 1987; Wen and Carignan, 2007; Jitaru et al., 2009). These elements also showed a general weak correlation with other elements except with each other (r=0.82) and Ca, pointing to a common source. These elements have been shown to derive prevalently from emissions from the marine biosphere, with minor contributions from volcanic activity and sea salt sprays (Nriagu, 1989; Schroeder and Munthe, 1998; Wen and Carignan, 2007). Additionally, the biogeochemical cycle of mercury in polar regions is affected by the seasonal absence of photochemical reactions, leading to accumulation of Hg on snow and ice (Ebinghaus et al., 2002). The observed enrichment could thus be related to the volatile elements partitioning to the solid phase and bounding with mineral dust particles, as reported by Jitaru et al. (2009).

As, Sb, Zn and Cr have lower EF if we consider mean values, but single samples may display values higher than 10 in all the three categories. These elements, while having a higher crustal contribution than Se and Hg (Nriagu, 1989), also have significant sources from sea salt aerosols, biogenic sources and volcanic emissions.

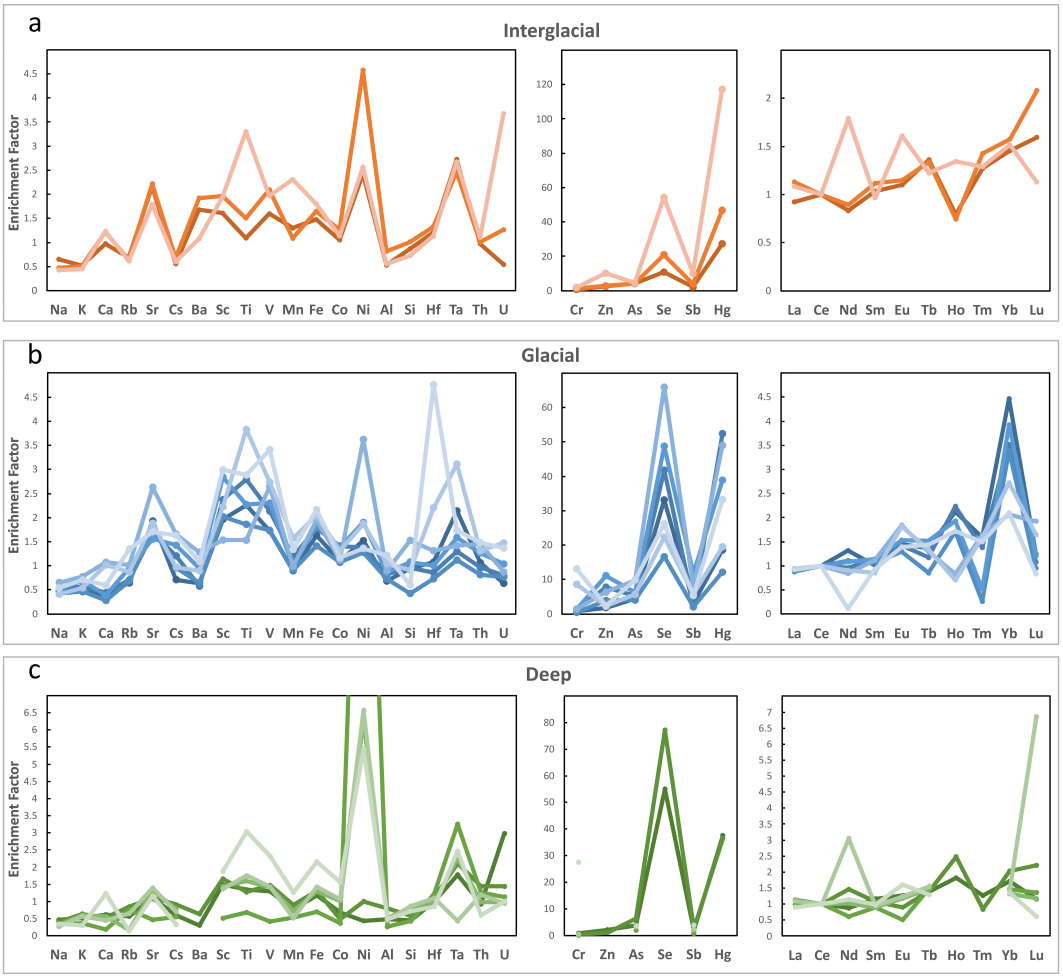

Figure 4.8: Enrichment Factors calculated for INAA measurements. Samples were divided into 3 categories: interglacial samples (a), glacial samples (b) and deep samples (c). Each line represents a single sample. For deep samples, some elements (Ba, Zn, Se, Hg, Ho, Tm) were not considered in all the samples, leading to some broken lines.

Nickel displays a different behavior throughout the different categories: in glacial and inter-glacial samples EF values are quite low, with means respectively of 3.2 and 1.8 and single values always under 5, while in the deep core we find several samples above 5 and a single value of 19.2. Nickel concentrations can be strongly influenced by volcanic activity, which is abundant at Talos Dome and may be the origin of single high values. Further studies will be needed to better understand the enrichment of nickel in deep samples.

Between the elements which do not display an enrichment trend, titanium is the element with the highest variability in all three categories, together with tantalum; hafnium shows great variability only in glacial samples. Ti, Hf and Ta can be enriched in atmospheric mineral dust as a consequence of weathering processes occurring during the atmospheric transport (Vlastelic et al., 2015; Baccolo et al., 2016b). In addition, we note that all these elements are highly fractionated in heavy minerals, thus the presence of a few heavy mineral grains could lead to a high variability in terms of elemental concentration.

Rare earth elements in general do not display enrichment tendencies. It is interesting to look at ytterbium, which consistently displays higher values only in glacial samples.

4.3.2 Total dissolvable fraction

Figures 4.9 and 4.10 report a graphical representation of the correlation matrix for the total dissolvable fraction, respectively for major and trace elements, and for REEs.
Co, Fe, Mn, Ti and V display a very good correlation between each other, with values always above 0.7. This is in line with what was observed for the insoluble fraction.

Mo and Nb also have a very high degree of correlation between each other (r=0.95) and with both Ta and Sn (r=0.83-0.88). Nb and Ta usually occur together in minerals due to their chemical similarities, such that their most widespread mineral is known either as columbite or tantalite depending on the predominating element. Mg and Na only seem to show a high correlation with each other, pointing to a strong influence of sea salt emissions, of which both elements are major components, to their total concentration.

On the other hand, Cd, Cu, Li and Ni do not display any correlation with the other elements suggesting a heterogeneity of sources.

REEs have a very high degree of correlation between each other, with r values always between 0.98 and 1, except for Eu which displays values between 0.8 and 0.9. This is indicative of the various degrees of the well-known Eu anomaly.

Enrichment factors were also calculated for this dataset, as shown in Figures 4.11 and 4.12. Ti, V, Mn, Fe, Co and Nb consistently show low values in all samples, in line with what was observed before. Mg, Rb, Sr, Cs, Ta, Ga, Pb and Tl, while always remaining under the chosen threshold of 10 for enrichment values, display a higher inter-sample variability. This confirms the main crustal origin of this group of elements, with possible minor influences from sea salts, especially for Mg and Sr. It is clear that Cd appears to be greatly enriched in all samples, with values ranging several orders of magnitude. We interpret this as a background

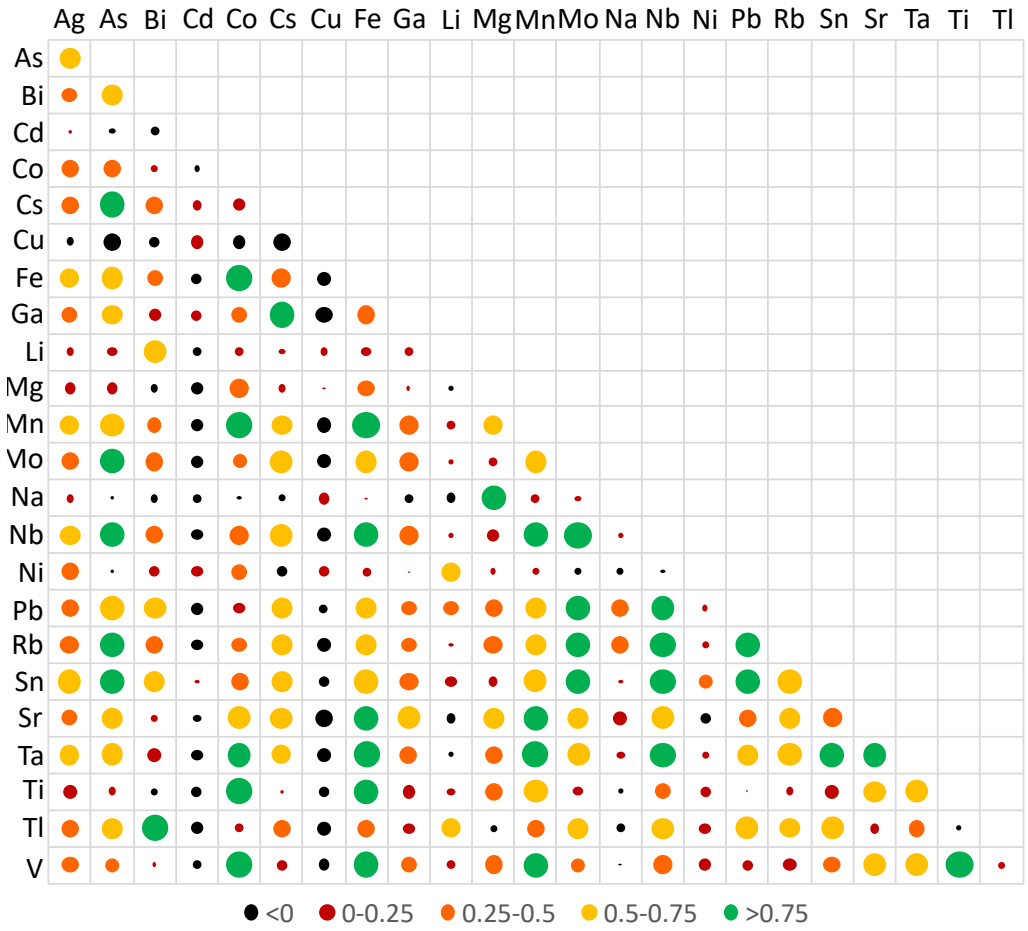

Figure 4.9: Graphical representation of the correlation matrix for ICPM-SFMS untreated data for major and trace elements. Both color (see legend) and dimension of the dots represent the degree of correlation. The bigger the dot, the closer the number is to 1.

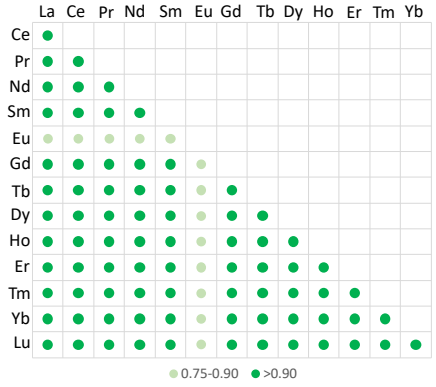

Figure 4.10: Graphical representation of the correlation matrix for ICPM-SFMS untreated data for rare earth elements. Both color (see legend) and dimension of the dots represent the degree of correlation. The bigger the dot, the closer the number is to 1.

volcanic signal, but further analysis will be needed in order to be sure such extreme values are not due to contamination. Li and Ag also display high EF throughout the entire ice core. Li enrichment had previously been documented in antarctic ice cores (Gabrielli et al., 2005b; Siggaard-Andersen et al., 2007; Aarons et al., 2017), although with lower values than what was found on our study.

Rare earth elements have EFs always very close to one, with very low variability, except for the europium anomaly observed in deep samples which may testify to unknown processes involving this element. In general there is good agreement between interglacial, glacial and deep samples, with good agreement especially with the glacial pattern found for REEs in other antarctic ice cores (Gabrielli et al., 2010; Wegner et al., 2012).

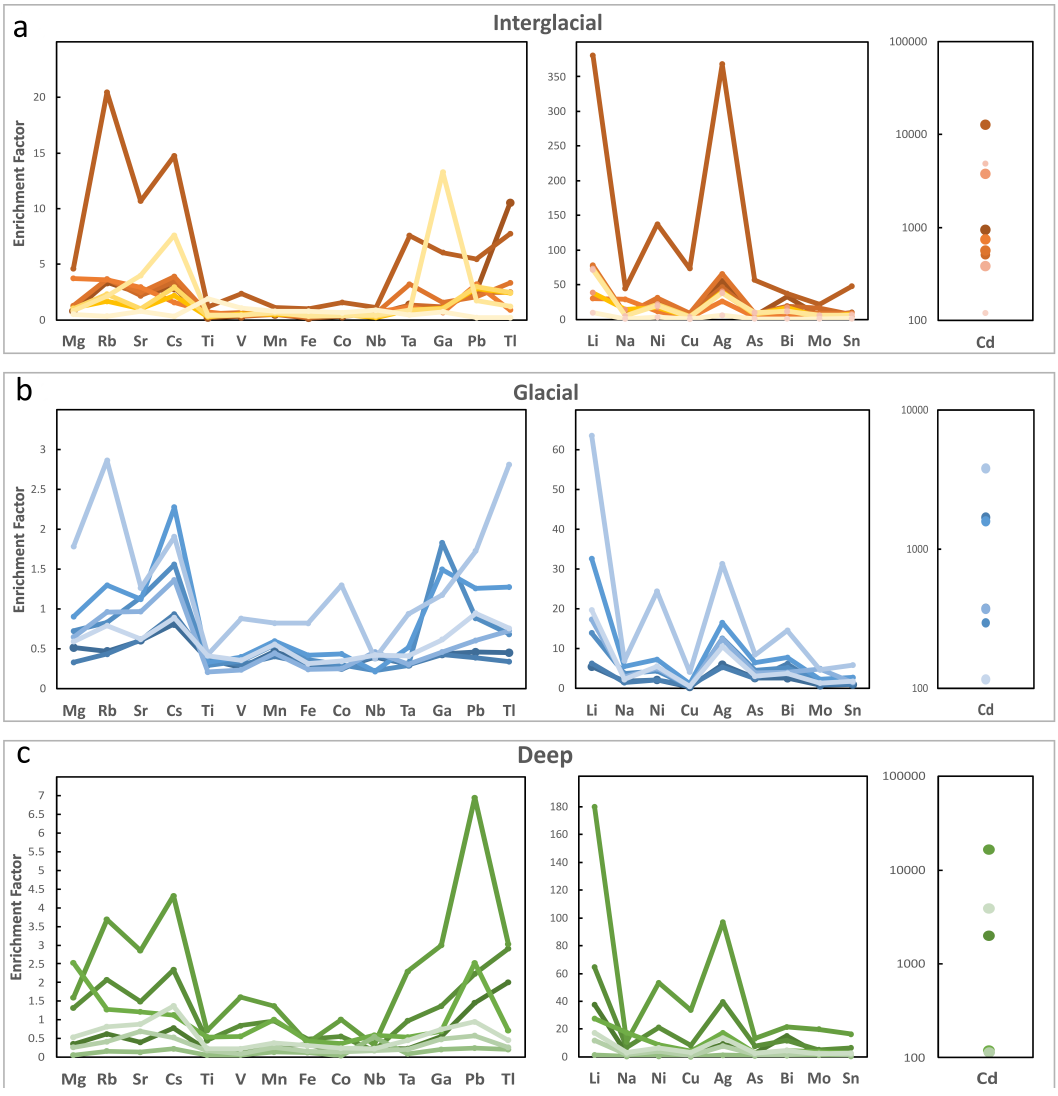

Figure 4.11: Enrichment factors calculated for ICPMS measurements of major and trace elements. Samples were divided into 3 categories: interglacial samples (a), glacial samples (b) and deep samples (c). Each line represents a single sample. Note that Cd was plotted with a logarithmic y-axis.

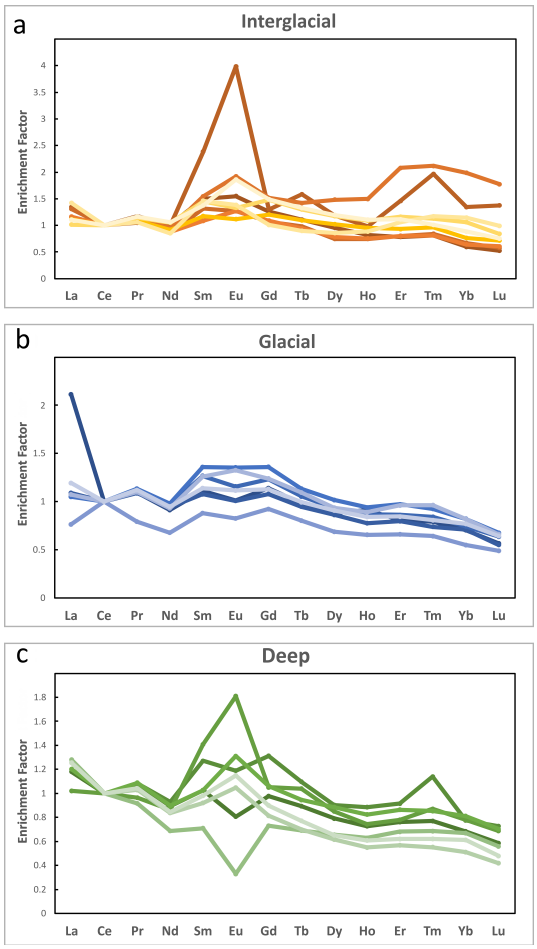

Figure 4.12: Enrichment factors calculated for ICPMS measurements for rare earth elements. Samples were divided into 3 categories: interglacial samples (a), glacial samples (b) and deep samples (c). Each line represents a single sample.

4.3.3 Soluble fraction

Figures 4.13 and 4.14 report a graphical representation of the correlation matrix for the soluble fraction, respectively for major and trace elements, and for REEs. Looking at major and

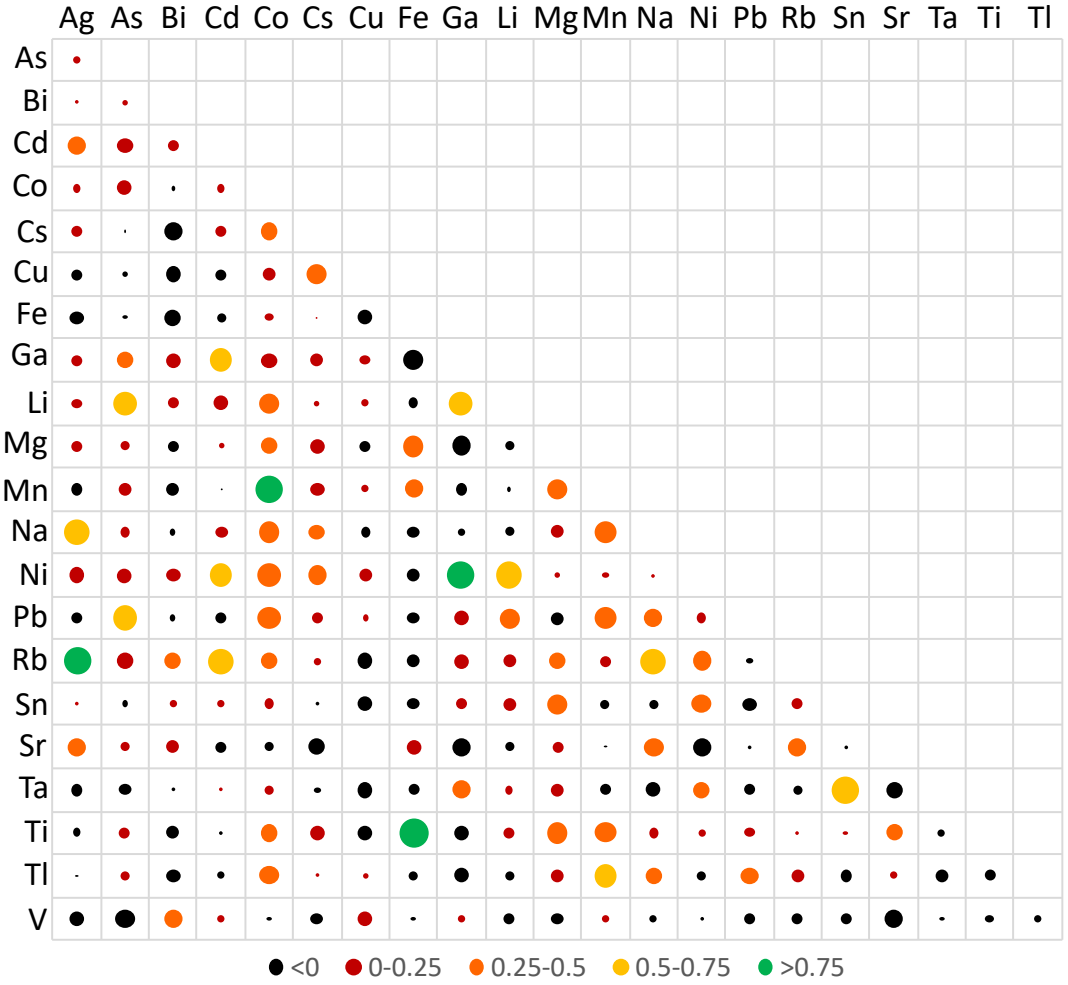

Figure 4.13: Graphical representation of the correlation matrix for ICPM-SFMS filtered data for major and trace elements. Both color (see legend) and dimension of the dots represent the degree of correlation. The bigger the dot, the closer the number is to 1.

trace elements, it is clear that correlations are much less stronger than in the total dissolvable fraction. The only elements which showed high correlations were Ti and Fe (r=0.87), Mn and Co (0.79), Rb and Ag (r=0.78), Ta and Sn (r=0.73). REEs still have a high degree of correlation, although slightly lower than what was found in the total dissolvable fraction. Ce is an evident exception: values are quite low, between 0.5 and 0.6.

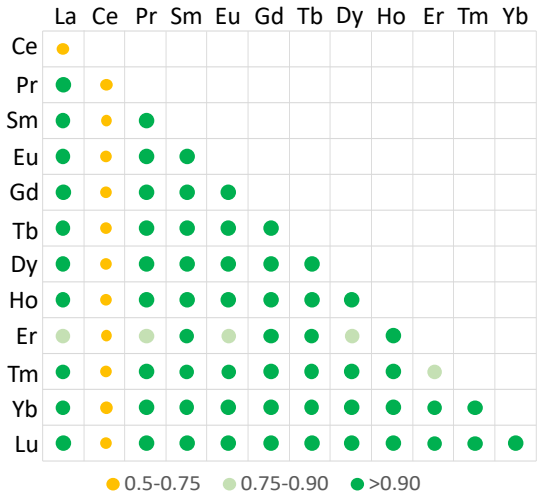

Figure 4.14: Graphical representation of the correlation matrix for ICPM-SFMS filtered data for rare earth elements. Both color (see legend) and dimension of the dots represent the degree of correlation. The bigger the dot, the closer the number is to 1.

4.3.4 EF comparison

Because some elements were measured with both techniques, we were able to calculate two enrichment factors for these elements, one for the INAA dataset and one for the ICP-SFMS dataset. Agreement is generally good for Ti, Mn, V, Fe and Co, although ICP-SFMS values are consistently lower than INAA values. As said before, ICP-SFMS values may be underestimated due to incomplete leaching or partial atomization of the reference element with respect to other elements in the sample.

Nickel was also measured with both techniques, but displays some discrepancies. For interglacial samples, values are quite close to 1 for INAA samples, but approach 100 for ICP-SFMS. For glacial samples, values are consistently higher for ICP-SFMS measurements. Deep samples display great variability for both techniques. Sodium displays the same differences between the two techniques. Some minor discrepancies are also found for Cs, Rb, Sr and Ta, for which INAA values are always quite close to 1, while ICP-SFMS tend to display higher values, although never higher than 10.

Rare earth elements also display some discrepancies in EF calculations. Data from ICP-SFMS are generally quite close to 1, with some samples displaying positive Eu anomalies during interglacials and both positive and negative Eu anomalies in the deep section. EF from INAA samples show more variability. In particular, in glacial samples Yb appears to be greatly enriched and Tm is consistently depleted.

4.4 Solubility study

We performed a solubility study by comparing data from the three different methodologies.

At first we calculate a Solubility Index (SI) using the untreated and filtered ICP-SFMS data, following Equation 4.3.

$$SI = \frac{Filtered}{Untreated} \cdot 100 \tag{4.3}$$

where:

$Filtered$ = Element concentration in the filtered sample
$Untreated$ = Element concentration in the untreated sample

This index was calculated for each sample, and then the mean value was calculated for different climatic stages: Holocene, last glacial maximum (LGM), MIS 3-4, MIS5 and deep samples. Because some samples displayed filtered values higher than the untreated samples, we decided to only consider them if the difference was lower than 10%, to account for instrumental errors. We thus decided to not consider copper and tin, which had too many samples discarded after this selection and may have suffered from contamination during analysis.

Based on this index, we consider:

1. Soluble elements: score > 80
2. Partially Soluble: score 50 - 80
3. Partially insoluble: score 20 - 50
4. insoluble: score < 20

Results can be seen in Tables 4.1, 4.2 and 4.3.

Table 4.1: Solubility Index for major and trace elements

Climatic Stage	Ag	As	Bi	Cd	Co	Cs	Fe	Ga	Li	Mg	Mn	Na	Ni	Pb	Rb	Sr	Ta	Ti	Tl	V
Holocene	102	71	58	35	64	71	71	78	93	51	41	101	99	27	69	71	79	50	47	67
LGM	81	17	58	3	12	25	8	19	93	10	5	82	92	55	41	27	68	8	25	20
MIS3/4	90	25	50	22	22	60	12	40	91	26	24	88	99	21	57	43	96	40	25	28
MIS5	98	28	74	31	48	47	23	45	90	33	18	87	100	32	66	38	75	34	38	31
Deep	94	39	44	7	41	43	13	34	94	24	25	87	98	44	60	31	80	20	42	28

Table 4.2: Solubility Index of REEs.

Climatic Stage	La	Ce	Pr	Sm	Eu	Gd	Tb	Dy	Ho	Er	Tm	Yb	Lu
Holocene	24	26	21	35	43	33	31	20	25	21	34	23	31
LGM	1	1	1	4	8	2	3	2	1	2	4	2	3
MIS3/4	3	11	2	8	13	4	5	2	2	3	7	6	6
MIS5	5	9	6	16	23	10	12	9	8	14	19	11	12
Deep	5	8	8	13	15	11	11	10	10	11	14	10	13

Silver, lithium, sodium, nickel and tantalum are prevalently soluble throughout the ice core. Sodium is expected to have a high solubility as it main source are sea salt sprays. On the other hand, such high solubilities for the other four elements were not expected. For example, Siggaard-Andersen et al. (2007) reported a change in the solubility of lithium in

EPICA Dome C samples during the last glacial/interglacial transition, and attributed it to a shift to different remote source areas. Our findings would suggest a rather uniform supply of soluble Li, probably of local and marine origin. Silver, nickel and tantalum will have to be further investigated to confirm our findings and exclude eventual contamination of the samples. An hypothesis to consider is that some, or all, of these elements may be carried by insoluble particles which are smaller than the filter cut-off (0.2 µm), thus resulting in the soluble fraction when they are indeed insoluble.

The majority of the remaining elements display a similar pattern: highest solubility during Holocene and lowest during LGM, while MIS3/4, MIS5 and deep samples display intermediate behaviors. This is true for As, Cd, Co, Cs, Fe, Ga, Mg, Mn, Sr, Ti, Tl and V. In particular, iron is the element in which this tendency is more pronounced as it shows very high solubility in Holocene samples, and very low solubility for all other samples. Precipitation of iron in deeper samples leading to the formation of jarosite, as previously stated, can explain the decrease in solubility of this element. Iron is also the only element of the dataset which showed a relevant correlation ($r^2 > 0.5$) between depth and SI (Figure 4.15). Bismuth and rubidium show quite intermediate behaviors oscillating between partially soluble and partially insoluble during different periods. Lead is the only element which shows a maximum in solubility during LGM. Rare earth elements display a very consistent insoluble behavior, with slightly

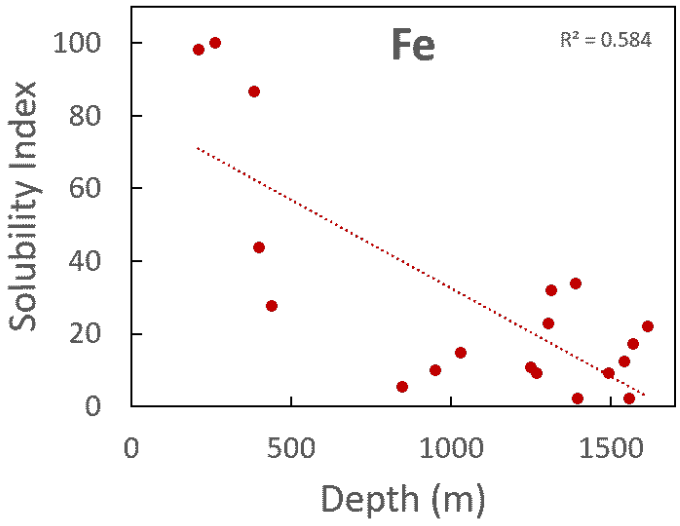

Figure 4.15: Solubility Index of iron plotted against depth (m).

higher values in the Holocene samples.

We also combined the measurements made with ICP-SFMS and INAA to further investigate the solubility of some elements throughout the entire length of the Talos Dome ice core. As before, we assume the untreated ICP-SFMS samples to represent the total concentration of an

Table 4.3: Solubility of the Elements

Solubility	Elements
Soluble	Ag, Li, Na, Ni, Ta
Partially soluble	Bi, Cs, Rb,
Partially insoluble	As, Cd, Co, Fe, Ga, Mg, Mn, Pb, Sr, Ti, Tl, V
Insoluble	Ce, Dy, Er, Eu, Gd, Ho, La, Lu, Pr, Sm, Tb, Tm, Yb

element and the filtered ICP-SFMS samples to represent the soluble fraction of the element, while the INAA samples represent the insoluble fraction. Ideally, the sum of soluble and insoluble should roughly correspond to the total concentration. This is not always the case, as the data for the insoluble fraction does not correspond to the same samples as the total and soluble. We also remind that the total concentration is actually the total dissolvable fraction. Despite this, agreement is generally well inside the error bar. For 21 elements we were able to compare data, as seen in Figures 4.16, 4.17, 4.19, and 4.18. Elements were divided by chemical affinity. We report median values with the corresponding median absolute deviation for three distinct categories of samples: glacial, interglacial and deep.

In Figure 4.16 we show the six transition metals (Ti, V, Mn, Fe, Co and Ni) we were able to measure with all three methodologies.

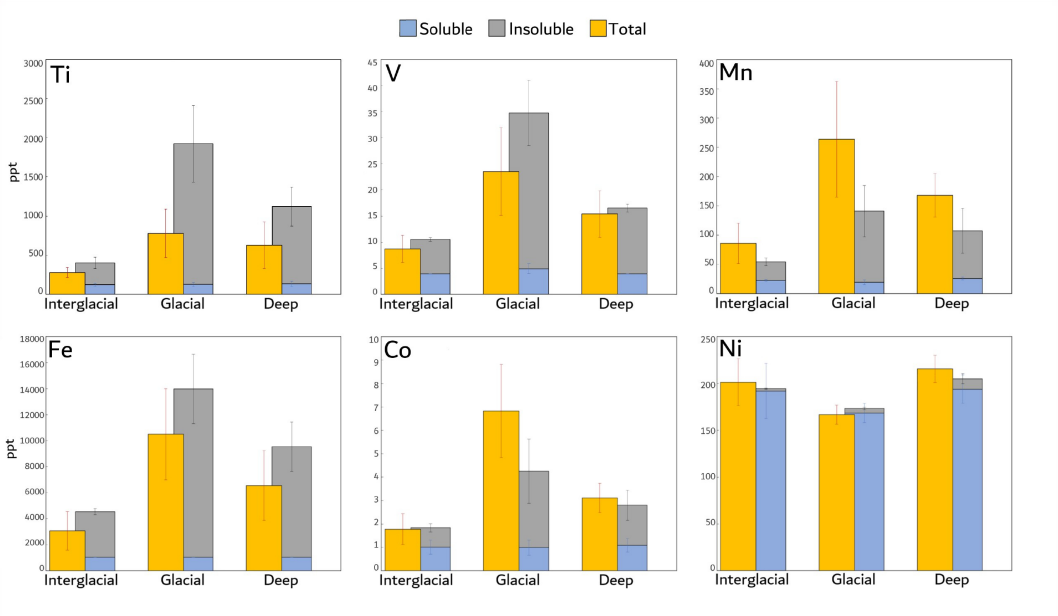

Figure 4.16: Solubility of transition metals. Soluble and total are from ICP-SFMS measurements, insoluble is from INAA.

Titanium, vanadium, manganese, iron and cobalt display a similar behavior. The soluble fraction remains constant and typically quite low with respect to the total, throughout the different categories. On the contrary, the total and insoluble fraction vary: concentration is higher during glacial stages and lower during interglacials, showing a good correlation with

total dust content. This points to a crustal origin of these elements, which travel as aeolian dust from remote sources and are therefore affected by oscillations in the general atmospheric circulation. Deep samples always display an intermediate behavior, which could point to a disturbance in the paleoclimatic signal of this section, leading to an homogenization of the concentration from different climatic periods.

In our samples, iron showed very low concentrations in the dissolved phase, the majority being under our DL, and a higher variability for interglacial and deep samples. Iron in mineral dust typically displays a low fractional solubility $10^{-12} - 10^{-9}$ g/g (Gaspari et al., 2006; Edwards et al., 2006), while we display concentrations of an order of magnitude higher. Fractional solubility percentages are in line with Winton et al. (2016). Spolaor et al. (2013) found that iron associated with fine particles is in a more soluble and bioavailable form during glacial periods than that present during interglacial periods.

Absolute values of cobalt are in line with Gabrielli et al. (2005a) Dome-C samples. Fractionation found in the interglacial is almost equally distributed between soluble and insoluble phase, respectively 55% and 45%, in line with what was found by Grotti et al. (2011) in Antarctic snow samples. For glacial samples the ratio changes to 25% soluble and 75% insoluble. Manganese and vanadium follow a very similar pattern: fractionation between soluble and insoluble for the interglacial is 40:60 for both elements, which shifts to 15:85 for glacial samples. Vanadium interglacial values are in line with De Angelis et al. (1983), while glacial values are quite lower. There is good agreement with data from Greenland snow (Herron et al., 1977). Since particulates are a major contributor to atmospheric vanadium, its transport is expected to closely follow dust profiles (Huang et al., 2015). Titanium displays a similar behavior, but the dissolved phase is significantly and constantly lower than the particulate phase, reaching a ratio of 95:5 for glacial samples and 70:30 for interglacial samples. This is expected as titanium is consistently considered an insoluble element (Wagenbach and Geis, 1989). Nickel displays a very stable behavior through different climatic stages, suggesting a predominant local origin which is not affected by the typical glacial/interglacial pattern of aeolian dust. Comparison between total and soluble is very good, while the insoluble fraction is consistently low. Twining et al. (2012) has shown high levels of nickel in diatoms in the Southern Ocean, which could point to our signal being partially of biological origin. As was also previously mentioned, nickel concentrations can be also influenced by volcanic emissions, which are abundant near Talos Dome. It has to be considered that the ICP-SFMS data displayed high instrumental blanks, comparable to sample level. Nickel is often affected by contamination problems and is rarely determined in ice core samples, such that to our knowledge no comparable data exists.

Figure 4.17 shows the four elements determined from the alkali and alkaline earth metals groups: sodium, rubidium, strontium and cesium. These elements display a higher solubility with respect to the elements from the transition metals group. While it is possible that the soluble Na measurements suffer of a certain degree of contamination from the filtration system, the comparison between the total and the insoluble leaves no doubt of the high solubility of

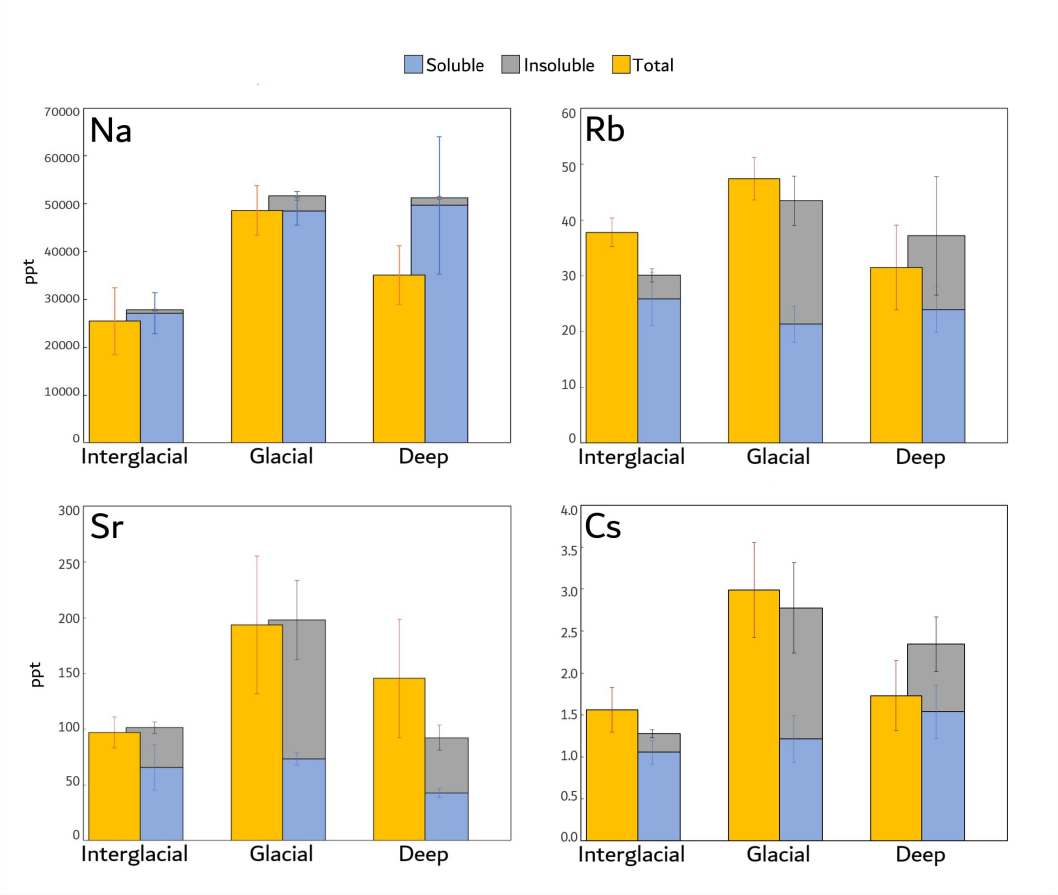

Figure 4.17: Solubility of alkali and alkaline-earth metals.

this element in our samples. This points mainly to a local origin from sea salts. This is coherent with the peripheral position in the Antarctic of the Talos Dome site. In this case the local signal is so strong that even in glacial samples, the insoluble contribution is negligible, unlike what has been observed in inner continental sites such as Dome C and Vostok (De Angelis et al., 1983; Petit et al., 1981). Cesium, rubidium and strontium's insoluble fraction follow the usual glacial-interglacial pattern of aeolian dust. The fractionation ratio of glacial and interglacial samples is inverted with respect to transition metals: during the interglacial both Cs and Rb have a ratio soluble to insoluble of 85:15, while during glacial it is very close to 50:50. Sr displays a perfect inversion: 65% soluble and 35% insoluble for the interglacial samples, the exact opposite for glacial samples. Sr was found to have a significant contribution from sea salts during interglacials (Gabrielli et al., 2005b). The high solubility displayed by this group of elements in interglacial samples is in line with what was found in Antarctic snow samples by Grotti et al. (2011). All four elements display an intermediate behavior in deep samples, as previously observed.

While arsenic displays the typical trend previously seen in transition metals, tantalum shows a peculiar behavior. The insoluble fraction is anomalously high with respect to the total concentration. Tantalum is commonly considered an insoluble element (Filella, 2017) and since our ICP-SFMS values for Ta are quite close to the blank samples, these results have to be considered carefully.

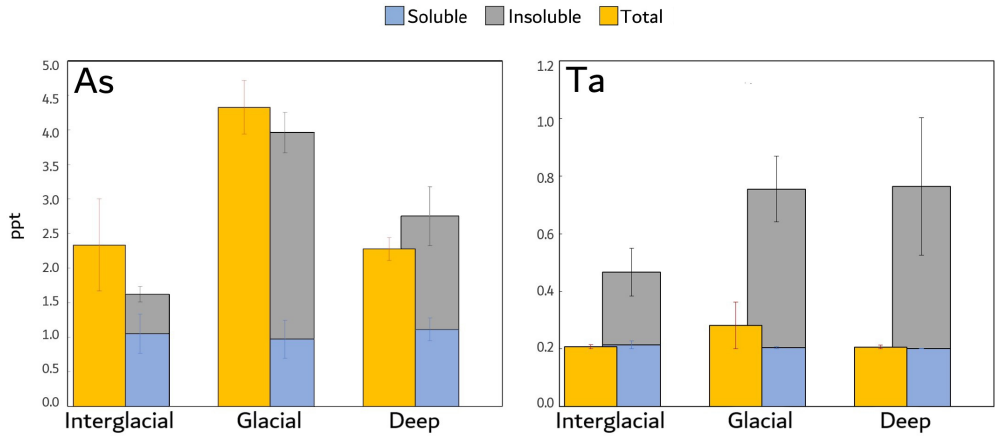

Figure 4.18: Solubility of arsenic and tantalum

Rare earth elements display a consistent insoluble behaviour, as seen in Figure 4.19.

For glacial samples, all considered REEs show very high insoluble fractions: apart from Eu and Sm which have respectively 80% and 85%, all other REEs display percentages above 90%. This is consistent with the geochemical properties of REEs, which are only poorly soluble (Henderson, 1984). The restricted mobility of REEs is related to their adsorption on solid particles due to the formation of ion pairs on the particle surface (Dubinin, 2004). Europium represents an exception. While other lanthanides exclusively form trivalent ions,

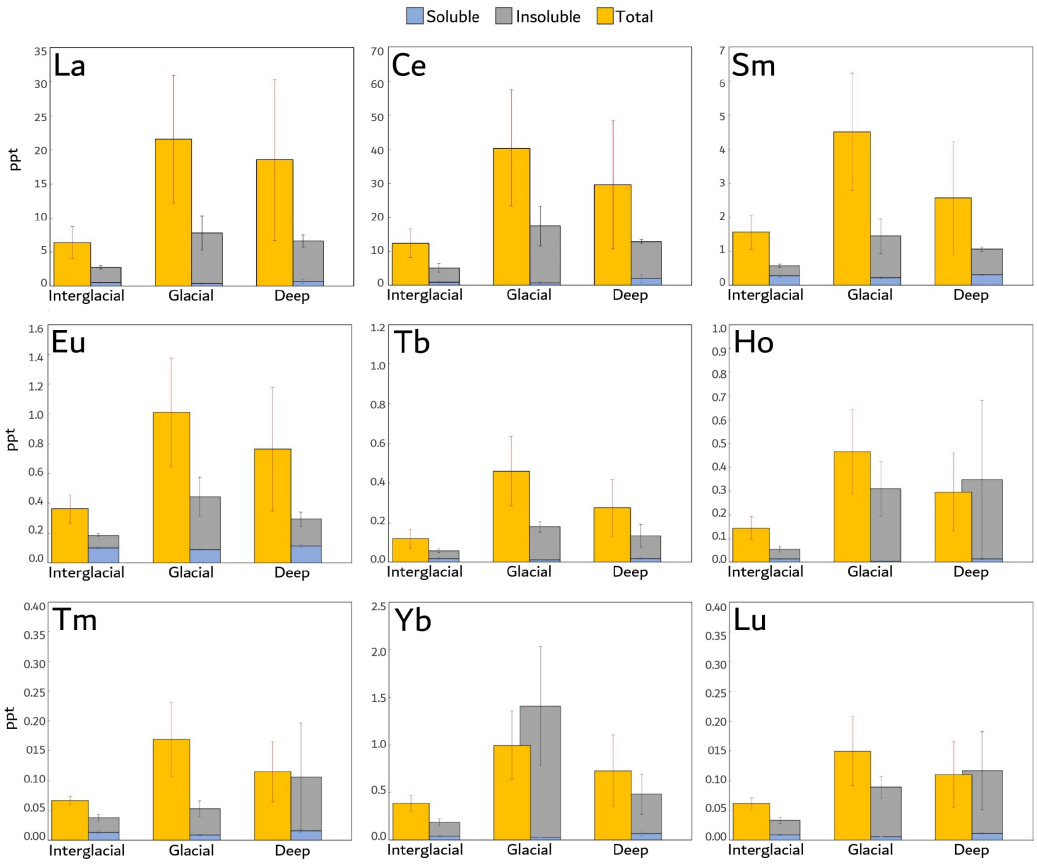

Figure 4.19: Solubility of REEs

Eu also holds the possibility to form bivalent ions, thus gaining the possibility to substitute Ca^{+} in plagioclase minerals. This translates to an higher environmental mobility of Europium. Cerium also represents an anomaly as it forms quadrivalent ions.

Chapter 5

Conclusions

5.1 Physical and chemical alterations of deep ice

We decided to deepen our knowledge of the deep section of the Talos Dome ice core, since due to its dating uncertainties it had been neglected. Grain size anomalies emerge from the mineral dust record, and are much more evident if we look at granulometric indexes such as FPP and CLPP. The increase in modal dust size and the departure from a log-normal distribution point to post-depositional artefacts consisting of dust aggregates. These are uncorrelated to dust sources and transport.

Physical alteration is not the only evidence for post-depositional processes occurring inside deep ice. We have documented the presence of jarosite, a ferric-potassium hydroxide sulphate mineral which typically forms as a result of chemical weathering in environments which are acidic, rich in iron and with limited presence of liquid water. We hypothesize that jarosite acts as a cement in the aggregates, making them resistant to breaking through the use of ultrasonic waves. The distribution of other elements further supports chemical weathering in the deep section of the ice core: Mg, Ca and Na are almost absent from jarosite precipitates and scarce within Si-rich grains, while more present in Holocene and glacial samples. The removal of soluble and labile fractions in mineral is one of the most common weathering processes.

Our findings suggest that dust alteration in deep ice happens as a result of specific conditions: 1) concentration of impurities at graind boundaries, which is a consequence of ice metamorphism taking place at depths where the ice temperature is close to the pressure melting point; 2) occurrence of highly saline and acidic fluids, spatially limited to the grain boundaries. When both these conditions are met, dust alteration in the form of dissolution of the original dust particles and precipitation of new mineral phases, such as jarosite, may take place.

5.2 Crustal and non-crustal contributions to the concentration of impurities

We further investigated the elemental composition of dust in the Talos Dome ice core with INAA and ICP-SFMS measurements and used enrichment factors and correlation matrices to evaluate the crustal origin of elements.

The high correlations and low enrichment factors found among insoluble elements confirm a prevalent crustal source for mineral dust. In particular transition metals (Fe, Ti, Mn, Co, V) are very highly correlated ($r>0.85$) and maintain this correlation in both the insoluble and the total dissolvable fraction confirming no other significant contributions other than the crustal one.

Apart from the Earth's crust, contribution to mineral dust can derive from volcanic eruptions and marine emissions, in the form of sea salt sprays and biogenic emissions. Although marine contributions are generally considered to be more soluble, fractionation to the solid phase is not negligible, as testified by our records of mercury and selenium. These two elements are heavily enriched and highly correlated between each other in our insoluble record, pointing to a common source; biogenic emissions and sea salt sprays play an important role as a source for these elements.

When pronounced differences in correlations between the insoluble and the total fraction are found, it points to a major contribution of the soluble fraction to the total budget of an element. It is evident if we look at sodium, which displays a high correlation to crustal elements in its insoluble fraction,but not in the total dissolvable concentration, where it only matches with magnesium. This result clearly points to a strong signal from sea salt aerosols, of which both sodium and and magnesium are major components, affecting concentrations at Talos Dome.

Finally, the concentration of some elements is the probable result of a mixture of different sources, both terrestrial and marine, making the signal harder to read. Some, like arsenic and strontium, may display high correlation with crustal elements but also high enrichment factors. Others, like calcium and nickel, may present counterintuitive correlations with other elements and will need further studies in order to draw significant conclusions.

5.3 Solubility trends across different climatic periods

By comparing ICP-SFMS filtered and untreated samples we evaluated the solubility for each considered element at different depths of the ice core. Overall, the majority of elements exhibits a minimum in solubility during the last glacial maximum. This is the result of higher fluxes of mineral dust which were transported to the antarctic continent from remote sources and is consistent with the crustal origin we documented for the better part of the elements considered.

Many elements also showed a maximum in solubility in shallower samples, belonging to the Holocene. This is especially evident when we look at rare earth elements, which displayed a consistently insoluble behavior except for Holocene samples. Despite this, no clear trends connected to depth were found, except for iron. The decrease of iron's solubility with depth further supports the chemical weathering of the deeper sections of the ice core involving Fe precipitation to form jarosite. This result also highlights the high sensitivity of iron with respect to post-depositional processes, posing issues on its study in deep ice cores.

When comparing INAA and ICP-SFMS data, the soluble fraction typically remains constant throughout the different categories (interglacial, glacial, deep) while the total and insoluble fraction vary. Typically, concentrations are higher during glacial stages and lower during interglacials, showing a good correlation with total dust content. This further confirms the crustal origin of these elements, which travel as aeolian dust from remote sources and are therefore affected by oscillations in the general atmospheric circulation. It is also possible that remote dust experiences chemical alteration during its prolonged transport, removing the most volatile and soluble fraction of dust before it reaches Antarctica and deposits. Interglacial samples which have a higher contribution from local sources would be less affected by these processes, retaining a higher proportion of the more soluble elements.

Deep samples always display an intermediate behavior, which could point to a disturbance in the paleoclimatic signal of this section, leading to an homogenization of the concentration from different climatic periods. The consistency of the soluble fraction suggest this is mainly derived by local sources and therefore less affected by glacial/interglacial cycles. This may be linked to local mineral dust sources, contributions from sea salt sprays and volcanic signals.

Five elements were found to be completely soluble throughout the entire ice core, and three more have shown strong solubility tendencies. These elements belong mainly to the alkaline series (Li, Na, Rb, Cs), but we also find some transition metals (Ni, Ag, Ta) and a metal (Bi). High EFs for these elements further suggest a non-crustal source. While we can safely point to sea salt aerosols as the dominant source for sodium, further studies will be needed for the other elements in order to exclude contamination of the ICP-SFMS samples and better determine their sources. We can suggest two plausible hypothesis, which do not exclude one another:

- a predominant local origin for these elements, which is not affected by the typical glacial/interglacial pattern of aeolian dust. It is possible that enrichment of these elements is of volcanic origin. Talos Dome is in fact characterized by a pervasive and constant presence of a volcanic signal detected as background aerosol, which is the result of aeolian remobilization of local volcanic material (Delmonte et al., 2013).
- a significant bond of these elements with insoluble particles smaller than 0.2 µm, which would not be retained by the filter thus altering our soluble fraction.

Rare Earth elements were measured both with INAA and ICP-SFMS. They present a typical crustal behavior, with crustal-like concentrations and low solubility. No evident differences

were observed along the core, confirming that these set of elements is among the most suited to track crustal material, regardless of weathering.

5.4 Future perspectives

With this study we have proven the existence of post-depositional processes which physically and chemically alter mineral dust in the deeper sections of the ice core. These findings are of particular relevance for future intepretation of dust records in deep ice cores, especially in the light of new drillings which aim at retrieving older and deeper ice cores.

In particular, we have observed the presence of dust aggregates. Our first attempts in processing them through the use of an ultrasonic bath were not successful, due to high risk of contamination and to the high persistence of the aggregates, which are likely tightly bound together by jarosite, which acts as a cement. Further studies are needed in this direction in order to noticeably lower the risk of contamination and to find appropriate intensities and sonication times in order to break the aggregates.

Furthermore, this study was a first attempt in comparing INAA and ICP-SFMS data to study the solubility of different elements inside ice cores. Further studies will have to expand the current record, especially for INAA samples, which were only 16 in this study as they take longer analysis, in order to obtain a better statistical significance. A special focus on analysis of the more soluble elements in the deep part of TALDICE with ICP-SFMS may provide further insight in chemical weathering processes which were briefly investigated through SEM analysis in this work. At last, expanding a similar study to different ice cores may help to better pinpoint the different contributions of the elements in their soluble and insoluble fractions.

Bibliography

Aarons, S. M., Aciego, S. M., Arendt, C. A., Blakowski, M. A., Steigmeyer, A., Gabrielli, P., Sierra-Hernández, M. R., Beaudon, E., Delmonte, B., Baccolo, G., May, N. W., and Pratt, K. A. (2017). Dust composition changes from Taylor Glacier (East Antarctica) during the last glacial-interglacial transition: A multi-proxy approach. *Quat. Sci. Rev.*, 162:60–71.

Aarons, S. M., Aciego, S. M., Gabrielli, P., Delmonte, B., Koornneef, J. M., Wegner, A., and Blakowski, M. A. (2016). The impact of glacier retreat from the Ross Sea on local climate : Characterization of mineral dust in the Taylor Dome ice core , East Antarctica. *Earth Planet. Sci. Lett.*, 444:34–44.

Albani, S., Delmonte, B., Maggi, V., Baroni, C., Petit, J. R., Stenni, B., Mazzola, C., and Frezzotti, M. (2012). Interpreting last glacial to Holocene dust changes at Talos Dome (East Antarctica): Implications for atmospheric variations from regional to hemispheric scales. *Clim. Past*, 8(2):741–750.

Anderson, D. L. and Benson, C. S. (1963). The Densification and Diagenesis of Snow. *Ice Snow Prop. Process. Appl.*, page 21.

Angelis, M. D., Barkov, N. I., and Petrov, V. N. (1987). Aerosol concentrations over the last climatic cycle (160 kyr) from an Antarctic ice core. *Nature*, 325(6102):318–321.

Baccolo, G., Cibin, G., Delmonte, B., Hampai, D., Marcelli, A., Di Stefano, E., Macis, S., and Maggi, V. (2018a). The Contribution of Synchrotron Light for the Characterization of Atmospheric Mineral Dust in Deep Ice Cores: Preliminary Results from the Talos Dome Ice Core (East Antarctica). *Condens. Matter*, 3(3):25.

Baccolo, G., Clemenza, M., Delmonte, B., Maffezzoli, N., Nastasi, M., Previtali, E., Prata, M., Salvini, A., and Maggi, V. (2016a). A new method based on low background instrumental neutron activation analysis for major, trace and ultra-trace element determination in atmospheric mineral dust from polar ice cores. *Anal. Chim. Acta*, 922:11–18.

Baccolo, G., Clemenza, M., Delmonte, B., Salvini, A., and Maggi, V. (2016b). A new method based on low background instrumental neutron activation analysis for major , trace and ultra-trace element determination in atmospheric mineral dust from polar ice cores Niccol o. *Anal. Chim. Acta*, 922:11–18.

Baccolo, G., Delmonte, B., Albani, S., Baroni, C., and Cibin, G. (2018b). Regionalization of the Atmospheric Dust Cycle on the Periphery of the East Antarctic Ice Sheet Since the Last Glacial Maximum Geochemistry , Geophysics , Geosystems. pages 3540–3554.

Baccolo, G., Delmonte, B., Niles, P., Cibin, G., Di Stefano, E., Hampai, D., Keller, L., Maggi, V., Marcelli, A., Michalski, J., Snead, C., and Frezzotti, M. (2021). Jarosite formation in deep Antarctic ice provides a window into acidic, water-limited weathering on Mars. *Nat. Commun.*, 12:1–8.

Baccolo, G., Maffezzoli, N., Clemenza, M., Delmonte, B., Prata, M., Salvini, A., Maggi, V., and Previtali, E. (2015). Low-background neutron activation analysis: a powerful tool for atmospheric mineral dust analysis in ice cores. *J. Radioanal. Nucl. Chem.*, 306(3):589–597.

Barrett, P. (2003). Cooling a continent. *Nature*, 24(1):37–45.

Basile, I., Grousset, F. E., Revel, M., Robert, J., and Biscaye, P. E. (1997). Patagonian origin of glacial dust deposited in East Antarctica (Vostok and Dome C) during glacial stages 2, 4 and 6. *Earth Planet. Sci. Lett.*, 146:573–589.

Bazin, L., Landais, A., Lemieux-Dudon, B., Toyé Mahamadou Kele, H., Veres, D., Parrenin, F., Martinerie, P., Ritz, C., Capron, E., Lipenkov, V., Loutre, M. F., Raynaud, D., Vinther, B., Svensson, A., Rasmussen, S. O., Severi, M., Blunier, T., Leuenberger, M., Fischer, H., Masson-Delmotte, V., Chappellaz, J., and Wolff, E. (2013). An optimized multi-proxy, multi-site Antarctic ice and gas orbital chronology (AICC2012): 120-800 ka. *Clim. Past*, 9(4):1715–1731.

Borio di Tigliole, A., Cammi, A., Chiesa, D., Clemenza, M., Manera, S., Nastasi, M., Pattavina, L., Ponciroli, R., Pozzi, S., Prata, M., Previtali, E., Salvini, A., and Sisti, M. (2014). TRIGA reactor absolute neutron flux measurement using activated isotopes. *Prog. Nucl. Energy*, 70:249–255.

Bory, A., Wolff, E., Mulvaney, R., Jagoutz, E., Wegner, A., Ruth, U., and Elderfield, H. (2010). Multiple sources supply eolian mineral dust to the Atlantic sector of coastal Antarctica: Evidence from recent snow layers at the top of Berkner Island ice sheet. *Earth Planet. Sci. Lett.*, 291(1-4):138–148.

Bradley, R. S. (2014). *Paleoclimatology: Reconstructing Climates of the Quaternary: Third Edition*.

Brook, E. J., White, J. W., Schilla, A. S., Bender, M. L., Barnett, B., Severinghaus, J. P., Taylor, K. C., Alley, R. B., and Steig, E. J. (2005). Timing of millennial-scale climate change at Siple Dome, West Antarctica, during the last glacial period. *Quat. Sci. Rev.*, 24(12-13):1333–1343.

Chu, S., Ekstrom, L., and Firestone, R. (1999). The Lund/LBNL Nuclear Data Search [Online]: www.nucleardata.nuclear.lu.se/toi.

Craig, H. (1961). Isotopic variations in meteoric waters. *Science (80-.).*, 133(3465):1702–1703.

Currie, L. A. (1968). Limits for qualitative detection and quantitative determination. Application to radiochemistry. *Anal. Chem.*, 40(3):586–593.

Damaske, D., Schreckenberger, B., and Goldmann, F. (2014). A high resolution aeromagnetic survey over the Mesa Range, northern Victoria Land, Antarctica. *Polarforschung*, 84(1):1–13.

De Angelis, M., Legrand, M., Petit, J. R., Barkov, N. I., Korotkevitch, Y. S., and Kotlyakov, V. M. (1983). Soluble and insoluble impurities along the 950 m deep Vostok ice core (Antarctica) - Climatic implications. *J. Atmos. Chem.*, 1(3):215–239.

De Angelis, M., Tison, J. L., Morel-Fourcade, M. C., and Susini, J. (2013). Micro-investigation of EPICA Dome C bottom ice: Evidence of long term in situ processes involving acid-salt interactions, mineral dust, and organic matter. *Quat. Sci. Rev.*, 78:248–265.

De Deckker, P. (2020). Airborne dust traffic from Australia in modern and Late Quaternary times. *Glob. Planet. Change*, 184(October 2019):103056.

De Deckker, P., Norman, M., Goodwin, I. D., Wain, A., and Gingele, F. X. (2010). Lead isotopic evidence for an Australian source of aeolian dust to Antarctica at times over the last 170,000 years. *Palaeogeogr. Palaeoclimatol. Palaeoecol.*, 285(3-4):205–223.

Delmonte, B., Andersson, P. S., Hansson, M., Schöberg, H., Petit, J. R., Basile-Doelsch, I., and Maggi, V. (2008). Aeolian dust in East Antarctica (EPICA-Dome C and Vostok): Provenance during glacial ages over the last 800 kyr. *Geophys. Res. Lett.*, 35(7):2–7.

Delmonte, B., Andersson, P. S., Schöberg, H., Hansson, M., Petit, J. R., Delmas, R., Gaiero, D. M., Maggi, V., and Frezzotti, M. (2010a). Geographic provenance of aeolian dust in East Antarctica during Pleistocene glaciations: preliminary results from Talos Dome and comparison with East Antarctic and new Andean ice core data. *Quat. Sci. Rev.*, 29(1-2):256–264.

Delmonte, B., Baroni, C., Andersson, P. S., Narcisi, B., Salvatore, M. C., Petit, J. R., Scarchilli, C., Frezzotti, M., Albani, S., and Maggi, V. (2013). Modern and Holocene aeolian dust variability from Talos Dome (Northern Victoria Land) to the interior of the Antarctic ice sheet. *Quat. Sci. Rev.*, 64:76–89.

Delmonte, B., Baroni, C., Andersson, P. S., Schoberg, H., Hansson, M., Aciego, S., Petit, J. R., Albani, S., Mazzola, C., Maggi, V., and Frezzotti, M. (2010b). Aeolian dust in the Talos Dome ice core (East Antarctica, Pacific/Ross Sea sector): Victoria Land versus remote sources over the last two climate cycles. *J. Quat. Sci.*, 25(8):1327–1337.

Delmonte, B., Paleari, C. I., Andò, S., Garzanti, E., Andersson, P. S., Petit, J. R., Crosta, X., Narcisi, B., Baroni, C., Salvatore, M. C., Baccolo, G., and Maggi, V. (2017). Causes of dust size variability in central East Antarctica (Dome B): Atmospheric transport from expanded South American sources during Marine Isotope Stage 2. *Quat. Sci. Rev.*, 168:55–68.

Delmonte, B., Petit, J. R., Andersen, K. K., Basile-Doelsch, I., Maggi, V., and Lipenkov, V. Y. (2004). Dust size evidence for opposite regional atmospheric circulation changes over east Antarctica during the last climatic transition. *Clim. Dyn.*, 23(3-4):427–438.

Delmonte, B., Petit, R., and Maggi, V. (2002). Glacial to Holocene implications of the new 27000-year dust record from the EPICA Dome C (East Antarctica) ice core. pages 647–660.

Dubinin, A. V. (2004). Geochemistry of rare earth elements in the ocean. *Lithol. Miner. Resour.*, 39(4):289–307.

Durand, G., Svensson, A., Persson, A., Gagliardini, O., Gillet-Chaulet, F., Sjolte, J., Montagnat, M., and Dahl-Jensen, D. (2009). Evolution of the Texture along the EPICA Dome C Ice Core.

Ebinghaus, R., Kock, H. H., Temme, C., Einax, J. W., Löwe, A. G., Richter, A., Burrows, J. P., and Schroeder, W. H. (2002). Antarctic springtime depletion of atmospheric mercury. *Environ. Sci. Technol.*, 36(6):1238–1244.

Edwards, R., Sedwick, P., Morgan, V., and Boutron, C. (2006). Iron in ice cores from Law Dome: A record of atmospheric iron deposition for maritime East Antarctica during the Holocene and Last Glacial Maximum. *Geochemistry, Geophys. Geosystems*, 7(12).

EPICA Community Members (2004). Eight glacial cycles from an Antarctic ice core. *Nature*, 429:623–628.

EPICA Community Members (2006). One-to-one coupling of glacial climate variability in Greenland and Antarctica. *Nature*, 444(7116):195–198.

Faria, H., Freitag, J., and Kipfstuhl, S. (2010). Polar ice structure and the integrity of ice-core paleoclimate records. *Quat. Sci. Rev.*, 29:338–351.

Filella, M. (2017). Tantalum in the environment. *Earth-Science Rev.*, 173(June):122–140.

Fischer, H., Fundel, F., Ruth, U., Twarloh, B., Wegner, A., Udisti, R., Becagli, S., Castellano, E., Morganti, A., Severi, M., Wolff, E., Littot, G., Röthlisberger, R., Mulvaney, R., Hutterli, M. A., Kaufmann, P., Federer, U., Lambert, F., Bigler, M., Hansson, M., Jonsell, U., de Angelis, M., Boutron, C., Siggaard-Andersen, M. L., Steffensen, J. P., Barbante, C., Gaspari, V., Gabrielli, P., and Wagenbach, D. (2007). Reconstruction of millennial changes in dust emission, transport and regional sea ice coverage using the deep EPICA ice cores from the Atlantic and Indian Ocean sector of Antarctica. *Earth Planet. Sci. Lett.*, 260(1-2):340–354.

Fischer, H., Severinghaus, J., Brook, E., Wolff, E., Albert, M., Alemany, O., Arthern, R., Bentley, C., Blankenship, D., Chappellaz, J., Creyts, T., Dahl-Jensen, D., Dinn, M., Frezzotti, M., Fujita, S., Gallee, H., Hindmarsh, R., Hudspeth, D., Jugie, G., Kawamura, K., Lipenkov, V., Miller, H., Mulvaney, R., Parrenin, F., Pattyn, F., Ritz, C., Schwander, J., Steinhage, D., Van Ommen, T., and Wilhelms, F. (2013). Where to find 1.5 million yr old ice for the IPICS "Oldest-Ice" ice core. *Clim. Past*, 9(6):2489–2505.

Fountain, A. G., Nylen, T. H., Monaghan, A., Basagic, H. J., and Bromwich, D. (2010). Snow in the Mcmurdo Dry Valleys, Antarctica. *Int. J. Climatol.*, 30(5):633–642.

Fretwell, P., Pritchard, H. D., Vaughan, D. G., Bamber, J. L., Barrand, N. E., Bell, R., Bianchi, C., Bingham, R. G., Blankenship, D. D., Casassa, G., Catania, G., Callens, D., Conway, H., Cook, A. J., Corr, H. F., Damaske, D., Damm, V., Ferraccioli, F., Forsberg, R., Fujita, S., Gim, Y., Gogineni, P., Griggs, J. A., Hindmarsh, R. C., Holmlund, P., Holt, J. W., Jacobel, R. W., Jenkins, A., Jokat, W., Jordan, T., King, E. C., Kohler, J., Krabill, W., Riger-Kusk, M., Langley, K. A., Leitchenkov, G., Leuschen, C., Luyendyk, B. P., Matsuoka, K., Mouginot, J., Nitsche, F. O., Nogi, Y., Nost, O. A., Popov, S. V., Rignot, E., Rippin, D. M., Rivera, A., Roberts, J., Ross, N., Siegert, M. J., Smith, A. M., Steinhage, D., Studinger, M., Sun, B., Tinto, B. K., Welch, B. C., Wilson, D., Young, D. A., Xiangbin, C., and Zirizzotti, A. (2013). Bedmap2: Improved ice bed, surface and thickness datasets for Antarctica. *Cryosphere*, 7(1):375–393.

Frezzotti, M., Bitelli, G., De Michelis, P., Deponti, A., Forieri, A., Gandolfi, S., Maggi, V., Mancini, F., Remy, F., Tabacco, I. E., Urbini, S., Vittuari, L., and Zirizzotti, A. (2004). Geophysical survey at Talos Dome, East Antarctica: The search for a new deep-drilling site. *Ann. Glaciol.*, 39(2002):423–432.

Fudge, T. J., Steig, E. J., Markle, B. R., Schoenemann, S. W., Ding, Q., Taylor, K. C., McConnell, J. R., Brook, E. J., Sowers, T., White, J. W., Alley, R. B., Cheng, H., Clow, G. D., Cole-Dai, J., Conway, H., Cuffey, K. M., Edwards, J. S., Lawrence Edwards, R., Edwards, R., Fegyveresi, J. M., Ferris, D., Fitzpatrick, J. J., Johnson, J., Hargreaves, G., Lee, J. E., Maselli, O. J., Mason, W., McGwire, K. C., Mitchell, L. E., Mortensen, N., Neff, P., Orsi, A. J., Popp, T. J., Schauer, A. J., Severinghaus, J. P., Sigl, M., Spencer, M. K., Vaughn, B. H., Voigt, D. E., Waddington, E. D., Wang, X., and Wong, G. J. (2013). Onset of deglacial warming in West Antarctica driven by local orbital forcing. *Nature*, 500(7463):440–444.

Gabrielli, P., Barbante, C., Boutron, C., Cozzi, G., Gaspari, V., Planchon, F., Ferrari, C., Turetta, C., Hong, S., and Cescon, P. (2005a). Variations in atmospheric trace elements in Dome C (East Antarctica) ice over the last two climatic cycles. *Atmos. Environ.*, 39(34):6420–6429.

Gabrielli, P., Barbante, C., Turetta, C., Marteel, A., Boutron, C., Cozzi, G., Cairns, W., Ferrari, C., and Cescon, P. (2006). Direct determination of rare earth elements at the subpicogram per gram level in antarctic ice by ICP-SFMS using a desolvation system. *Anal. Chem.*, 78(6):1883–1889.

Gabrielli, P., Planchon, F. A., Hong, S., Lee, K. H., Hur, S. D., Barbante, C., Ferrari, C. P., Petit, J. R., Lipenkov, V. Y., Cescon, P., and Boutron, C. F. (2005b). Trace elements in Vostok Antarctic ice during the last four climatic cycles. *Earth Planet. Sci. Lett.*, 234(1-2):249–259.

Gabrielli, P., Wegner, A., Petit, J. R., Delmonte, B., De Deckker, P., Gaspari, V., Fischer, H., Ruth, U., Kriews, M., Boutron, C., Cescon, P., and Barbante, C. (2010). A major

glacial-interglacial change in aeolian dust composition inferred from Rare Earth Elements in Antarctic ice. *Quat. Sci. Rev.*, 29(1-2):265–273.

Galeotti, S., DeConto, R., Naish, T., Stocchi, P., Florindo, F., Pagani, M., Barrett, P., Bohaty, Steven M and Lanci, L., Pollard, D., Sandroni, S., Talarico, F. M., and Zachos, J. C. (2016). Antarctic Ice Sheet variability across the Eocene-Oligocene boundary climate transition. *Res. Reports*.

Gaspari, V., Barbante, C., Cozzi, G., Cescon, P., Boutron, C. F., Gabrielli, P., Capodaglio, G., Ferrari, C., Petit, J. R., and Delmonte, B. (2006). Atmospheric iron fluxes over the last deglaciation: Climatic implications. *Geophys. Res. Lett.*, 33(3):5–8.

Gasson, E., DeConto, R. M., Pollard, D., and Levy, R. H. (2016). Dynamic Antarctic ice sheet during the early to mid-Miocene. *Proc. Natl. Acad. Sci. U. S. A.*, 113(13):3459–3464.

Gili, S., Gaiero, D. M., Goldstein, S. L., Chemale, F., Jweda, J., Kaplan, M. R., Becchio, R. A., and Koester, E. (2017). Glacial/interglacial changes of Southern Hemisphere wind circulation from the geochemistry of South American dust. *Earth Planet. Sci. Lett.*, 469:98–109.

Goldstein, J. I., Newbury, D. E., Echlin, P., Joy, D. C., Romig, A. D., Lyman, C. E., Fiori, C., Lifshin, E., Goldstein, J. I., Newbury, D. E., Echlin, P., Joy, D. C., Romig, A. D., Lyman, C. E., Fiori, C., and Lifshin, E. (1992). Coating and Conductivity Techniques for SEM and Microanalysis. *Scanning Electron Microsc. X-Ray Microanal.*, pages 671–740.

Greenberg, R. R., Bode, P., and De Nadai Fernandes, E. A. (2011). Neutron activation analysis: A primary method of measurement. *Spectrochim. Acta - Part B At. Spectrosc.*, 66(3-4):193–241.

Grootes, P. M., Steig, E. J., Stuiver, M., Waddington, E. D., Morse, D. L., and Nadeau, M. J. (2001). The Taylor Dome Antarctic 18O record and globally synchronous changes in climate. *Quat. Res.*, 56(3):289–298.

Grotti, M., Soggia, F., Ardini, F., and Magi, E. (2011). Major and trace element partitioning between dissolved and particulate phases in Antarctic snow. *J. Environ. Monit.*, 13:2511–2520.

Grousset, F. E., Biscaye, P. E., and Revel, M. (1992). Antarctic (Dome C) ice-core dust at 18 ky B.P.: Isotopic constraints on origins. *Earth Planet. Sci. Lett.*, 111:175–182.

Hammer, C. U., Clausen, H. B., and Langway, C. C. (1994). Electrical conductivity method (ECM) stratigraphic dating of the Byrd Station ice core, Antarctica. *Ann. Glaciol.*, 20:115–120.

Henderson, P. (1984). Rare Earth Element Geochemistry.

Herron, M. M., Langway, C. C., Weiss, H. V., and Cragin, J. H. (1977). Atmospheric trace metals and sulfate in the Greenland Ice Sheet. *Geochim. Cosmochim. Acta*, 41(7):915–920.

Hochmuth, K., Gohl, K., Leitchenkov, G., Sauermilch, I., Whittaker, J. M., Uenzelmann-Neben, G., Davy, B., and De Santis, L. (2020). The Evolving Paleobathymetry of the Circum-Antarctic Southern Ocean Since 34 Ma: A Key to Understanding Past Cryosphere-Ocean Developments. *Geochemistry, Geophys. Geosystems*, 21(8):1–28.

Huang, J., Mendoza, B., Daniel, J. S., Nielsen, C. J., Rotstayn, L., and Wild, O. (2013). Anthropogenic and natural radiative forcing. *Clim. Chang. 2013 Phys. Sci. Basis Work. Gr. I Contrib. to Fifth Assess. Rep. Intergov. Panel Clim. Chang.*, 9781107057:659–740.

Huang, J. H., Huang, F., Evans, L., and Glasauer, S. (2015). Vanadium: Global (bio)geochemistry. *Chem. Geol.*, 417:68–89.

ice core research group, D.-F. (1998). Preliminary investigation of palaeoclimate signals recorded in the ice core from Dome Fuji station, east Dronning Maud Land, Antarctica. *Ann. Glaciol.*

Ingolfsson, O. (2004). Quaternary glacial and climate history of Antarctica. In *Quat. Glaciat. Chronol. Part III South Am. Asia, Africa, Australas. Antarct.*, volume I.

IPCC (2013a). *Climate Change 2013: The Physical Science Basis. Contribution of Working Group I to the Fifth Assessment Report of the Intergovernmental Panel on Climate Change*. Cambridge University Press, Cambridge, United Kingdom and New York, NY, USA.

IPCC (2013b). *Summary for policymakers*, pages 3–29. Cambridge University Press, Cambridge, UK.

IPCC (2019a). *IPCC Special Report on the Ocean and Cryosphere in a Changing Climate*. Cambridge University Press, Cambridge, United Kingdom and New York, NY, USA.

IPCC (2019b). *Technical Summary*. Cambridge University Press, Cambridge, UK.

Jenkins, A., Shoosmith, D., Dutrieux, P., Jacobs, S., Kim, T. W., Lee, S. H., Ha, H. K., and Stammerjohn, S. (2018). West Antarctic Ice Sheet retreat in the Amundsen Sea driven by decadal oceanic variability. *Nat. Geosci.*, 11(10):733–738.

Jitaru, P., Gabrielli, P., Marteel, A., Plane, J. M., Planchon, F. A., Gauchard, P. A., Ferrari, C. P., Boutron, C. F., Adams, F. C., Hong, S., Cescon, P., and Barbante, C. (2009). Atmospheric depletion of mercury over Antarctica during glacial periods. *Nat. Geosci.*, 2(7):505–508.

Johnsen, S. J., Dansgaard, W., Clausen, H. B., and Langway, C. C. (1972). Oxygen isotope profiles through the antarctic and greenland ice sheets. *Nature*, 235(5339):429–434.

Jouzel, J. (2013). A brief history of ice core science over the last 50 yr. *Clim. Past*, 9(6):2525–2547.

Jouzel, J., Masson-Delmotte, V., Cattani, O., Dreyfus, G., Falourd, S., Hoffmann, G., Minster, B., Nouet, J., Barnola, J. M., Chappellaz, J., Fischer, H., Gallet, J. C., Johnsen, S.,

Leuenberger, M., Loulergue, L., Luethi, D., Oerter, H., Parrenin, F., Raisbeck, G., Raynaud, D., Schilt, A., Schwander, J., Selmo, E., Souchez, R., Spahni, R., Stauffer, B., Steffensen, J. P., Stenni, B., Stocker, T. F., Tison, J. L., Werner, M., and Wolff, E. W. (2007). Orbital and millennial antarctic climate variability over the past 800,000 years. *Science (80-.).*, 317(5839):793–796.

Jouzel, J., Merlivat, L., and Lorius, C. (1982). Deuterium excess in an East Antarctic ice core suggests higher relative humidity at the oceanic surface during the last glacial maximum. *Nature*, 299(5885):688–691.

Kawamura, K., Abe-Ouchi, A., Motoyama, H., Ageta, Y., Aoki, S., Azuma, N., Fujii, Y., Fujita, K., Fujita, S., Fukui, K., Furukawa, T., Furusaki, A., Goto-Azuma, K., Greve, R., Hirabayashi, M., Hondoh, T., Hori, A., Horikawa, S., Horiuchi, K., Igarashi, M., Iizuka, Y., Kameda, T., Kanda, H., Kohno, M., Kuramoto, T., Matsushi, Y., Miyahara, M., Miyake, T., Miyamoto, A., Nagashima, Y., Nakayama, Y., Nakazawa, T., Nakazawa, F., Nishio, F., Obinata, I., Ohgaito, R., Oka, A., Okuno, J., Okuyama, J., Oyabu, I., Parrenin, F., Pattyn, F., Saito, F., Saito, T., Saito, T., Sakurai, T., Sasa, K., Seddik, H., Shibata, Y., Shinbori, K., Suzuki, K., Suzuki, T., Takahashi, A., Takahashi, K., Takahashi, S., Takata, M., Tanaka, Y., Uemura, R., Watanabe, G., Watanabe, O., Yamasaki, T., Yokoyama, K., Yoshimori, M., and Yoshimoto, T. (2017). State dependence of climatic instability over the past 720,000 years from Antarctic ice cores and climate modeling. *Sci. Adv.*, 3(2):1–14.

Koffman, B. G., Handley, M. J., Osterberg, E. C., Wells, M. L., and Kreutz, K. J. (2014a). Dependence of ice-core relative trace-element concentration on acidification. *J. Glaciol.*, 60(219):103–112.

Koffman, B. G., Kreutz, K. J., Breton, D. J., Kane, E. J., Winski, D. A., Birkel, S. D., and Kurbatov, A. V. (2014b). Centennial-scale variability of the Southern Hemisphere westerly wind belt in the eastern Pacific over the past two millennia. *Clim. Past*, pages 1125–1144.

Koyama, M. and Fujii, N. (1988). 2 Geophysical Research Station , Kyoto University , 3National Institute of Polar Research , ltabashi , Tokyo 173 (Japan) S Department of Chemistry , Faculty of Science , Kyoto University , Elsev ˜ r ˜ quo ˜ A ., L ˜ e. 124(1):235–249.

Lambert, F., Bigler, M., Steffensen, J. P., Hutterli, M., and Fischer, H. (2012). Centennial mineral dust variability in high-resolution ice core data from Dome C , Antarctica. *Clim. Past*, pages 609–623.

Lambert, F., Delmonte, B., Petit, J. R., Bigler, M., Kaufmann, P. R., Hutterli, M. A., Stocker, T. F., Ruth, U., Steffensen, J. P., and Maggi, V. (2008). Dust - Climate couplings over the past 800,000 years from the EPICA Dome C ice core. *Nature*, 452(7187):616–619.

Lee, J. E., Brook, E. J., Bertler, N. A. N., Buizert, C., Baisden, T., Blunier, T., Ciobanu, V. G., Conway, H., Dahl-jensen, D., Fudge, T. J., Hindmarsh, R., Keller, E. D., Parrenin, F., Severinghaus, J. P., Vallelonga, P., and Waddington, E. D. (2020). An 83 000-year-old ice core from Roosevelt Island, Ross Sea, Antarctica. *Cryosph.*, pages 1691–1713.

Legrand, M. R. and Delmas, R. J. (1988). Soluble Impurities in Four Antarctic Ice Cores Over the Last 30 000 Years. *Ann. Glaciol.*, 10(2):116–120.

Levy, R. H., Meyers, S. R., Naish, T. R., Golledge, N. R., McKay, Crampton, J., Deconto, R. M., Santis, L. D., Florindo, F., Gasson, E. G. W., Harwood, D. M., Luyendyk, B. P., Powell, R. D., Clowes, C., and K, K. D. (2019). Antarctic ice-sheet sensitivity to obliquity forcing enhanced through ocean connections. *Nat. Geosci.*, 12(February).

Liefferinge, B. V. and Pattyn, F. (2013). Using ice-flow models to evaluate potential sites of million year-old ice in Antarctica. *Clim. Past*, pages 2859–2887.

Lisiecki, L. E. and Raymo, M. E. (2005). A Pliocene-Pleistocene stack of 57 globally distributed benthic δ 18O records. *Paleoceanography*, 20(1):1–17.

Liu, Z., Tuo, S., Zhao, Q., Cheng, X., and Huang, W. (2004). Deep-water Earliest Oligocene Glacial Maximum (EOGM) in South Atlantic. *Chinese Sci. Bull.*, 49(20):2190–2197.

Long, D. T., Fegan, N. E., Mckee, J. D., Lyons, W. B., Hines, M. E., and Macumber, P. G. (1992). Formation of alunite, jarosite and hydrous iron oxides in a hypersaline system : Lake Tyrrell, Victoria, Australia. *Chem. Geol.*, 96:183–202.

MacFarling Meure, C., Etheridge, D., Trudinger, C., Steele, P., Langenfelds, R., Van Ommen, T., Smith, A., and Elkins, J. (2006). Law Dome CO2, CH4 and N2O ice core records extended to 2000 years BP. *Geophys. Res. Lett.*, 33(14):2000–2003.

Madden, M. E., Bodnar, R. J., and Rimstidt, J. D. (2004). Jarosite as an indicator of water-limited chemical weathering on Mars. *Nature*, 431(7010):821–823.

Maher, B. A., Prospero, J. M., Mackie, D., Gaiero, D., Hesse, P. P., and Balkanski, Y. (2010). Global connections between aeolian dust, climate and ocean biogeochemistry at the present day and at the last glacial maximum. *Earth-Science Rev.*, 99(1-2):61–97.

Mahowald, N. M., Muhs, D. R., Levis, S., Rasch, P. J., Yoshioka, M., Zender, C. S., and Luo, C. (2006). Change in atmospheric mineral aerosols in response to climate: Last glacial period, preindustrial, modern, and doubled carbon dioxide climates. *J. Geophys. Res.*, 111.

Marchant, D. R., Swisher, C. C., Lux, D. R., West, D. P., and Denton, G. H. (1993). Pliocene paleoclimate and East Antarctic ice-sheet history from surficial ash deposits. *Science (80-.).*, 260(5108):667–670.

Marzeion, B., Cogley, J. G., Richter, K., and Parkes, D. (2014). Glaciers. Attribution of global glacier mass loss to anthropogenic and natural causes. *Science*, 345(6199):919–921.

Masson-Delmotte, V., Hou, S., Ekaykin, A., Jouzel, J., Aristarain, A., Bernardo, R. T., Bromwich, D., Cattani, O., Delmotte, M. M., Falourd, S., Frezzotti, M., Gallée, H., Genoni, L., Isaksson, E., Landais, A., Helsen, M. M., Hoffmann, G., Lopez, J., Morgan, V., Motoyama, H., Noone, D., Oerter, H., Petit, J. R., Royer, A., Uemura, R., Schmidt, G. A., Schlosser, E., Simões, J. C., Steig, E. J., Stenni, B., Stievenard, M., Van Den Broeke, M. R.,

Van De Wal, R. S., Van De Berg, W. J., Vimeux, F., and White, J. W. (2008). A review of antarctic surface snow isotopic composition: Observations, atmospheric circulation, and isotopic modeling. *J. Clim.*, 21(13):3359–3387.

Medwedeff, W. G. and Roe, G. H. (2017). Trends and variability in the global dataset of glacier mass balance. *Clim. Dyn.*, 48(9-10):3085–3097.

Miller, K. G., Wright, J. D., Katz, M. E., Browning, J. V., Cramer, B. S., Wade, B. S., and Mizintseva, S. F. (2008). A View of Antarctic Ice-Sheet Evolution from Sea-Level and Deep-Sea Isotope Changes During the Late Cretaceous-Cenozoic. *Antarct. a keystone a Chang. world*, pages 55–70.

Montagnat, M., Buiron, D., Arnaud, L., Broquet, A., Schlitz, P., Jacob, R., and Kipfstuhl, S. (2012). Measurements and numerical simulation of fabric evolution along the Talos Dome ice core, Antarctica. *Earth Planet. Sci. Lett.*, 357-358:168–178.

Morgan, V., Li, J., Omme, T. D. V. A. N., Skinner, W., and Fitzpatrick, M. F. (1997). Site information and initial results from deep ice drilling on Law Dome, Antarctica. (143):3–10.

Mosher, B. W. and Duce, A. (1987). A global atmospheric Selenium budget. *J. Geophys. Res.*, 92(Dll).

Motoyama, H. (2007). The second deep ice coring project at Dome Fuji, Antarctica. *Sci. Drill.*, (5):41–43.

Mouginot, J., Rignot, E., and Scheuchl, B. (2014). Sustained increase in ice discharge from the Amundsen Sea Embayment, West Antarctic, from 1973 to 2013. *Geophys. Res. Lett.*, pages 1576–1584.

Mulvaney, R., Alemany, O., and Possenti, P. (2007). The Berkner Island (Antarctica) ice-core drilling project. *Ann. Glaciol.*, 47:115–124.

Neff, P. D. (2014). A review of the brittle ice zone in polar ice cores. *Ann. Glaciol.*, 55(68):72–82.

Nereson, N. A., Waddington, E. D., Raymond, C. F., and Jacobson, H. P. (1996). Predicted age-depth scales for Siple Dome and inland WAIS ice cores in west Antarctica. *Geophys. Res. Lett.*, 23(22):3163–3166.

Nriagu, J. O. (1989). A global assessment of natural sources of atmospheric trace metals. *Nature*, 338(6210):47–49.

Paleari, C. I., Delmonte, B., Andò, S., Garzanti, E., Petit, J. R., and Maggi, V. (2019). Aeolian Dust Provenance in Central East Antarctica During the Holocene : Environmental Constraints From Single - Grain Raman Spectroscopy. *Geophys. Res. Lett.*, 46(16):9968–9979.

Papike, J. J., Karner, J. M., and Shearer, C. K. (2006). Comparative planetary mineralogy : Implications of martian and terrestrial jarosite . A crystal chemical perspective. *Geochim. Cosmochim. Acta*, 70:1309–1321.

Parrenin, F., Jouzel, J., Waelbroeck, C., Ritz, C., and Barnola, J. M. (2001). Dating the Vostok ice core by an inverse method. *J. Geophys. Res. Atmos.*, 106(D23):31837–31851.

Petit, J. R., Briat, M., and Royer, A. (1981). Ice age aerosol content from East Antarctic ice core samples and past wind strength. *Nature*, 293(5831):391–394.

Petit, J. R., Raynaud, D., Basile, I., Chappellaz, J., Davisk, M., Ritz, C., Delmotte, M., Legrand, M., Lorius, C., Pe, L., and Saltzmank, E. (1999). Climate and atmospheric history of the past 420 , 000 years from the Vostok ice core , Antarctica. *Nature*, 399:429–436.

Petit, J. R., White, J. W. C., Young, N. W., Jouzel, J., and Korotkevich, Y. S. (1991). Deuterium Excess in Recent Antarctic Snow. *J. Geophys. Res.*, 96:5113–5122.

Pol, K., Masson-Delmotte, V., Johnsen, S., Bigler, M., Cattani, O., Durand, G., Falourd, S., Jouzel, J., Minster, B., Parrenin, F., Ritz, C., Steen-Larsen, H. C., and Stenni, B. (2010). New MIS 19 EPICA Dome C high resolution deuterium data: Hints for a problematic preservation of climate variability at sub-millennial scale in the "oldest ice". *Earth Planet. Sci. Lett.*, 298(1-2):95–103.

Pollard, D. and Deconto, R. M. (2020). Continuous simulations over the last 40 million years with a coupled Antarctic ice sheet-sediment model. *Palaeogeogr. Palaeoclimatol. Palaeoecol.*, 537(September 2019):109374.

Railsback, L. B., Gibbard, P. L., Head, M. J., Voarintsoa, N. R. G., and Toucanne, S. (2015). An optimized scheme of lettered marine isotope substages for the last 1.0 million years, and the climatostratigraphic nature of isotope stages and substages. *Quat. Sci. Rev.*, 111(March 2015):94–106.

Rauter, R. and Stauffer, B. (1977). Determination of impurities in ice cores from the Jungfrau-Joch by neutron activation analysis. *J. Radioanal. Chem.*, 38:405–413.

Revel-rolland, M., Deckker, P. D., Delmonte, B., and Hesse, P. P. (2006). Eastern Australia : A possible source of dust in East Antarctica interglacial ice. *Earth Planet. Sci. Lett.*, 249:1–13.

Rhodes, R. H., Baker, J. A., Millet, M.-a., and Bertler, N. A. N. (2011). Experimental investigation of the effects of mineral dust on the reproducibility and accuracy of ice core trace element analyses. *Chem. Geol.*, 286(3-4):207–221.

Rignot, E., Mouginot, J., Morlighem, M., Seroussi, H., and Scheuchl, B. (2014). Widespread, rapid grounding line retreat of Pine Island, Thwaites, Smith, and Kohler glaciers, West Antarctica, from 1992 to 2011. pages 3502–3509.

Rignot, E., Mouginot, J., and Scheuchl, B. (2011). Ice Flow of the Antarctic Ice Sheet. *Science (80-.).*, 333(September):1427–1431.

Rignot, E., Mouginot, J., Scheuchl, B., Van Den Broeke, M., Van Wessem, M. J., and Morlighem, M. (2019). Four decades of Antarctic ice sheet mass balance from 1979–2017. *Proc. Natl. Acad. Sci. U. S. A.*, 116(4):1095–1103.

Rothlisberger, R., Mulvaney, R., Wolff, E. W., Hutterli, M. A., Bigler, M., Sommer, S., and Jouzel, J. (2003). Dust and sea salt variability in central East Antarctica (Dome C) over the last 45 kyrs and its implications for southern high-latitude climate. *Geophys. Res. Lett.*, 29(20):1–4.

Salvini, A., Clemenza, M., Previtali, E., Borio di Tigliole, A., Cagnazzo, M., and Manera, S. (2006). Determination of Th , U and K contamination in materials used in a low background detector by nuclear measures. *J. Phys. Conf. Ser. 41 046*.

Scarchilli, C., Frezzotti, M., and Ruti, P. M. (2011). Snow precipitation at four ice core sites in East Antarctica: Provenance, seasonality and blocking factors. *Clim. Dyn.*, 37(9-10):2107–2125.

Schroeder, W. H. and Munthe, J. (1998). Atmospheric mercury - An overview. *Atmos. Environ.*, 32(5):809–822.

Shepherd, A., Gilbert, L., Muir, A. S., Konrad, H., Mcmillan, M., Slater, T., Briggs, K. H., and Sundal, A. V. (2019). Trends in Antarctic Ice Sheet Elevation and Mass. *Geophys. Res. Lett.*, 46:8174–8183.

Siggaard-Andersen, M.-l., Gabrielli, P., and Peder, J. (2007). Soluble and insoluble lithium dust in the EPICA DomeC ice core — Implications for changes of the East Antarctic dust provenance during the recent glacial – interglacial transition. 258:32–43.

Slater, T., Lawrence, I. R., Otosaka, I. N., Shepherd, A., Gourmelen, N., Jakob, L., Tepes, P., Gilbert, L., and Nienow, P. (2021). Earth's ice imbalance. *Cryosph.*, 15.1:233–246.

Sommerfeld, R. and LaChapelle, E. (1970). The classification of snow metamorphism. *J. Glaciol.*, 5(6):225–226.

Spolaor, A., Vallelonga, P., Cozzi, G., Gabrieli, J., Varin, C., Kehrwald, N., Zennaro, P., Boutron, C., and Barbante, C. (2013). Iron speciation in aerosol dust influences iron bioavailability over glacial-interglacial timescales. *Geophys. Res. Lett.*, 40(8):1618–1623.

Steig, E. J., Brook, E. J., White, J. W., Sucher, C. M., Bender, M. L., Lehman, S. J., Morse, D. L., Waddington, E. D., and Clow, G. D. (1998). Synchronous climate changes in Antarctica and the North Atlantic. *Science (80-.).*, 282(5386):92–95.

Stenni, B., Buiron, D., Frezzotti, M., Albani, S., Barbante, C., Bard, E., Barnola, J. M., Baroni, M., Baumgartner, M., Bonazza, M., Capron, E., Castellano, E., Chappellaz, J., Delmonte, B., Falourd, S., Genoni, L., Iacumin, P., Jouzel, J., Kipfstuhl, S., Landais, A., Lemieux-Dudon, B., Maggi, V., Masson-Delmotte, V., Mazzola, C., Minster, B., Montagnat, M., Mulvaney, R., Narcisi, B., Oerter, H., Parrenin, F., Petit, J. R., Ritz, C., Scarchilli, C., Schilt, A., Schüpbach, S., Schwander, J., Selmo, E., Severi, M., Stocker, T. F., and Udisti, R. (2011). Expression of the bipolar see-saw in Antarctic climate records during the last deglaciation. *Nat. Geosci.*, 4(1):46–49.

Stockli, R., Vermote, E., Saleous, N., Simmon, R., and Herring, D. (2005). The Blue Marble Next Generation - A true color earth dataset including seasonal dynamics from MODIS. *NASA Earth Obs.*, 43200:3–5.

Sugden, D. E., Bentley, M. J., and Cofaigh, C. Ó. (2006). Geological and geomorphological insights into Antarctic ice sheet evolution. *Philos. Trans. R. Soc. A Math. Phys. Eng. Sci.*, 364(1844):1607–1625.

Taylor, K. C., Alley, R. B., Meese, D. A., Spencer, M. K., Brook, E. J., Dunbar, N. W., Finkel, R. C., Gow, A. J., Kurbatov, A. V., Lamorey, G. W., Mayewski, P. A., Meyerson, E. A., Nishiizumi, K., and Zielisnki, G. A. (2004). Dating the Siple Dome (Antarctica) ice core by manual and computer interpretation of annual layering. *J. Glaciol.*, 50(170):453–461.

Tegen, I. (2003). Modeling the mineral dust aerosol cycle in the climate system. *Quat. Sci. Rev.*, 22:1821–1834.

Tison, J. L., De Angelis, M., Littot, G., Wolff, E., Fischer, H., Hansson, M., Bigler, M., Udisti, R., Wegner, A., Jouzel, J., Stenni, B., Johnsen, S., Masson-Delmotte, V., Landais, A., Lipenkov, V., Loulergue, L., Barnola, J. M., Petit, J. R., Delmonte, B., Dreyfus, G., Dahl-Jensen, D., Durand, G., Bereiter, B., Schilt, A., Spahni, R., Pol, K., Lorrain, R., Souchez, R., and Samyn, D. (2015). Retrieving the paleoclimatic signal from the deeper part of the EPICA Dome C ice core. *Cryosphere*, 9(4):1633–1648.

Twining, B. S., Baines, S. B., Vogt, S., and Nelson, D. M. (2012). Role of diatoms in nickel biogeochemistry in the ocean. *Global Biogeochem. Cycles*, 26(4):1–9.

Uglietti, C., Gabrielli, P., Olesik, J. W., Lutton, A., and Thompson, L. G. (2014). Large variability of trace element mass fractions determined by ICP-SFMS in ice core samples from worldwide high altitude glaciers. *Appl. Geochemistry*, 47:109–121.

Vallelonga, P., Gabrielli, P., Balliana, E., Wegner, A., Delmonte, B., Turetta, C., Burton, G., Vanhaecke, F., Rosman, K. J. R., Hong, S., Boutron, C. F., Cescon, P., and Barbante, C. (2010). Lead isotopic compositions in the EPICA Dome C ice core and Southern Hemisphere Potential Source Areas q. *Quat. Sci. Rev.*, 29(1-2):247–255.

Vallelonga, P. and Svensson, A. (2014). Ice core archives of mineral dust. In *Miner. Dust*, pages 463–485.

Vallelonga, P., Velde, K. V. D., Candelone, J., Morgan, V. I., Boutron, C. F., and Rosman, K. J. R. (2002). The lead pollution history of Law Dome , Antarctica , from isotopic measurements on ice cores : 1500 AD to 1989 AD. *Earth Planet. Sci. Lett.*, 204.

Van Liefferinge, B., Pattyn, F., Cavitte, M. G. P., Karlsson, N. B., Young, D. A., Sutter, J., and Eisen, O. (2018). Promising Oldest Ice sites in East Antarctica based on thermodynamical modelling. *Cryosph. Discuss.*, (February):1–22.

Veres, D., Bazin, L., Landais, A., Toyé Mahamadou Kele, H., Lemieux-Dudon, B., Parrenin, F., Martinerie, P., Blayo, E., Blunier, T., Capron, E., Chappellaz, J., Rasmussen, S. O., Severi, M., Svensson, A., Vinther, B., and Wolff, E. W. (2013). The Antarctic ice core chronology (AICC2012): An optimized multi-parameter and multi-site dating approach for the last 120 thousand years. *Clim. Past*, 9(4):1733–1748.

Vlastelic, I., Suchorski, K., Sellegri, K., Colomb, A., Nauret, F., Bouvier, L., and Piro, J.-L. (2015). The high field strength element budget of atmospheric aerosols (puy de Dome, France). *Geochim. Cosmochim. Acta*, 167:253–268.

Wagenbach, D. and Geis, K. (1989). The mineral dust record in a high altitude Alpine glacier (Colle Gnifetti, Swiss Alps). In *Paleoclimatology Paleometeorology Mod. Past Patterns Glob. Atmos. Transp. NATO ASI Ser. (Series C Math. Phys. Sci.* Springer, Dordrecht, paleoclima edition.

Watanabe, O., Jouzel, J., Johnsen, S., Parrenin, F., Shoji, H., and Yoshida, N. (2003). Homogeneous climate variability across East Antarctica over the past three glacial cycles. *Nature*, 422(6931):509–512.

Wedepohl, K. H. (1995). The composition of the continental crust. *Geochim. Cosmochim. Acta*, 59(7):1217–1232.

Wegner, A., Fischer, H., Delmonte, B., Petit, J., Erhardt, T., Ruth, U., Svensson, A., Vinther, B., and Miller, H. (2015). The role of seasonality of mineral dust concentration and sizeon glacial/interglacial dust changes in the EPICA DronningMaud Land ice core. *J. Geophys. Res.*, 120(19):9916–9931.

Wegner, A., Gabrielli, P., Ruth, U., Kriews, M., Deckker, P. D., Barbante, C., and Cozzi, G. (2012). Change in dust variability in the Atlantic sector of Antarctica at the end of the last deglaciation. *Clim. Past*, pages 135–147.

Wen, H. and Carignan, J. (2007). Reviews on atmospheric selenium: Emissions, speciation and fate. *Atmos. Environ.*, 41(34):7151–7165.

Winton, V. H. L., Edwards, R., Delmonte, B., Ellis, A., Andersson, P. S., Bowie, A., Bertler, N. A. N., Neff, P., and Tuohy, A. (2016). Multiple sources of soluble atmospheric iron to Antarctic waters. *Global Biogeochem. Cycles*, pages 421–437.

Zachos, J., Pagani, H., Sloan, L., Thomas, E., and Billups, K. (2001). Trends, rhythms, and aberrations in global climate 65 Ma to present. *Science (80-.).*, 292(5517):686–693.

Zachos, J. C., Dickens, G. R., and Zeebe, R. E. (2008). An early Cenozoic perspective on greenhouse warming and carbon-cycle dynamics. *Nature*, 451(7176):279–283.

Zachos, J. C., Quinn, T. M., and Salamy, K. A. (1996). High-resolution deap-sea foraminiferal stable isotope records of the Eocene-Oligocene transition. *Paleoceanography*, 11(3):251–266.

Zemp, M., Frey, H., Gärtner-Roer, I., Nussbaumer, S. U., Hoelzle, M., Paul, F., Haeberli, W., Denzinger, F., Ahlstrøm, A. P., Anderson, B., Bajracharya, S., Baroni, C., Braun, L. N., Càceres, B. E., Casassa, G., Cobos, G., Dàvila, L. R., Delgado Granados, H., Demuth, M. N., Espizua, L., Fischer, A., Fujita, K., Gadek, B., Ghazanfar, A., Hagen, J. O., Holmlund, P., Karimi, N., Li, Z., Pelto, M., Pitte, P., Popovnin, V. V., Portocarrero, C. A., Prinz, R., Sangewar, C. V., Severskiy, I., Sigurdsson, O., Soruco, A., Usubaliev, R., and Vincent, C. (2015). Historically unprecedented global glacier decline in the early 21st century. *J. Glaciol.*, 61(228):745–762.

Zolotov, M. Y. and Mironenko, M. V. (2007). Timing of acid weathering on Mars: A kinetic-thermodynamic assessment. *J. Geophys. Res. E Planets*, 112(7).

Appendix A
Concentration values for INAA and ICP-SFMS measurements

Table 1 and 2 report concentration values, expressed in ng/g, for INAA data.

Table 3 and 4 report concentration values, expressed in ng/g, for untreated ICP-SFMS data.

Table 5 and 6 report concentration values, expressed in ng/g, for filtered ICP.SFMS data.

Table 1: INAA data. Concentration values expressed in ng/g. Values in blue are Detection Limits.

Sample	Depth (m)	Al	As	Ba	Ca	Ce	Co	Cr	Cs	Eu	Fe	Hf	Hg	Ho	K	La	Lu	Mn
T1	439-529	3360	0.69	92.05	2353	5.39	1.00	2.12	0.27	0.09	3741	0.57	0.13	0.04	1222	2.45	0.035	56
T2	531-649	2746	0.36	55.84	1562	2.86	0.64	1.92	0.17	0.05	2210	0.34	0.11	0.02	639	1.59	0.024	25
T3	669-798	2722	0.57	45.54	2289	4.15	0.83	4.28	0.22	0.10	3511	0.41	0.41	0.05	820	2.21	0.019	77
T4	802-813	13581	2.25	108.88	3028	16.91	3.26	6.15	1.06	0.36	12943	1.60	0.27	0.34	3398	7.42	0.086	122
T5	816-903	18010	2.99	109.17	3677	18.64	4.64	12.42	1.98	0.39	15611	1.41	0.83	0.39	4614	8.01	0.083	178
T6	906-931	22210	3.15	171.45	3235	25.91	4.89	5.69	2.18	0.48	17184	1.66	0.27	0.42	5322	11.18	0.101	190
T7	939-957	16953	3.18	158.98	2870	16.68	4.07	12.60	2.10	0.37	14356	1.48	0.55	0.30	5072	7.51	0.083	134
T8	1067-1199	4529	1.28	55.84	2058	4.29	0.85	3.06	0.63	0.11	3932	0.50	0.18	0.03	1444	1.99	0.034	34
T9	1210-1255	7576	1.06	55.78	2791	6.14	1.42	28.08	0.53	0.16	5917	1.20	0.10	0.04	1442	2.84	0.042	78
T10	1259-1298	15601	3.29	120.05	2892	10.86	2.23	75.71	1.56	0.22	11055	4.56	0.31	0.18	3344	4.92	0.037	117
T11	1423-1441	13752	2.84	75.12	6715	24.33	2.92	10.71	1.30	0.44	13401	2.14	0.78	0.42	5509	11.82	0.116	148
T12	1445-1477	9999	2.02	68.45	2523	10.60	0.91	2.66	0.85	0.14	6511	1.04	0.33	0.25	2942	5.87	0.096	77
T13	1489-1512	10537	2.00		2889	34.25	2.19	0.85	1.67	0.25	11239	3.70			5452	16.65	0.192	146
T14	1513-1530	6734	1.27		2765	11.03	1.98	1.10	0.76	0.19	6700	0.92			2876	5.96	0.053	64
T15	1535-1552	5665	1.17		2100	10.50	1.97	2.89	0.65	0.19	7021	1.02			2605	5.68	0.296	44
T16	1560-1689	5662	1.04		5442	9.83	2.69	144.02	0.28	0.23	9981	0.74			1269	4.36	0.025	99

Table 2: INAA data. Concentration values expressed in ng/g. Values in blue are Detection Limits.

Sample	Depth (m)	Na	Nd	Ni	Rb	Sb	Sc	Se	Si	Sm	Sr	Ta	Tb	Th	Ti	Tm	U	V	Yb	Zn
T1	439-529	1371	1.77	3.70	6.21	0.05	0.93	0.074	21562	0.40	56.34	0.34	0.06	0.82	279	0.03	0.11	7	0.18	10.51
T2	531-649	528	1.01	3.70	3.06	0.05	0.60	0.076	13351	0.23	30.49	0.16	0.03	0.45	204	0.02	0.14	5	0.10	6.35
T3	669-798	692	2.93	3.01	4.27	0.20	0.86	0.284	13922	0.29	35.73	0.25	0.04	0.72	649	0.02	0.58	7	0.14	33.20
T4	802-813	3190	8.78	7.27	18.18	0.25	3.54	0.707	73493	1.23	156.81	0.83	0.18	2.81	1811	0.12	0.41	24	1.72	24.43
T5	816-903	3878	7.05	7.27	22.11	0.25	4.71	0.984	82332	1.49	150.28	0.55	0.17	2.81	2468	0.12	0.57	32	1.50	114.58
T6	906-931	4263	11.34	9.38	29.81	0.25	5.57	0.544	50625	1.96	222.53	0.66	0.17	3.30	2284	0.03	0.75	36	2.01	79.16
T7	939-957	3265	7.11	8.97	26.50	0.92	5.05	1.027	82995	1.36	124.59	0.60	0.19	3.31	1797	0.04	0.66	31	1.50	146.83
T8	1067-1199	1093	1.42	4.40	7.27	0.15	0.70	0.357	30269	0.34	54.23	0.14	0.04	0.98	311	0.03	0.14	9	0.20	21.48
T9	1210-1255	984	2.19	3.25	8.94	0.17	1.45	0.173	25874	0.38	55.55	0.44	0.06	1.26	1116	0.04	0.34	14	0.38	10.63
T10	1259-1298	2287	0.47	4.19	24.52	0.27	3.46	0.359	30218	0.72	89.07	0.43	0.12	2.52	1486	0.07	0.56	30	0.52	20.28
T11	1423-1441	4430	8.37	3.01	23.14	0.21	3.86	1.692	51125	2.03	128.41	0.99	0.26	3.52	1548	0.14	2.76	26	0.95	41.39
T12	1445-1477	1677	6.10	3.01	15.04	0.12	1.87	1.033	28045	0.82	56.99	0.51	0.11	2.39	639	0.04	0.58	13	0.49	9.28
T13	1489-1512	4506	8.18	187.13	44.10	0.11	1.85		67340	2.21	76.42	2.54	0.39	6.81	1104		1.48	12	1.15	
T14	1513-1530	1352	4.45	19.58	2.93	0.11	1.69		42064	0.70	70.56	0.57	0.12	1.70	836		0.41	13	0.33	
T15	1535-1552	1109	12.65	19.54	11.42	0.11	1.53		41976	0.71	70.42	0.10	0.12	1.97	872		0.38	12	0.34	
T16	1560-1689	1325	4.45	15.17	2.27	0.18	1.97		32590	0.69	54.67	0.56	0.10	0.92	1418		0.38	18	0.30	

Table 3: Untreated ICP-SFMS data. Concentration values expressed in ng/g. Values in blue are Detection Limits.

Sample	Depth (m)	Ag	As	Bi	Cd	Ce	Co	Cs	Cu	Dy	Er	Eu	Fe	Ga	Gd	Ho	La	Li	Lu	Mg
TD-0209	209.00	0.52	1.22	0.37	12.56	8.00	1.04	1.30	10.37	0.48	0.22	0.27	1056	2.11	0.67	0.09	4.44	185	0.02	2340
TD-0262	261.75	0.62	2.34	0.08	30.64	1.44	0.91	1.21	44.31	0.11	0.07	0.12	1036	2.19	0.13	0.02	0.97	165	0.01	2439
TD-0383	383.00	0.44	1.78	0.22	6.84	8.08	1.70	1.56	28.48	0.38	0.23	0.22	1193	2.35	0.58	0.08	5.29	175	0.03	3673
TD-0398	398.00	0.47	1.55	0.11	5.83	6.20	1.36	1.37	22.29	0.58	0.45	0.26	2365	2.44	0.63	0.12	3.58	145	0.06	2915
TD-0438	438.00	0.49	1.50	0.10	20.20	16.31	2.43	1.45	15.79	0.81	0.45	0.45	3740	2.70	1.19	0.16	9.51	149	0.06	22353
TD-0849	848.25	0.62	6.55	0.32	55.02	88.69	9.48	4.10	14.01	4.93	2.51	1.94	19673	9.67	6.74	1.08	93.74	145	0.29	16757
TD-0893	892.25	0.52	5.72	0.74	236.10	84.13	8.33	4.46	23.28	4.60	2.35	1.84	19240	9.01	6.05	0.87	45.84	159	0.27	10216
TD-0950	949.25	0.59	5.22	0.30	19.79	40.27	4.83	3.56	8.39	2.39	1.21	1.01	10501	18.42	3.31	0.47	21.59	169	0.15	10690
TD-1030	1030.00	0.45	4.28	0.25	61.06	23.17	4.05	2.99	11.47	1.49	0.79	0.68	7002	8.67	2.10	0.29	12.18	227	0.09	7688
TD-1186	1186.00	0.52	4.05	0.20	22.26	36.00	3.66	2.78	8.36	1.57	0.83	0.64	6315	4.16	2.21	0.32	13.75	187	0.10	8576
TD-1249	1249.00	0.60	3.94	0.34	103.40	16.37	8.49	1.77	28.32	0.97	0.55	0.47	9690	4.81	1.35	0.19	8.79	312	0.06	10709
TD-1269	1269.00	0.61	4.33	0.27	9.53	49.43	6.83	2.50	11.53	2.84	1.46	1.19	11164	7.65	3.72	0.55	29.48	292	0.19	10743
TD-1303	1303.00	0.72	3.00	0.37	95.40	15.17	2.86	1.88	24.29	0.98	0.49	0.37	4551	4.05	1.22	0.19	8.46	176	0.06	5848
TD-1313	1312.50	0.56	2.94	0.23	8.05	12.58	2.44	2.10	24.09	0.94	0.51	0.36	3256	3.08	1.24	0.18	6.38	277	0.06	4716
TD-1391	1390.50	0.54	3.55	0.20	99.49	12.29	1.78	5.29	17.31	0.67	0.46	0.37	3068	40.82	0.83	0.14	8.74	263	0.07	3659
TD-1397	1396.50	0.60	2.50	0.13	17.05	85.22	21.76	1.57	17.31	6.45	3.32	3.44	48593	15.60	8.46	1.26	47.22	249	0.37	16340
TD-1492	1492.50	0.53	3.78	1.03	6.21	48.42	3.18	2.15	28.24	2.42	1.29	0.85	11326	6.73	3.15	0.47	28.59	545	0.17	6362
TD-1496	1495.25	0.52	2.44	0.19	37.19	11.20	2.49	1.49	38.39	0.64	0.36	0.29	3871	3.84	0.98	0.13	6.72	217	0.05	5419
TD-1524	1523.50	0.54	1.78	0.15	131.51	4.78	1.93	1.17	67.20	0.26	0.13	0.19	1313	3.58	0.33	0.05	2.44	258	0.02	2797
TD-1544	1543.50	0.54	2.22	0.18	5.34	26.95	3.89	1.73	46.56	1.51	0.82	0.77	8437	4.69	1.91	0.30	16.20	223	0.11	24966
TD-1558	1557.55	0.72	11.88	0.74	11.06	544.36	9.85	6.98	10.64	22.58	12.96	3.88	49364	28.44	26.50	4.56	348.55	229	1.77	11683
TD-1571	1570.50	0.47	2.28	0.11	9.87	52.00	3.12	1.56	20.29	2.03	1.03	1.18	6024	6.25	2.82	0.38	32.72	183	0.13	5167
TD-1616	1615.75	0.47	2.28	0.19	191.91	29.57	2.88	2.30	37.49	1.22	0.64	0.74	6552	5.55	1.77	0.24	18.54	153	0.08	5786

Table 4: Untreated ICP-SFMS data. Concentration values expressed in ng/g. Values in blue are Detection Limits.

Sample	Depth (m)	Mn	Mo	Na	Nb	Nd	Ni	Pb	Pr	Rb	Sm	Sn	Sr	Ta	Tb	Ti	Tl	Tm	V	Yb
TD-0209	209.00	45	0.82	17848	1.46	3.68	201	5.09	1.04	35	1.06	3.11	106	0.201	0.10	109	0.730	0.03	3.95	0.16
TD-0262	261.75	19	0.58	25448	0.50	0.65	185	1.95	0.17	38	0.30	2.65	86	0.201	0.02	111	0.097	0.01	5.58	0.06
TD-0383	383.00	46	2.41	24259	0.98	3.11	176	4.99	0.98	39	0.94	2.09	97	0.201	0.09	241	0.175	0.03	6.08	0.18
TD-0398	398.00	51	0.98	18252	1.17	2.66	181	3.21	0.78	29	0.85	2.19	85	0.364	0.10	238	0.179	0.07	6.48	0.41
TD-0438	438.00	94	1.23	185534	3.61	6.45	181	12.91	1.93	77	1.56	2.61	268	0.345	0.17	776	0.128	0.07	9.93	0.35
TD-0849	848.25	495	1.26	64723	11.13	36.45	177	10.06	10.82	54	8.71	3.23	299	0.497	0.95	2184	0.347	0.35	39.36	2.08
TD-0893	892.25	408	1.60	48569	11.18	35.53	163	8.10	10.21	47	8.00	3.24	287	0.469	0.86	2046	0.249	0.31	41.27	1.99
TD-0950	949.25	264	1.36	60463	2.88	17.55	166	8.79	4.99	44	4.51	2.50	255	0.216	0.46	779	0.239	0.17	22.96	1.00
TD-1030	1030.00	165	0.95	51044	1.60	10.23	156	7.20	2.93	39	2.78	2.42	145	0.221	0.28	520	0.256	0.11	15.14	0.63
TD-1186	1186.00	192	3.27	40992	5.24	11.00	167	5.37	3.19	45	2.80	2.11	194	0.201	0.31	502	0.228	0.12	14.01	0.66
TD-1249	1249.00	161	1.40	44701	1.96	6.86	373	6.98	2.01	61	1.83	3.68	115	0.282	0.19	469	0.399	0.08	23.53	0.45
TD-1269	1269.00	329	1.23	43362	6.64	21.10	257	11.56	6.18	51	4.97	3.34	171	0.371	0.53	1368	0.324	0.20	29.04	1.27
TD-1303	1303.00	86	0.92	85618	1.11	6.27	248	10.50	1.84	33	1.57	4.58	83	0.249	0.18	286	0.319	0.07	13.24	0.39
TD-1313	1312.50	90	0.86	26702	1.28	5.95	259	9.31	1.61	38	1.62	2.88	70	0.208	0.18	279	0.268	0.07	8.71	0.44
TD-1391	1390.50	99	1.34	23575	1.65	4.72	227	5.27	1.46	34	1.59	2.98	272	0.201	0.12	344	0.129	0.07	8.84	0.47
TD-1397	1396.50	795	1.65	32418	23.48	40.72	247	4.24	11.11	39	10.35	3.80	377	0.723	1.22	10795	0.154	0.43	148.60	2.51
TD-1492	1492.50	191	1.82	41271	3.74	19.50	230	17.41	5.86	39	4.39	3.37	108	0.207	0.47	637	0.841	0.19	15.39	1.10
TD-1496	1495.25	131	1.06	30465	0.65	4.67	222	6.16	1.36	30	1.26	2.80	93	0.201	0.13	333	0.282	0.06	15.43	0.29
TD-1524	1523.50	78	1.75	20250	0.51	1.85	237	8.19	0.51	23	0.59	2.99	76	0.201	0.05	230	0.125	0.02	12.55	0.12
TD-1544	1543.50	324	1.84	183454	5.03	10.87	216	16.78	3.28	45	2.44	2.68	182	0.268	0.28	983	0.167	0.11	24.66	0.73
TD-1558	1557.55	896	11.87	62952	94.56	168.64	200	33.23	55.71	119	34.15	7.99	409	0.920	4.08	2121	0.983	1.86	55.96	12.13
TD-1571	1570.50	168	2.44	34863	2.91	19.61	203	7.45	5.97	28	4.23	3.33	200	0.201	0.39	628	0.120	0.14	8.42	0.88
TD-1616	1615.75	134	1.18	35118	2.18	11.26	178	6.90	3.44	31	2.56	3.00	146	0.247	0.25	470	0.118	0.09	10.91	0.60

Table 5: Filtered ICP-SFMS data. Concentration values expressed in ng/g. Values in blue are Detection Limits.

Sample	Depth (m)	Ag	As	Bi	Cd	Ce	Co	Cs	Cu	Dy	Er	Eu	Fe	Ga	Gd	Ho	La	Li	Lu
TD-0209	209.00	0.55	1.05	0.15	1.70	0.762	0.71	1.04	19.72	0.046	0.020	0.098	1036	1.74	0.081	0.006	0.495	173	0.005
TD-0262	261.75	0.60	0.84	0.20	2.91	1.179	0.98	2.00	7.35	0.060	0.042	0.103	1036	1.72	0.129	0.016	0.688	165	0.009
TD-0383	383.00	0.50	1.34	0.17	2.20	2.031	0.62	0.79	8.20	0.080	0.056	0.098	1036	2.28	0.169	0.017	1.167	144	0.010
TD-0398	398.00	0.49	1.34	0.33	2.87	0.520	0.72	0.97	13.16	0.055	0.028	0.082	1036	1.42	0.078	0.008	0.356	166	0.006
TD-0438	438.00	1.09	1.11	0.20	13.93	0.490	1.31	1.20	18.64	0.041	0.028	0.094	1036	2.03	0.095	0.008	0.375	145	0.006
TD-0849	848.25	0.47	1.44	0.16	0.48	0.624	0.55	0.97	24.20	0.073	0.027	0.094	1036	2.83	0.070	0.008	0.426	147	0.006
TD-0950	949.25	0.50	0.61	0.19	0.86	0.799	0.90	0.94	20.51	0.048	0.025	0.106	1036	1.73	0.081	0.008	0.388	144	0.007
TD-1030	1030.00	0.63	0.78	0.08	0.62	7.850	0.66	0.77	13.85	0.044	0.035	0.091	1036	1.42	0.080	0.008	0.521	196	0.006
TD-1186	1186.00	0.48	1.05	0.10	1.78	0.301	1.30	1.50	11.79	0.023	0.016	0.083	9103	1.08	0.065	0.003	0.172	170	0.005
TD-1249	1249.00	0.68	1.44	0.19	53.20	1.354	1.09	1.77	21.53	0.036	0.018	0.080	1036	4.01	0.080	0.006	0.400	310	0.006
TD-1269	1269.00	0.54	0.89	0.17	2.81	0.604	1.61	1.46	16.74	0.038	0.021	0.087	1036	2.59	0.065	0.006	0.327	250	0.007
TD-1303	1303.00	0.63	0.84	0.11	3.06	0.899	1.14	4.50	69.03	0.148	0.072	0.107	1036	2.63	0.187	0.025	0.298	162	0.011
TD-1313	1312.50	0.58	1.34	0.24	8.11	1.091	1.53	1.06	54.66	0.060	0.146	0.100	1036	2.75	0.108	0.015	0.595	238	0.010
TD-1391	1390.50	0.54	0.72	0.18	0.80	2.392	1.49	1.28	22.10	0.093	0.053	0.116	1036	3.37	0.119	0.017	0.668	238	0.009
TD-1397	1396.50	0.60	0.42	0.25	3.50	0.876	1.01	1.05	47.70	0.090	0.062	0.131	1036	2.87	0.151	0.019	0.543	231	0.010
TD-1492	1492.50	0.62	2.05	0.21	0.41	2.337	1.73	1.54	39.71	0.134	0.071	0.102	1036	3.19	0.176	0.022	1.021	506	0.013
TD-1544	1543.50	0.49	1.28	0.15	6.07	6.860	2.93	2.08	48.16	0.491	0.287	0.285	1036	2.20	0.742	0.102	3.004	203	0.038
TD-1558	1557.55	0.57	1.11	0.10	0.36	0.745	0.80	1.30	57.32	0.076	0.092	0.112	1036	1.67	0.125	0.015	0.690	203	0.010
TD-1571	1570.50	0.51	1.11	0.06	1.56	0.366	1.09	1.86	106.86	0.067	0.037	0.117	1036	1.87	0.115	0.012	0.264	172	0.008
TD-1616	1615.75	0.45	0.55	0.26	1.49	1.985	0.90	0.89	59.97	0.102	0.054	0.099	1446	2.20	0.129	0.015	0.697	158	0.011

Table 6: Filtered ICP-SFMS data. Concentration values expressed in ng/g. Values in blue are Detection Limits.

Sample	Depth (m)	Mg	Mn	Na	Ni	Pb	Pr	Rb	Sm	Sn	Sr	Ta	Tb	Ti	Tl	Tm	V	Yb
TD-0209	209.00	1886	16	16450	192	1.52	0.085	26	0.215	3.84	78	0.201	0.014	97	0.120	0.008	3.95	0.027
TD-0262	261.75	1555	21	119765	191	5.80	0.103	33	0.242	3.29	94	0.202	0.021	236	0.072	0.011	3.95	0.034
TD-0383	383.00	1718	19	25530	163	6.66	0.240	16	0.327	3.51	43	0.405	0.026	122	0.072	0.013	3.95	0.045
TD-0398	398.00	2947	22	24550	176	1.27	0.053	32	0.219	5.25	80	0.214	0.015	105	0.072	0.009	3.95	0.032
TD-0438	438.00	2516	38	197015	192	1.45	0.052	59	0.231	3.77	92	0.201	0.015	132	0.081	0.010	3.95	0.038
TD-0849	848.25	1254	16	50090	154	9.63	0.072	18	0.231	3.29	74	0.201	0.017	97	0.072	0.010	3.95	0.035
TD-0950	949.25	1259	17	52064	162	1.24	0.067	22	0.280	2.88	73	0.207	0.019	97	0.072	0.009	6.83	0.027
TD-1030	1030.00	2085	15	46815	166	0.95	0.071	18	0.188	4.71	78	0.203	0.015	109	0.072	0.009	5.71	0.063
TD-1186	1186.00	2996	117	30828	171	1.32	0.030	21	0.204	2.64	80	0.201	0.014	471	0.072	0.008	4.11	0.027
TD-1249	1249.00	1905	22	50606	303	2.32	0.056	48	0.224	4.73	48	0.270	0.013	142	0.072	0.008	7.84	0.028
TD-1269	1269.00	2773	42	42632	268	1.70	0.052	29	0.209	16.00	57	0.531	0.012	188	0.072	0.008	3.95	0.029
TD-1303	1303.00	2273	23	70915	251	3.17	0.109	21	0.391	3.87	40	0.245	0.031	158	0.072	0.015	3.95	0.081
TD-1313	1312.50	1666	24	29097	259	1.94	0.088	26	0.277	3.53	48	0.204	0.020	140	0.072	0.013	3.95	0.041
TD-1391	1390.50	1700	16	27121	232	2.26	0.142	24	0.277	3.45	66	0.378	0.021	100	0.072	0.024	4.08	0.057
TD-1397	1396.50	1558	24	22826	236	1.50	0.100	23	0.341	3.54	45	0.215	0.025	112	0.072	0.013	6.95	0.057
TD-1492	1492.50	1719	28	61801	272	13.56	0.171	28	0.324	3.94	72	0.201	0.025	219	0.072	0.016	3.95	0.075
TD-1544	1543.50	2396	248	145473	221	14.60	0.999	32	0.945	2.68	54	0.202	0.098	173	0.117	0.043	8.37	0.247
TD-1558	1557.55	2330	17	49705	186	5.79	0.092	24	0.288	3.54	43	0.235	0.019	97	0.093	0.013	3.95	0.067
TD-1571	1570.50	1856	26	30639	179	1.17	0.072	20	0.301	2.58	39	0.201	0.016	97	0.072	0.011	3.95	0.029
TD-1616	1615.75	1718	23	35342	194	1.63	0.125	19	0.302	3.09	43	0.256	0.021	133	0.072	0.015	30.02	0.046

Appendix B
Authored and Coauthored publications

The core of my PhD project focused on the geochemical analysis of dust from the Talos Dome ice core, as has been discussed in depth in this thesis. This work has lead, up to now, to two publications which I have coauthored:

- Baccolo, G., Cibin, G., Delmonte, B., Hampai, D., Marcelli, A., Di Stefano, E., Macis S., Maggi, V. (2018). The contribution of synchrotron light for the characterization of atmospheric mineral dust in deep ice cores: Preliminary results from the Talos Dome ice core (East Antarctica). Condensed Matter, 3(3), 25.
- Baccolo, G., Delmonte, B., Niles, P. B., Cibin, G., Di Stefano, E., Hampai, D., Keller, L., Maggi, V., Marcelli, A., Michalski, J., Snead, C., Frezzotti, M. (2020, in review). Jarosite formation in deep Antarctic ice provides a window into acidic, water-limited weathering on Mars.

During the three years of my phD I have also conducted research involving different aspects of radioactivity, atmospheric circulation and glacier dynamics. Here I will present a brief overview on the four publications (one as first author) to which this research led, reporting for each one my involvement in the project together with the full reference for the article.

- **^{137}Cs contamination in the Adamello glacier: Improving the analytical method**

  This work is part of a bigger project which aims at studying the radioactive contamination inside the Adamello glacier (Italy). This will be done by fully reconstructing profiles of ^{137}Cs and ^{3}H inside the Adamello ice core. ^{137}Cs is measured with γ-spectroscopy through the use of germanium detectors, while ^{3}H is measured with β-spectroscopy using liquid scintillation. The reconstruction of these profiles will first of all aid the dating of the ice core, since these radioactive isotopes provide well know fixed temporal horizons inside the ice. Moreover, since cesium mainly travels bound to particulate matter while tritium is incorporated in the water molecule, the comparison of the two profiles may help shed a light on percolation processes which occur inside the temperate glaciers. I have carried out all laboratory measurements, data analysis and result interpretation for this project. This article represents a first methodological study on the analysis of ^{137}Cs. Another publication which will include extended profiles of both ^{137}Cs and ^{3}H is in preparation.

  Di Stefano, E., Clemenza, M., Baccolo, G., Delmonte, B., Maggi, V. (2019). 137Cs contamination in the Adamello glacier: Improving the analytical method. Journal of environmental radioactivity, 208, 106039.

  https://doi.org/10.1016/j.jenvrad.2019.106039

- **Giant dust particles at Nevado Illimani: a proxy of summertime deep convection over the Bolivian Altiplano**

This work concerns the study of a firn core extracted from Nevado Illimani (Bolivia), with the aim of better constraining atmospheric circulation at the site. A thorough study of dust particles through an array of techniques was conducted. I mainly worked on the data analysis of neutron activation, the same technique applied in this thesis to the Talos Dome samples.

Lindau, F. G. L., Simões, J. C., Delmonte, B., Ginot, P., Baccolo, G., Paleari, C. I., Di Stefano, E., Korotkikh, E., Introne, D. S., Maggi, V., Garzanti, E., and Andò, S.: Giant dust particles at Nevado Illimani: a proxy of summertime deep convection over the Bolivian Altiplano, The Cryosphere Discuss., in review, 2020.

https://doi.org/10.5194/tc-2020-55

- **Artificial and natural radionuclides in cryoconite as tracers of supraglacial dynamics: Insights from the Morteratsch glacier (Swiss Alps)**

  This works concerns the study of cryoconite samples from Morteratsch glacier (Switzerland). A radioactive characterization of this sediment present on the surface of glaciers was performed in order to investigate the connection between the formation and distribution of cryoconites and hydrological supraglacial processes. I was involved in the measurements and data analysis of cryoconite samples through neutron activation analysis.

  Baccolo, G., Nastasi, M., Massabò, D., Clason, C., Di Mauro, B., Di Stefano, E., Lokas, E., Prati, P., Previtali, E., Takeuchi, N., Delmonte, B., Maggi, V. (2020). Artificial and natural radionuclides in cryoconite as tracers of supraglacial dynamics: Insights from the Morteratsch glacier (Swiss Alps). CATENA, 191, 104577.

  https://doi.org/10.1016/j.catena.2020.104577

- **The Ruthenium-106 plume over Europe in 2017: a source-receptor model to estimate the source region**

  The aim of this work was to use the combination of air measurement datasets and atmospheric circulation models to constrain the location of an unknown emission source of ^{106}Ru. This radionuclide, which is a fission product of uranium and plutonium, had been detected between the end of September and the beginning of October 2017 throughout Europe, including Italy. Radioactivity levels of particulate matter trapped in the air filters installed at Milano-Bicocca university were also measured and ^{106}Ru contamination was indeed found. I carried out the measurements and data analysis of these filters through the use of γ-spectroscopy.

  Maffezzoli, N., Baccolo, G., Di Stefano, E., Clemenza, M. (2019). The Ruthenium-106 plume over Europe in 2017: a source-receptor model to estimate the source region. Atmospheric Environment, 212, 239-249.

  https://doi.org/10.1016/j.atmosenv.2019.05.033